Doctral thesis

Fermi Surface and Superconducting Properties of TrX_4 (Tr = Rh, Ir; X = Ge, Sn) with Chiral Crystal Structure

Naoki Nakamura

Department of Physics
Tokyo Metropolitan University
2023/February/27th

Contents

List of Figures

List of Tables

CHAPTER 1

Introduction

One of the recent interests in the field of solid state and condensed matter physics is related to noncentrosymmetric compounds [1]. Typical examples of noncentrosymmetric crystal structures, which lack a center of inversion, are of the so-called Rashba-type and chiral nature. In these crystal structures, the antisymmetric spin-orbit interaction acts on the conduction electrons as an effective (emergent) magnetic field. The term $\alpha(\boldsymbol{n} \times \boldsymbol{p}) \cdot \boldsymbol{\sigma}$ (where α is the strength of the spin-orbit interaction, $\boldsymbol{n}$ is the unit vector for the crystalline potential gradient $\nabla V(\boldsymbol{r})$, $\boldsymbol{p}$ $(= \hbar\boldsymbol{k}, \boldsymbol{k}$: wave number) is the momentum of conduction electrons, and σ is the Pauli matrix of the up and down spin states) is added to the Hamiltonian for conduction electrons;

$$\varepsilon_{p\pm} = \frac{\boldsymbol{p}^2}{2m^*} + \alpha(\boldsymbol{n} \times \boldsymbol{p}) \cdot \sigma.$$

The corresponding Fermi surface thus splits into two Fermi surfaces with topology very similar to each other but different volumes. This splitting of the Fermi surfaces appears in the absence of an external magnetic field and introduces a characteristic momentum $\boldsymbol{p}$-dependent spin texture to the electronic states.

For example, the Fermi surfaces of $LaIrGe_3$, $LaRhGe_3$, and $LaCoGe_3$ with the tetragonal Rashba-type structure ($I4mn$, No. 107) are split into two Fermi surfaces, where the crystal structure lacks inversion symmetry along the tetragonal [001] direction and the caliper length of two split Fermi surfaces along the [001] direction, $2k_z$, is unchanged between the two split Fermi surfaces because of $\boldsymbol{n}$ = [001] [2, 3]. The splitting energy $\Delta\varepsilon$ for a main Fermi surface is 1090 K in $LaIrGe_3$, 510 K in $LaRhGe_3$, and 460 K in

$LaCoGe_3$. The splitting energy is larger in the Ir-5d conduction electrons than in the Rh-4d and Co-3d electrons, reflecting the magnitude of spin-orbit coupling. Furthermore, the spins of conduction electrons are rotated in the direction of the effective field, $\boldsymbol{n} \times \boldsymbol{p}$, clockwise in the k_z plane for one Fermi surface and counterclockwise for the other Fermi surface.

The present spin texture of conduction electrons produces a huge upper critical field $\mu_0 H_{c2}(0) \simeq 45$ T in a heavy fermion superconductor $CeIrSi_3$ with the same crystal structure as $LaIrSi_3$ mentioned above despite the low superconducting transition temperature $T_{sc} = 1.6$ K [3]. This is because all the spins of conduction electrons are perpendicular to the external magnetic field direction for $H \parallel [001]$, and the spin susceptibility for $H \parallel [001]$ does not change below T_{sc}, revealing no paramagnetic suppression in H_{c2}.

The magnetic skyrmion is now a well-known spin texture of magnetic ions observed in MnSi and EuPtSi with the cubic chiral structure ($P2_13$, No. 198) [4, 5, 6]. This structure has neither spatial inversion symmetry nor mirror symmetry, and chiral (left- and right-handed) structures are allowed for these compounds. The 3d electrons in MnSi are itinerant and become conduction electrons. Correlations between these conduction electrons are reflected in a relatively large electronic specific heat coefficient and cyclotron effective masses, together with the magnetic ordering and magnetic moment. Meanwhile, the 4f electrons in a rare earth compound EuPtSi are localized, and the RKKY interaction plays a predominant role in magnetism. Therefore, the mutual magnetic interaction between the 4f electrons occupying different atomic sites cannot be direct, such as in 3d-magnetism, but should be indirect, which occurs via the spins of the conduction electrons. As the crystal structure of MnSi and EuPtSi lacks the inversion symmetry, canting of spins or helical magnetic structure could be realized owing to an additional magnetic exchange term of the Dzyaloshinskii-Moriya interaction at zero magnetic field [7, 8]. The skyrmion phase is induced in a limited magnetic field and temperature regions.

The Fermi surface in the chiral structure also splits into two different Fermi surfaces, as in VSi_2, $NbSi_2$, and $TaSi_2$ with the hexagonal chiral structure, where VSi_2 and $TaSi_2$ belong to $P6_422$, while $NbSi_2$ only belongs to $P6_222$ [9]. The splitting energy of the main Fermi surface is 490 K in $TaSi_2$, 210 K in $NbSi_2$ and 39 K in VSi_2. It is known in a simple spherical Fermi surface centered at the Γ point (center in the Brillouin zone) that the spins of conduction electrons are directed from the Γ point to outside for one Fermi surface, as in Fermi velocity, while spins are centered in the Γ pint for the other Fermi surface. Very recently, these chiral compounds are found to exhibit a spin-polarized

state when the charge current is injected into the crystal [10]. Namely, a spin-polarized transport occurs in a linear regime of the current-voltage characteristics. The spin-polarized currents propagate over 10 μm.

In the present thesis, we studied the electronic states and Fermi surface properties from the electrical resistivity, specific heat, magnetoresistance, and de Haas-van Alphen experiments using the high-quality single crystals of α-$IrSn_4$, α-$RhSn_4$, $IrGe_4$, and $RhGe_4$ with the trigonal chiral structure. Characteristic angular dependences of the dHvA frequencies were observed in the present study, reflecting the present trigonal chiral structure, together with the anisotropic upper critical fields in superconductivity.

In Chapter 2, we will give a review of the fundamental electronic properties for noncentrosymmetric compounds including the chiral compounds. In Chapter 3, we will introduce the single crystal growth and the experimental methods including de Haas-van Alphen (dHvA) effect. In Chapter 4, we present the experimental results with analyses and discussion. Finally, the present study is summarized and concluded in Chapter 5.

CHAPTER 2

Review on Noncentrosymmetric Crystal Structures and Electronic States

2.1 Noncentrosymmetric crystal structures

In intermetallic compounds, a vast number of elements are regularly arranged. The smallest unit is a unit cell. For example, the unit cell of Cu is shown in Fig. 2.1(a) [11]. A ball corresponds to the Cu element. These units are regularly arranged to form a crystal. Some compounds have the structure shown in Fig. 2.1(b). This is the tetragonal crystal structure of $CePt_3Si$ [12]. The Si atom, which is represented as the red ball, is not symmetrical with respect to the $z = 1/2$ plane. This is one of the noncentrosymmetric crystal structures, so-called the Rashba-type. Furthermore, some compounds, such as Te, have a chiral structure as shown in Fig. 2.1(c) [13]. Thus, intermetallic compounds have various structures, and the symmetry of crystal structures greatly affects their electronic properties. $CePt_3Si$ has been studied for unconventional superconductivity caused by the inversion symmetry breaking [12, 14]. In Te, the non-reciprocal electrical resistivity, which is different between the left- and right-handed crystals, is observed [15].

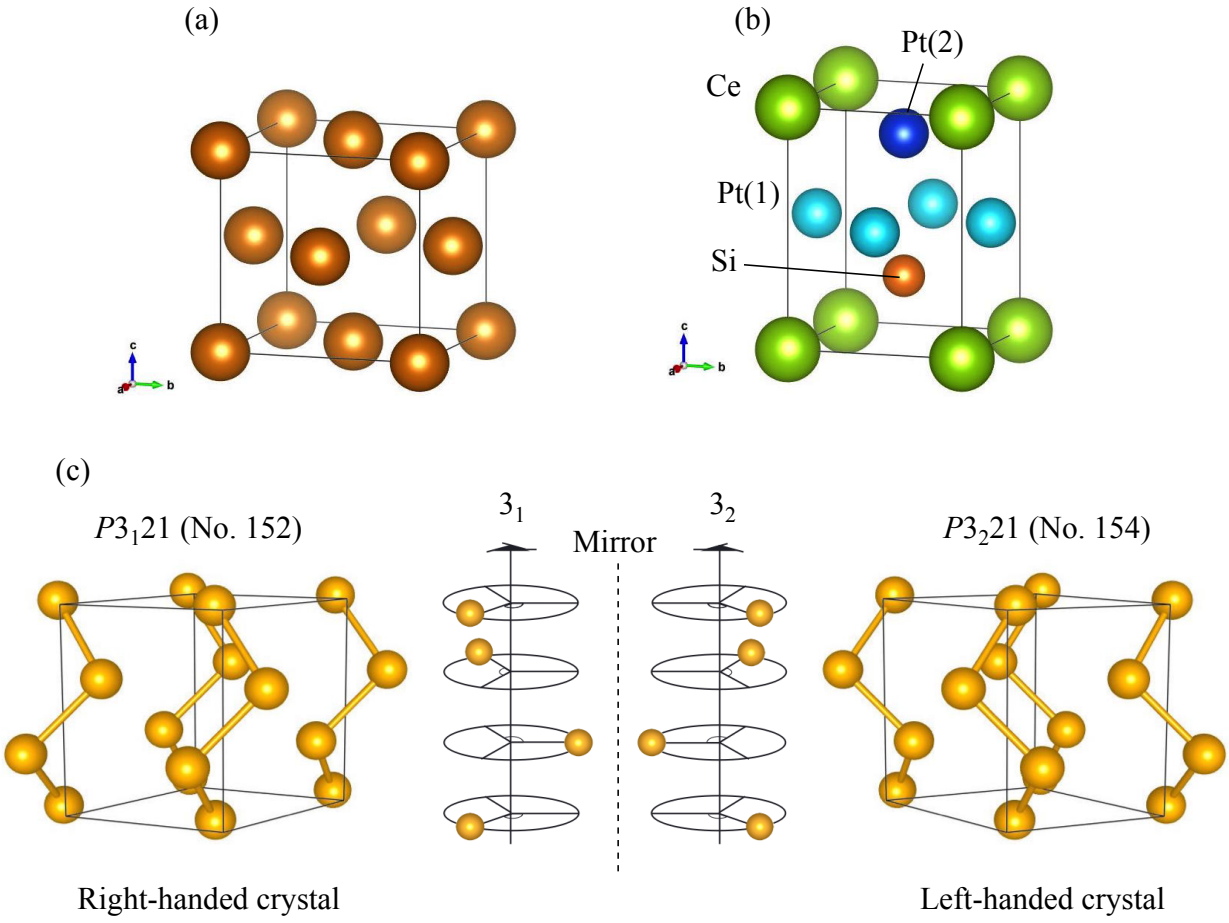

Figure 2.1: Crystal structures of (a) Cu, (b) $CePt_3Si$, and (c) Te.

Lattice systems and Bravais lattice

In a crystal, a large number of atoms are arranged regularly. Therefore, there are points that have exactly the same surrounding environment. These points are called lattice, which is connected to another lattice by translation operations. Note that the lattice is a point with identical surroundings, but not necessarily an atom there. The parallelepiped, which is formed by lattice, is the unit cell, and there are 14 independent unit cells in three dimensions. These independent unit cells are called Bravais lattice as shown in Fig. 2.2(a) [16]. The lattice systems is a classification of Bravais lattices by symmetry, and there are seven types of lattice systems: triclinic, monoclinic, orthorhombic, rhombohedral, hexagonal, tetragonal, and cubic. Fig. 2.2(b) shows the group-subgroup relationship of Bravais lattice in the three dimensions [17].

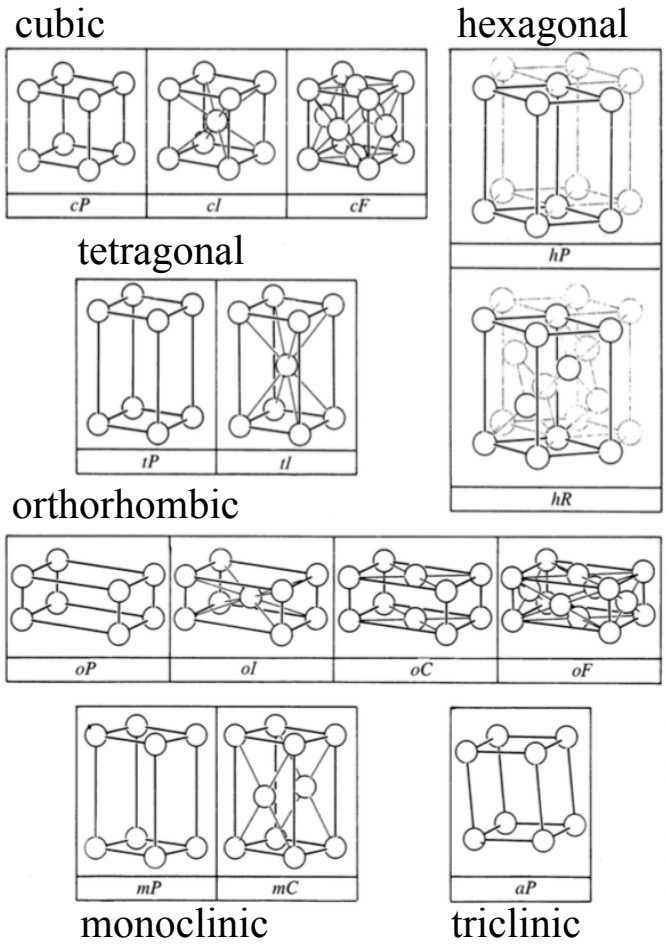

Figure 2.2: (a) 14 types of Bravais lattice in three dimensions, cited from ref. [16].

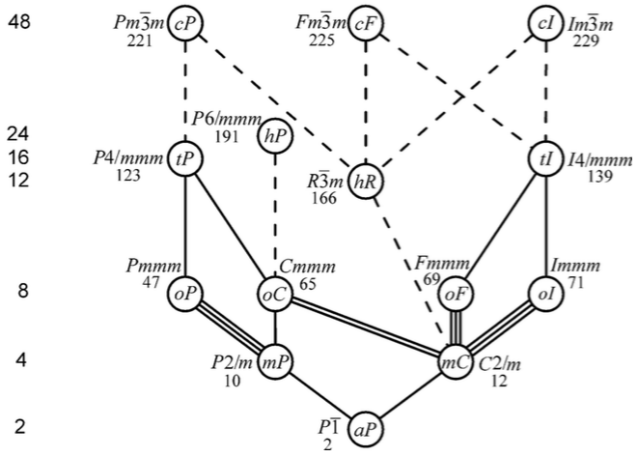

Figure 2.3: Group-subgroup relationship of Bravais lattice, cited from ref. [17].

crystal systems and geometric crystal classes

The Bravais lattices are classified by the translational symmetry of the lattice. When discussing the electronic properties of the compound, for example, the electrical resistivity, it is not necessary to consider translational symmetry. It is sufficient to consider the symmetry within the unit lattice, i.e., the symmetry of the atoms in the unit lattice. The symmetry of the internal structure is described by point symmetry operations such as rotation, mirror, or inversion around a certain point, representing point groups. By using only the rotation operations, seven independent basic elements, as shown in Fig. 2.4, are obtained in three dimensions, which compose crystal systems. Adding further rotation operations, mirror, and inversion operations, 32 independent elements are obtained, which compose geometric crystal classes. Geometric crystal classes correspond to crystal point groups. The group-subgroup relations of each point group are shown in Fig. 2.5 [18]. Of the 32 crystal point groups, 11 types of point groups without inversion center compose Laue groups. Symmetries of a Laue picture can be described by the symmetry of the Laue group with the Friedel's rule, meaning that the intensities of the (h, k, l) and $(\bar{h}, \bar{k}, \bar{l})$ reflections are equal.

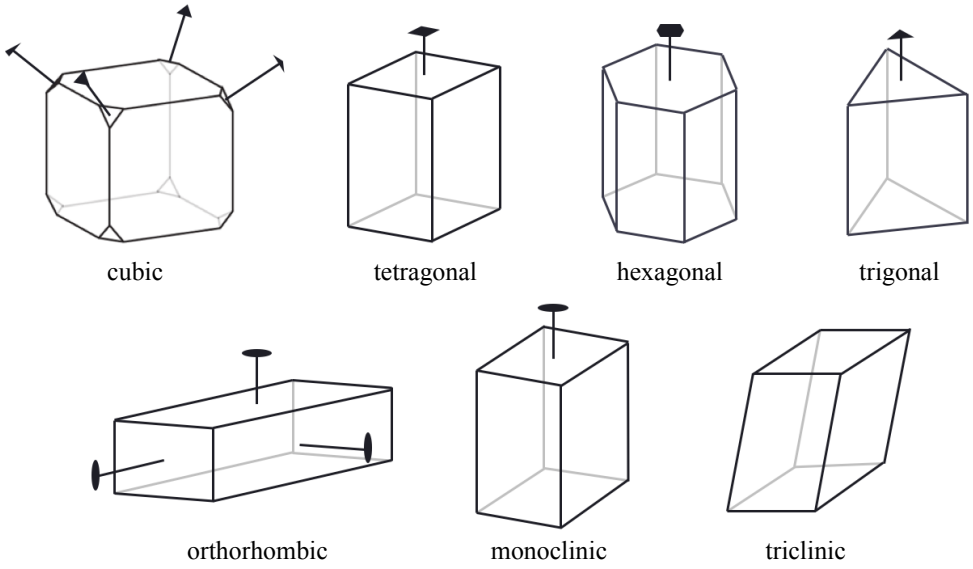

Figure 2.4: 7-types of crystal systems.

Table 2.1: Summary of the 32 crystal point group2 with Hermann–Mauguin notation, Schoenflies notation, stereographic projection.

General symbol	Crystal system					
	triclinic	monoclinic (top) orthorhombic (bottom)	tertagonal	trigonal	hexagonal	cubic
n	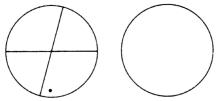 C_1 (1)	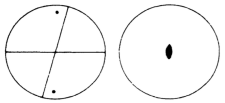 C_2 (2)	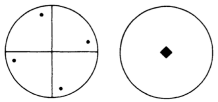 C_4 (4)	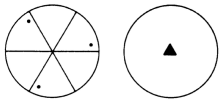 C_3 (3)	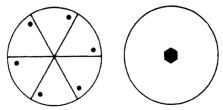 C_6 (6)	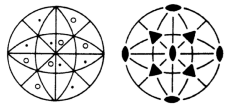 T (23)
$\bar{n}$	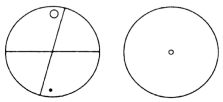 C_i ($\bar{1}$)	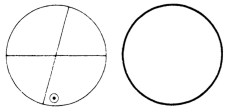 C_s ($\bar{2} \equiv m$)	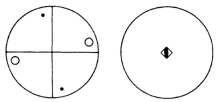 S_4 ($\bar{4}$)	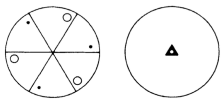 C_{3i} ($\bar{3}$)	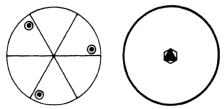 C_{3h} ($\bar{6} \equiv 3/m$)	
$n + \bar{1}$		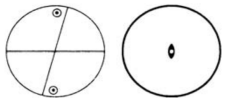 C_{2h} (2/m)	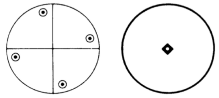 C_{4h} (4/m)		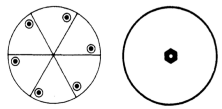 C_{6h} (6/m)	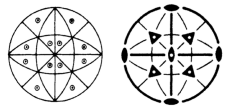 T_h ($m\bar{3}$)
$n22$		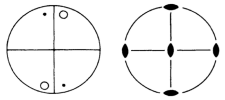 D_2 (222)	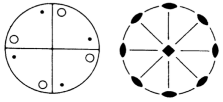 D_4 (422)	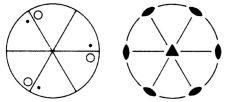 D_3 (32)	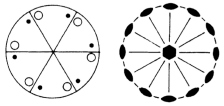 D_6 (622)	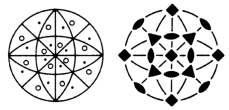 O (432)
nmm		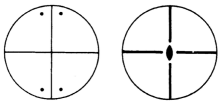 C_{2v} ($mm2$)	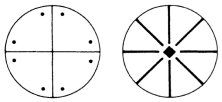 C_{4v} (4mm)	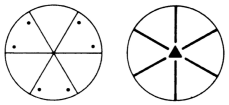 C_{3v} (3m)	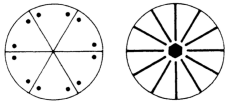 C_{6v} (6mm)	
$\bar{n}$2m			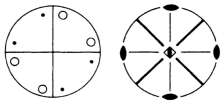 D_{2d} ($\bar{4}2m$)	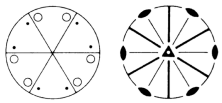 D_{3d} ($\bar{3}m$)	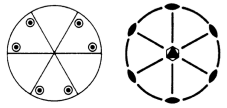 D_{3h} ($\bar{6}2m$)	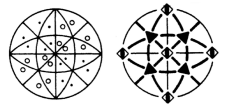 T_d ($\bar{4}3m$)
$n22 + \bar{1}$		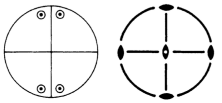 D_{2h} (mmm)	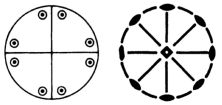 D_{4h} (4/mmm)		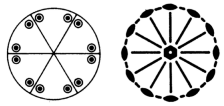 D_{6h} (6/mmm)	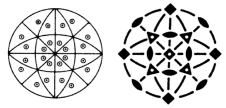 O_h ($m\bar{3}m$)

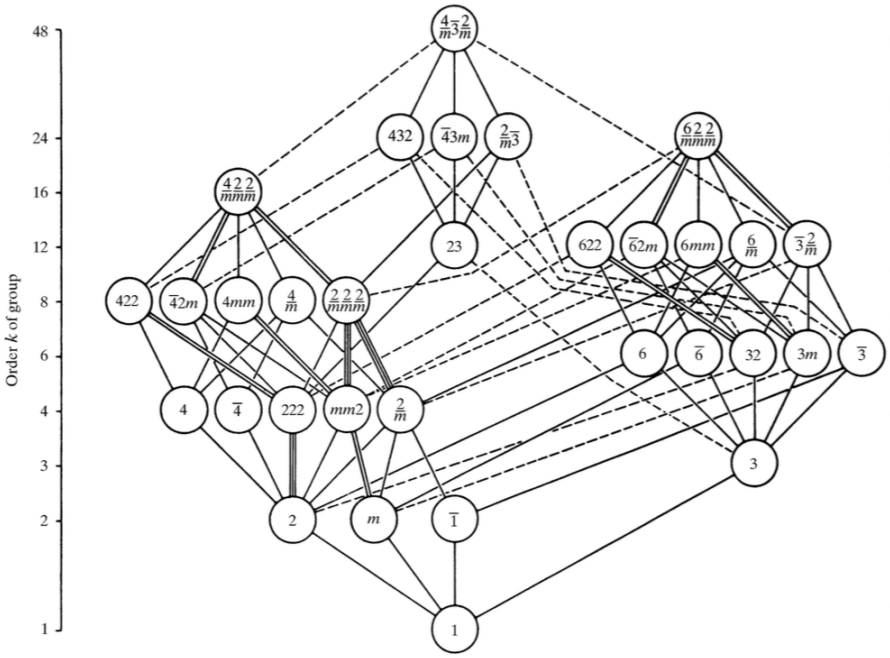

Figure 2.5: Group-subgroup relations of crystal point groups, cited from ref. [18].

crystallographic space groups

Lattice systems are classified by the translational symmetry of the lattice, and crystal systems are classified by the point symmetry in the unit cell. By combining these two types of operations, the symmetry of a crystal can be expressed. Both 14 types of Bravais lattices and 32 types of crystal point groups yield 73 independent closed groups, which are called arithmetic crystal classes. In addition to the above symmetry operations, some crystals have partial translation operations such as spiral and glide operations. Considering these symmetrical operations, 230 independent elements are composed of crystallographic space groups. The crystallographic space groups, which correspond to one-to-one to arithmetic crystal classes, are called symmorphic space groups, and the others are classified as nonsymmorphic space groups. The summary of the classification is shown in Fig. 2.6.

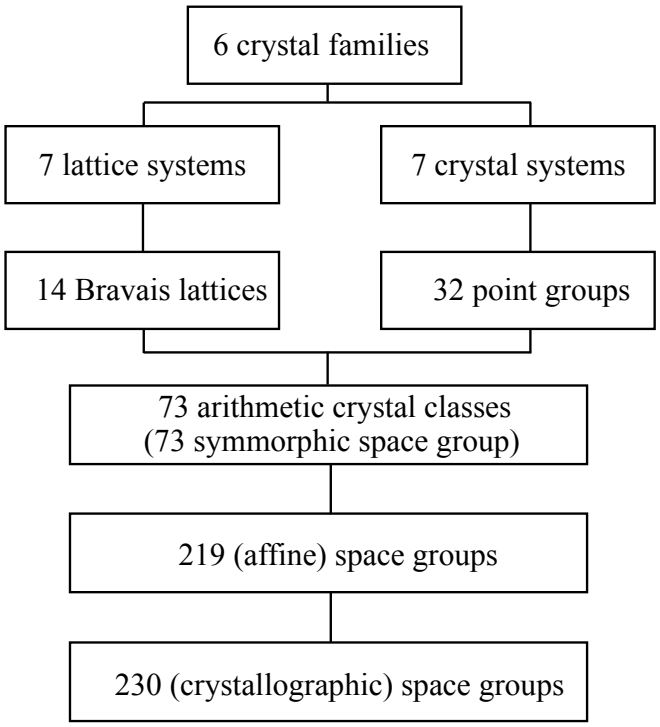

Figure 2.6: Classifications of space groups.

Noncentrosymmetric crystal structures

Performing an inversion operation on an object means performing a point symmetry operation on a point. The center of a point symmetry operation is called the inversion center. If the inversion center is the origin, then inversion operation $\mathcal{P}$ is expressed as $\mathcal{P} : (x, y, z,) \rightarrow (-x, -y, -z)$. A crystal structure without an inversion center is defined as the noncentrosymmetric crystal structure. Figures 2.7(a) and 2.7(b) show the centrosymmetric crystal structure of $ThCr_2Si_2$-type with an inversion center [19] and the noncentrocymmetric crystal structure of $BaNiSn_3$-type without an inversion center [20], respectively. The $ThCr_2Si_2$-type structure is not changed by the inversion operation, whereas the $BaNiSn_3$-type is changed after the inversion operation. Whether a crystal structure has an inversion center or not can be determined by the space group to which the crystal belongs. There are 138 space groups without inversion centers in the 230 space groups, which are summarized in Table 2.2.

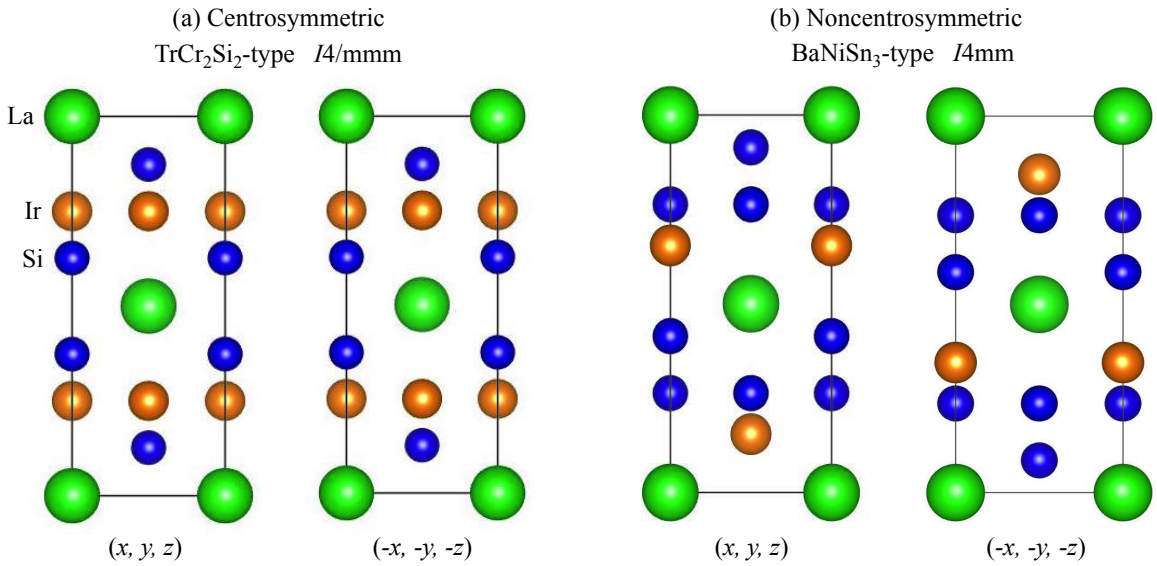

Figure 2.7: Crystal structures of (a) $ThCr_2Si_2$-type with an inversion center and (b) $BaNiSn_3$-type without an inversion center.

Table 2.2: Summary of 230 types of crystallographic space groups together with their short and full international symbols and also with the Schenfiels symbols. They are divided into 92 centrosymmetric space groups (their space group numbers are shown in black) and 138 noncentrosymmetric ones (in red). Suffix c of the space group number represents the chiral structure, courtesy of A. Teruya.

Triclinic, Monoclinic

1[c]	$P1$	$(P1)$	C_1^1	6*	Pm	$(P1m1)$	C_s^1	11*	$P2_1/m$	$(P12_1/m1)$	C_{2h}^2
2	$P\bar{1}$	$(P\bar{1})$	C_i^1	7*	Pc	$(P1c1)$	C_s^2	12*	$C2/m$	$(C12/m1)$	C_{2h}^3
3[c]*	$P2$	$(P121)$	C_2^1	8*	Cm	$(C1m1)$	C_s^3	13*	$P2/c$	$(P12/c1)$	C_{2h}^4
4[c]*	$P2_1$	$(P12_11)$	C_2^2	9*	Cc	$(C1c1)$	C_s^4	14*	$P2_1/c$	$(P12_1/c1)$	C_{2h}^5
5[c]*	$C2$	$(C121)$	C_2^3	10*	$P2/m$	$(P12/m1)$	C_{2h}^1	15*	$C2/c$	$(C12/c1)$	C_{2h}^6

Orthorombic

16[c]	$P222$	$(P222)$	D_2^1	36	$Cmc2_1$	$(Cmc2_1)$	C_{2v}^{12}	56	$Pccn$	$(P2_1/c2_1/c2/n)$	D_{2h}^{10}
17[c]	$P222_1$	$(P222_1)$	D_2^2	37	$Ccc2$	$(Ccc2)$	C_{2v}^{13}	57	$Pbcm$	$(P2/b2_1/c2_1/m)$	D_{2h}^{11}
18[c]	$P2_12_12$	$(P2_12_12)$	D_2^3	38	$Amm2$	$(Amm2)$	C_{2v}^{14}	58	$Pnnm$	$(P2_1/n2_1/n2/m)$	D_{2h}^{12}
19[c]	$P2_12_12_1$	$(P2_12_12_1)$	D_2^4	39	$Abm2$	$(Abm2)$	C_{2v}^{15}	59*	$Pmmn$	$(P2_1/m2_1/m2/n)$	D_{2h}^{13}
20[c]	$C222_1$	$(C222_1)$	D_2^5	40	$Ama2$	$(Ama2)$	C_{2v}^{16}	60	$Pbcn$	$(P2_1/b2/c2_1/n)$	D_{2h}^{14}
21[c]	$C222$	$(C222)$	D_2^6	41	$Aba2$	$(Aba2)$	C_{2v}^{17}	61	$Pbca$	$(P2_1/b2_1/c2_1/a)$	D_{2h}^{15}
22[c]	$F222$	$(F222)$	D_2^7	42	$Fmm2$	$(Fmm2)$	C_{2v}^{18}	62	$Pnma$	$(P2_1/n2_1/m2_1/a)$	D_{2h}^{16}
23[c]	$I222$	$(I222)$	D_2^8	43	$Fdd2$	$(Fdd2)$	C_{2v}^{19}	63	$Cmcm$	$(C2/m2/c2_1/m)$	D_{2h}^{17}
24[c]	$I2_12_12_1$	$(I2_12_12_1)$	D_2^9	44	$Imm2$	$(Imm2)$	C_{2v}^{20}	64	$Cmca$	$(C2/m2/c2_1/a)$	D_{2h}^{18}
25	$Pmm2$	$(Pmm2)$	C_{2v}^1	45	$Iba2$	$(Iba2)$	C_{2v}^{21}	65	$Cmmm$	$(C2/m2/m2/m)$	D_{2h}^{19}
26	$Pmc2_1$	$(Pmc2_1)$	C_{2v}^2	46	$Ima2$	$(Ima2)$	C_{2v}^{22}	66	$Cccm$	$(C2/c2/c2/m)$	D_{2h}^{20}
27	$Pcc2$	$(Pcc2)$	C_{2v}^3	47	$Pmmm$	$(P2/m2/m2/m)$	D_{2h}^1	67	$Cmma$	$(C2/m2/m2/a)$	D_{2h}^{21}
28	$Pma2$	$(Pma2)$	C_{2v}^4	48*	$Pnnn$	$(P2/n2/n2/n)$	D_{2h}^2	68*	$Ccca$	$(C2/c2/c2/a)$	D_{2h}^{22}
29	$Pca2_1$	$(Pca2_1)$	C_{2v}^5	49	$Pccm$	$(P2/c2/c2/m)$	D_{2h}^3	69	$Fmmm$	$(F2/m2/m2/m)$	D_{2h}^{23}
30	$Pnc2$	$(Pnc2)$	C_{2v}^6	50*	$Pban$	$(P2/b2/a2/n)$	D_{2h}^4	70*	$Iddd$	$(I2/d2/d2/d)$	D_{2h}^{24}
31	$Pmn2_1$	$(Pmn2_1)$	C_{2v}^7	51	$Pmma$	$(P2_1/m2/m2/a)$	D_{2h}^5	71	$Immm$	$(I2/m2/m2/m)$	D_{2h}^{25}
32	$Pba2$	$(Pba2)$	C_{2v}^8	52	$Pnna$	$(P2/n2_1/n2/a)$	D_{2h}^6	72	$Ibam$	$(I2/b2/a2/m)$	D_{2h}^{26}
33	$Pna2_1$	$(Pna2_1)$	C_{2v}^9	53	$Pmna$	$(P2/m2/n2_1/a)$	D_{2h}^7	73	$Ibca$	$(I2/b2/c2/a)$	D_{2h}^{27}
34	$Pnn2$	$(Pnn2)$	C_{2v}^{10}	54	$Pcca$	$(P2_1/c2/c2/a)$	D_{2h}^8	74	$Imma$	$(I2/m2/m2/a)$	D_{2h}^{28}
35	$Cmm2$	$(Cmm2)$	C_{2v}^{11}	55	$Pbam$	$(P2_1/b2_1/a2/m)$	D_{2h}^9				

Tetragonal

75[c]	$P4$	$(P4)$	C_4^1	98[c]	$I4_122$	$(I4_122)$	D_4^{10}	121	$I\bar{4}2m$	$(I\bar{4}2m)$	D_{2d}^{11}
76[c]	$P4_1$	$(P4_1)$	C_4^2	99	$P4mm$	$(P4mm)$	C_{4v}^1	122	$I\bar{4}2d$	$(I\bar{4}2d)$	D_{2d}^{12}
77[c]	$P4_2$	$(P4_2)$	C_4^3	100	$P4bm$	$(P4bm)$	C_{4v}^2	123	$P4/mmm$	$(P4/m2/m2/m)$	D_{4h}^1
78[c]	$P4_3$	$(P4_3)$	C_4^4	101	$P4_2cm$	$(P4_2cm)$	C_{4v}^3	124	$P4/mcc$	$(P4/m2/c2/c)$	D_{4h}^2
79[c]	$I4$	$(I4)$	C_4^5	102	$P4_2nm$	$(P4_2nm)$	C_{4v}^4	125*	$P4/nbm$	$(P4/n2/b2/m)$	D_{4h}^3
80[c]	$I4_1$	$(I4_1)$	C_4^6	103	$P4cc$	$(P4cc)$	C_{4v}^5	126*	$P4/nnc$	$(P4/n2/n2/c)$	D_{4h}^4
81	$P\bar{4}$	$(P\bar{4})$	S_4^1	104	$P4nc$	$(P4nc)$	C_{4v}^6	127	$P4/mbm$	$(P4/m2_1/bm)$	D_{4h}^5
82	$I\bar{4}$	$(I\bar{4})$	S_4^2	105	$P4_2mc$	$(P4_2mc)$	C_{4v}^7	128	$P4/mnc$	$(P4/m2_1/nc)$	D_{4h}^6
83	$P4/m$	$(P4/m)$	C_{4h}^1	106	$P4_2bc$	$(P4_2bc)$	C_{4v}^8	129*	$P4/nmm$	$(P4/n2_1/mm)$	D_{4h}^7
84	$P4_2/m$	$(P4_2/m)$	C_{4h}^2	107	$I4mm$	$(I4mm)$	C_{4v}^9	130*	$P4/ncc$	$(P4/n2_1/cc)$	D_{4h}^8
85*	$P4/n$	$(P4/n)$	C_{4h}^3	108	$I4cm$	$(I4cm)$	C_{4v}^{10}	131	$P4_2/mmc$	$(P4_2/m2/m2/c)$	D_{4h}^9
86*	$P4_2/n$	$(P4_2/n)$	C_{4h}^4	109	$I4_1md$	$(I4_1md)$	C_{4v}^{11}	132	$P4_2/mcm$	$(P4_2/m2/c2/m)$	D_{4h}^{10}
87	$I4/m$	$(I4/m)$	C_{4h}^5	110	$I4_1cd$	$(I4_1cd)$	C_{4v}^{12}	133*	$P4_2/nbc$	$(P4_2/n2/b2/c)$	D_{4h}^{11}
88*	$I4_1/a$	$(I4_1/a)$	C_{4h}^6	111	$P\bar{4}2m$	$(P\bar{4}2m)$	D_{2d}^1	134*	$P4_2/nnm$	$(P4_2/n2/n2/m)$	D_{4h}^{12}
89[c]	$P422$	$(P422)$	D_4^1	112	$P\bar{4}2c$	$(P\bar{4}2c)$	D_{2d}^2	135	$P4_2/mbc$	$(P4_2/m2_1/b2/c)$	D_{4h}^{13}
90[c]	$P42_12$	$(P42_12)$	D_4^2	113	$P\bar{4}2_1m$	$(P\bar{4}2_1m)$	D_{2d}^3	136	$P4_2/mnm$	$(P4_2/m2_1/n2/m)$	D_{4h}^{14}
91[c]	$P4_122$	$(P4_122)$	D_4^3	114	$P\bar{4}2_1c$	$(P\bar{4}2_1c)$	D_{2d}^4	137*	$P4_2/nmc$	$(P4_2/n2_1/m2/c)$	D_{4h}^{15}
92[c]	$P4_12_12$	$(P4_12_12)$	D_4^4	115	$P\bar{4}m2$	$(P\bar{4}m2)$	D_{2d}^5	138*	$P4_2/ncm$	$(P4_2/n2_1/c2/m)$	D_{4h}^{16}
93[c]	$P4_222$	$(P4_222)$	D_4^5	116	$P\bar{4}c2$	$(P\bar{4}c2)$	D_{2d}^6	139	$I4/mmm$	$(I4/m2/m2/m)$	D_{4h}^{17}
94[c]	$P4_22_12$	$(P4_22_12)$	D_4^6	117	$P\bar{4}b2$	$(P\bar{4}b2)$	D_{2d}^7	140	$I4/mcm$	$(I4/m2/c2/m)$	D_{4h}^{18}
95[c]	$P4_322$	$(P4_322)$	D_4^7	118	$P\bar{4}n2$	$(P\bar{4}n2)$	D_{2d}^8	141*	$I4_1/amd$	$(I4_1/a2/m2/d)$	D_{4h}^{19}
96[c]	$P4_32_12$	$(P4_32_12)$	D_4^8	119	$I\bar{4}m2$	$(I\bar{4}m2)$	D_{2d}^9	142*	$I4_1/acd$	$(I4_1/a2/c2/d)$	D_{4h}^{20}
97[c]	$I422$	$(I422)$	D_4^9	120	$I\bar{4}c2$	$(I\bar{4}c2)$	D_{2d}^{10}				

Trigonal (or Rhombohedral)

143[c]	$P3$	$(P3)$	C_3^1	152[c]	$P3_121$	$(P3_121)$	D_3^4	161*	$R3c$	$(R3c)$	C_{3v}^6
144[c]	$P3_1$	$(P3_1)$	C_3^2	153[c]	$P3_212$	$(P3_212)$	D_3^5	162	$P\bar{3}1m$	$(P\bar{3}12/m)$	D_{3d}^1
145[c]	$P3_2$	$(P3_2)$	C_3^3	154[c]	$P3_221$	$(P3_221)$	D_3^6	163	$P\bar{3}1c$	$(P\bar{3}12/c)$	D_{3d}^2
146[c]*	$R3$	$(R3)$	C_3^4	155[c]*	$R32$	$(R32)$	D_3^7	164	$P\bar{3}m1$	$(P\bar{3}2/m1)$	D_{3d}^3
147	$P\bar{3}$	$(P\bar{3})$	C_{3i}^1	156	$P3m1$	$(P3m1)$	C_{3v}^1	165	$P\bar{3}c1$	$(P\bar{3}2/c1)$	D_{3d}^4
148*	$R\bar{3}$	$(R\bar{3})$	C_{3i}^2	157	$P31m$	$(P31m)$	C_{3v}^2	166*	$R\bar{3}m$	$(R\bar{3}2/m)$	D_{3d}^5
149[c]	$P312$	$(P312)$	D_3^1	158	$P3c1$	$(P3c1)$	C_{3v}^3	167*	$R\bar{3}c$	$(R\bar{3}2/c)$	D_{3d}^6
150[c]	$P321$	$(P321)$	D_3^2	159	$P31c$	$(P31c)$	C_{3v}^4				
151[c]	$P3_112$	$(P3_112)$	D_3^3	160*	$R3m$	$(R3m)$	C_{3v}^5				

Hexagonal

168[c]	$P6$	$(P6)$	C_6^1	177[c]	$P622$	$(P622)$	D_6^1	186	$P6_3mc$	$(P6_3mc)$	C_{6v}^4
169[c]	$P6_1$	$(P6_1)$	C_6^2	178[c]	$P6_122$	$(P6_122)$	D_6^2	187	$P\bar{6}m2$	$(P\bar{6}m2)$	D_{3h}^1
170[c]	$P6_5$	$(P6_5)$	C_6^3	179[c]	$P6_522$	$(P6_522)$	D_6^3	188	$P\bar{6}c2$	$(P\bar{6}c2)$	D_{3h}^2
171[c]	$P6_2$	$(P6_2)$	C_6^4	180[c]	$P6_222$	$(P6_222)$	D_6^4	189	$P\bar{6}2m$	$(P\bar{6}2m)$	D_{3h}^3
172[c]	$P6_4$	$(P6_4)$	C_6^5	181[c]	$P6_422$	$(P6_422)$	D_6^5	190	$P\bar{6}2c$	$(P\bar{6}2c)$	D_{3h}^4
173[c]	$P6_3$	$(P6_3)$	C_6^6	182[c]	$P6_322$	$(P6_322)$	D_6^6	191	$P6/mmm$	$(P6/m2/m2/m)$	D_{6h}^1
174	$P\bar{6}$	$(P\bar{6})$	C_{3h}^1	183	$P6mm$	$(P6mm)$	C_{6v}^1	192	$P6/mcc$	$(P6/m2/c2/c)$	D_{6h}^2
175	$P6/m$	$(P6/m)$	C_{6h}^1	184	$P6cc$	$(P6cc)$	C_{6v}^2	193	$P6_3/mcm$	$(P6_3/m2/c2/m)$	D_{6h}^3
176	$P6_3/m$	$(P6_3/m)$	C_{6h}^2	185	$P6_3cm$	$(P6_3cm)$	C_{6v}^3	194	$P6_3/mmc$	$(P6_3/m2/m2/c)$	D_{6h}^4

Cubic

195[c]	$P23$	$(P23)$	T^1	207[c]	$P432$	$(P432)$	O^1	219	$F\bar{4}3c$	$(F\bar{4}3c)$	T_d^5
196[c]	$F23$	$(F23)$	T^2	208[c]	$P4_232$	(P_2432)	O^2	220	$I\bar{4}3d$	$(I\bar{4}3d)$	T_d^6
197[c]	$I23$	$(I23)$	T^3	209[c]	$F432$	$(F432)$	O^3	221	$Pm\bar{3}m$	$(P4/m\bar{3}2/m)$	O_h^1
198[c]	$P2_13$	$(P2_13)$	T^4	210[c]	$F4_132$	$(F4_132)$	O^4	222*	$Pn\bar{3}n$	$(P4/n\bar{3}2/n)$	O_h^2
199[c]	$I2_13$	$(I2_13)$	T^5	211[c]	$I432$	$(I432)$	O^5	223	$Pm\bar{3}n$	$(P4_2/m\bar{3}2/n)$	O_h^3
200	$Pm\bar{3}$	$(P2/m\bar{3})$	T_h^1	212[c]	$P4_332$	$(P4_332)$	O^6	224*	$Pn\bar{3}m$	$(P4_2/n\bar{3}2/m)$	O_h^4
201*	$Pn\bar{3}$	$(P2/n\bar{3})$	T_h^2	213[c]	$P4_132$	$(P4_132)$	O^7	225	$Fm\bar{3}m$	$(F4/m\bar{3}2/m)$	O_h^5
202	$Fm\bar{3}$	$(F2/m\bar{3})$	T_h^3	214[c]	$I4_132$	$(I4_132)$	O^8	226	$Fm\bar{3}c$	$(F4/m\bar{3}2/c)$	O_h^6
203*	$Fd\bar{3}$	$(F2/d\bar{3})$	T_h^4	215	$P\bar{4}3m$	$(P\bar{4}3m)$	T_d^1	227*	$Fd\bar{3}m$	$(F4_1/d\bar{3}2/m)$	O_h^7
204	$Im\bar{3}$	$(I2/m\bar{3})$	T_h^5	216	$F\bar{4}3m$	$(F\bar{4}3m)$	T_d^2	228*	$Fd\bar{3}c$	$(F4_1/d\bar{3}2/c)$	O_h^8
205	$Pa\bar{3}$	$(P2_1/a\bar{3})$	T_h^6	217	$I\bar{4}3m$	$(I\bar{4}3m)$	T_d^3	229	$Im\bar{3}m$	$(I4/m\bar{3}2/m)$	O_h^9
206	$Ia\bar{3}$	$(I2_1/a\bar{3})$	T_h^7	218	$P\bar{4}3n$	$(P\bar{4}3n)$	T_d^4	230	$Ia\bar{3}d$	$(I4_1/a\bar{3}2/d)$	O_h^{10}

2.2 Chiral crystal structures

Chirality is the geometric property of an object, which does not overlap with its mirror image. An object having chirality is called chiral, while the opposite term is achiral. Figures 2.8(a) and 2.8(b) show an achiral molecule and a chiral molecule, respectively. In the case of an achiral molecule, the mirror image, which is rotated by 180°, overlaps with the real image. On the other hand, in the case of a chiral molecule, even if the mirror image is rotated by 180°, it does not overlap with the real image. Of course, no matter how we rotate the molecule, the mirror image will not overlap with the real image. Namely, the achiral molecule has a mirror symmetry, while the chiral molecule does not have a mirror symmetry. Inversion, rotoinversion, and glide operation in addition to the mirror operation compose the symmetry operations of second kind, while translations, rotations, and screw rotation operations compose symmetry operations of first kind. In the language of symmetry operation, an achiral object has symmetry operations of second kind, while a chiral object has only symmetry operations of first kind. In the case of a crystal structure, whether the structure has chirality or not can be determined by the space group to which it belongs.

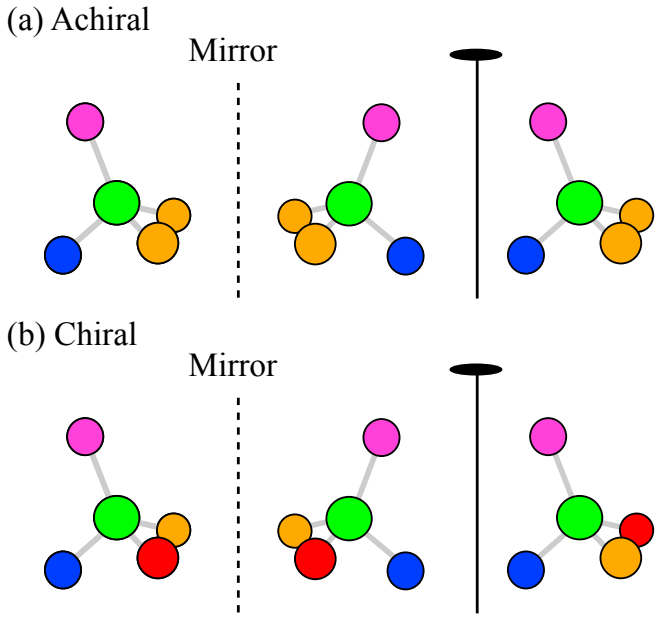

Figure 2.8: (a) Achiral molecule and (b) chiral molecule.

The space group of chiral crystals belongs to Sohncke groups which contain only symmetry operations of first kind. Among the 230 types of crystallographic space

groups, 65 are Sohncke types. Hermann-Mauguin symbols, which only contain number symbols, belong to Sohncke group. Figure 2.9 shows the classification of crystallographic space groups in terms of chirality. The space groups are divided into two groups: a chiral space group, whose Euclidean normalizer contains only symmetry operations of first kind, and the achiral space group, whose Euclidean normalizer contains symmetry operations of second kind. Among the 230 types of crystallographic space groups, 22 belong to the chiral space group, and the others 208 belong to the achiral space group. The 22 types of chiral space group form 11 enantiomorphic pairs. A crystal belonging to the chiral space group is definitely a chiral structure, but a crystal belonging to the achiral space group is not necessarily an achiral structure. The 208 types of achiral space groups are further classified into two groups: 43 space groups that have only symmetry operations of first kind and 165 space groups that include the symmetry operations of second kind. A crystal belonging to these 165 space groups shows achiral nature. On the other hand, a crystal belonging to these 43 space groups has a chiral structure. In summary, a crystal included in 65 (= 22 + 43) space groups is defined as a chiral crystal.

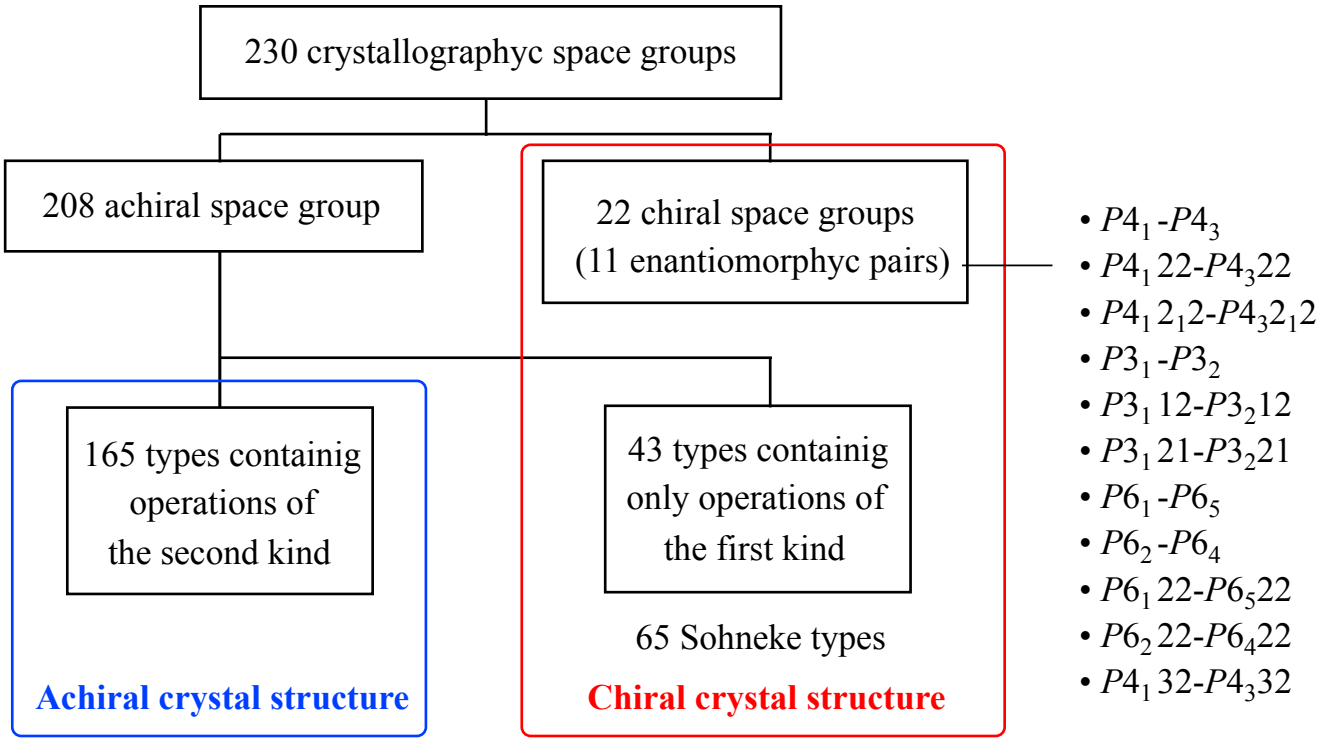

Figure 2.9: Classification of the 230 types of crystallographic space group in terms of chirality.

Te is presented as an example of a compound with a chiral structure, as shown in

Fig. 2.1. The crystal structure of Te is again shown in Fig. 2.10 and belongs to space group $P3_121$ (No. 152) or $P3_221$ (No. 154) [13]. The screw axis corresponds to the c-axis direction of the unit cell, and each Te atom takes a helical structure around the screw axis, rotating by 120° and translating by 1/3 of the lattice period. When a right-handed helix is defined as a helix that rotates clockwise in the direction of translation, the symmetry operation 3_1 corresponds to a right-handed helix and 3_2 corresponds to a left-handed helix. In the present Thesis, structures with right-handed helices are defined as the right-handed crystal, while structures with left-handed helices are defined as the left-handed crystal.

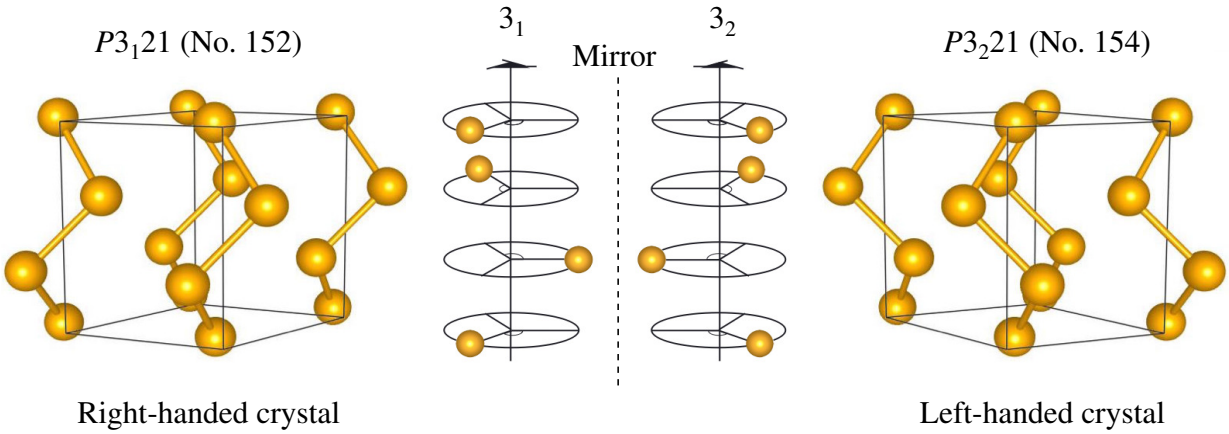

Figure 2.10: Chiral crystal structure of Te.

Determination of the left-handed and right-handed structures

The Flack parameter is useful to determine the chirality of the noncentrosymmetric structure by the single crystal X-ray diffraction analyses under consideration of the resonant scattering (the anomalous dispersion effect) [21, 22]. The Flack parameter x is defined by the following structure-amplitude equation

$$G^2(h,k,l,x) = (1-x)|F(h,k,l)|^2 + x|F(-h,-k,-l)|^2, \tag{2.1}$$

where G^2 is the square of the scaled observed structure factor, and $|F(h,k,l)^2|$ is the scattering intensity from the crystal structure. For a twinned crystal, x gives a measure of the relative amounts of the structure and its increase in the crystal.

2.3 Antisymmetric spin-orbit interaction and split Fermi surfaces

Spin-orbit coupling

The energies characterizing the band structure are of the order of 2-10 eV. The band splitting energy is, however, much smaller than 1 eV. A well-known case is that the splitting of the band is caused by the spin-orbit coupling of electrons.

Let us consider the case that the energy levels of an electron moving in the electrostatic potential $V(\boldsymbol{r})$ of ions prove to be degenerate. Usually, this occurs in those points of the space of the reciprocal lattice that has a high symmetry. The degeneracy might be lifted due to a peculiar relativistic effect called the spin-orbit coupling. This arises from the fact that in a coordinate system moving together with the electron, a small magnetic field is added to the electric field; it appears to be of order $(v/c)\nabla V(\boldsymbol{r})$, where v is the electron velocity, c is the velocity of light, 3×10^{10} cm/s, and $V(\boldsymbol{r})$ is the periodic electrostatic potential of the lattice. This magnetic field interacts with the magnetic moment of the electron and may alter the electronic energy spectrum such as the band splitting mentioned above. The relative value of the correction to the energy is of order $(v/c)^2 f(Z)$, where $f(Z)$ is an increasing function of the atomic number Z. Since $v \sim 10^8$ cm/s, these enegries are usually of the order of $10^{-3} \sim 10^{-2}$ eV.

To understand the spin-orbit coupling, it might be easier to consider the motion of electrons in the vicinity of the nucleus. Consider the velocity of an electron in the $1s$ orbital of an atom with the atomic number Z. If the orbital radius is r of the electron, the following equation is obtained by considering the balance between the centrifugal force and the Coulomb force. That is

$$m\frac{v^2}{r} = \frac{Ze^2}{r^2}. \tag{2.2}$$

The Bohr postulate for the $1s$ electron (the principal quantum number $n = 1$) is

$$mvr = \hbar. \tag{2.3}$$

The orbital radius and velocity are thus obtained as

$$r = \frac{1}{Z}\frac{\hbar^2}{me^2} = \frac{a_{\mathrm{B}}}{Z}, \tag{2.4}$$

$$\frac{v}{c} = Z\frac{e^2}{c\hbar} = \frac{Z}{137}. \tag{2.5}$$

Applying to Cu ($Z = 29$) provides $v/c = 0.21$, and therefore relativistic effects are no longer ignored.

The orbital motion of the electron rotation around the nucleus generates an orbital magnetic moment $-\mu_{\mathrm{B}}\boldsymbol{l}$. On the other hand, in a coordinate system centered on the electron, the nucleus with charge $+Ze$ rotates around the electron. The motion of nucleus generates a magnetic field $\boldsymbol{H}_{\mathrm{Z}}$ at the electron's position and $\boldsymbol{H}_{\mathrm{Z}}$ is expressed by Biot-Savart law as follow;

$$\boldsymbol{H}_{\mathrm{Z}} = \frac{Ze}{c}\frac{\boldsymbol{r}\times\boldsymbol{v}}{r^3} \tag{2.6}$$

$$= \frac{\hbar}{mc}\frac{Ze}{r^3}\left[\boldsymbol{r}\times\boldsymbol{p}\right]. \tag{2.7}$$

The Zeeman energy for the electron due to this magnetic field is expressed as

$$\mathcal{H}_{\mathrm{so}} = g\mu_{\mathrm{B}}\boldsymbol{s}\cdot\boldsymbol{H}_{\mathrm{Z}} \tag{2.8}$$

$$= \frac{\hbar^2 e^2}{m^2c^2}\frac{Z}{r^3}\boldsymbol{s}\cdot\boldsymbol{l}, \tag{2.9}$$

where the spin momentum is $\boldsymbol{\mu}_{\mathrm{s}} = -g\mu_{\mathrm{B}}\boldsymbol{s}$ and the Zeeman energy is $-\boldsymbol{\mu}_{\mathrm{s}}\cdot\boldsymbol{H}_{\mathrm{Z}}$. As can be seen from the sign, this energy is lower when $\boldsymbol{s}$ and $\boldsymbol{l}$ are antiparallel. This interaction between the spin angular momentum $\boldsymbol{s}$ and the orbital angular momentum $\boldsymbol{l}$ is called the spin-orbit coupling. The value of eq. (2.9) is larger than the actually observed value by a factor of 2. With relativistic corrections, it is correctly expressed as follows;

$$\mathcal{H}_{\mathrm{so}} = \frac{\hbar^2 e^2}{2m^2c^2}\frac{Z}{r^3}\boldsymbol{s}\cdot\boldsymbol{l}. \tag{2.10}$$

The electric field $\boldsymbol{E}$ acting on the electron is

$$\boldsymbol{E} = \frac{Ze}{r^3}\boldsymbol{r}. \tag{2.11}$$

By using the $\boldsymbol{E}$, the spin-orbit interaction can be transformed as follows,

$$\mathcal{H}_{\mathrm{so}} = -\frac{\hbar e}{2m^2c^2}\boldsymbol{s}\cdot\left[\boldsymbol{p}\times\boldsymbol{E}\right]. \tag{2.12}$$

More generally, the spin-orbit interaction is given by

$$\mathcal{H}_{\mathrm{so}} = \frac{\hbar}{2m^2c^2}\sum_i \boldsymbol{s}_i\cdot\left[\nabla V(\boldsymbol{r}_i)\times\boldsymbol{p}_i\right], \tag{2.13}$$

where $\boldsymbol{s}_i$, $\boldsymbol{r}_i$, and $\boldsymbol{p}_i$ is the spin, the coordinate, and the momentum of the i-th electron, respectively, and $V(\boldsymbol{r}_i)$ is the potential acting on the i-th electron. Consider an isolated atom with the total spin angular momentum $\boldsymbol{S} = \sum_i \boldsymbol{s}_i$ and the total orbital angular momentum $\boldsymbol{L} = \sum_i \boldsymbol{l}_i$. If we simplify the potential $V(\boldsymbol{r}_i) = -Ze^2/|\boldsymbol{r}_i|$ with the atomic number Z, the equation (2.13) can be written as follows.

$$\mathcal{H}_{\mathrm{so}} = \frac{\hbar}{2m^2c^2} \sum_i \frac{Z}{r_i^3} \boldsymbol{s}_i \cdot [\boldsymbol{r}_i \times \boldsymbol{p}_i] \tag{2.14}$$

$$= \frac{\hbar^2}{2m^2c^2} \sum_i \frac{Z}{r_i^3} \boldsymbol{s}_i \cdot \boldsymbol{l}_i \tag{2.15}$$

This expression is equivalent to the semi-classically obtained expression of eq. (2.9) with relativistic corrections. Defining the expectation value of Z/r^3 as λ for the radial wave function $r\varphi(r)$, we obtain

$$\lambda = \frac{\hbar^2}{2m^2c^2} \left\langle \frac{Z}{r^3} \right\rangle \tag{2.16}$$

$$= \frac{\hbar^2}{2m^2c^2} \int_0^\infty \frac{Z}{r^3} |r\varphi(r)|^2 \, dr. \tag{2.17}$$

Generally expressing, it is as follows;

$$\lambda = \frac{\hbar^2}{2m^{*2}c^2} \int_0^\infty \frac{1}{r} \frac{dV(r)}{dr} |r\phi(r)|^2 dr, \tag{2.18}$$

where $V(r)$ is the sum of the nucleus potential and the classical Coulomb and exchange-correlation potentials. The spin-orbit interaction I_{so} is calculated from following integral,

$$|\mathcal{H}_{\mathrm{so}}| = I_{\mathrm{so}}(r) = \frac{\hbar^2}{2m^{*2}c^2} \int_0^r \frac{1}{r'} \frac{dV(r')}{dr'} |r'\phi(r')|^2 dr'. \tag{2.19}$$

Here we calculate the spin-orbit interaction for the d electrons, not in the lattice but in the isolated atom, following the method presented by Koelling and Harmon [23]. The Z is 45, 77, 32, and 50 for Rh, Ir, Ge, and Sn, respectively. Figure 2.11 shows the radial atomic number wave function $r\phi(r)$. The coupling constant of the spin-orbit coupling $r^2 dV/dr$, and spin-orbit coupling I_{SO} for each atom are shown in Figs 2.12(a) and 2.12(b), respectively. The spin-orbit coupling is obtained to be 12.8 mRy (2020 K) in Rh-4d, 38.0 mRy (6000 K) in Ih-5d, Fig 2.11(c) show that the spin-orbit coupling

reaches the constant value at $r_{\text{const.}} = 0.37$ a.u. for Rh, 0.11 a.u. for Ir, indicating the spin-orbit coupling is determined near the nucleus atom. On the other hand, the $r\phi(r)$ function possesses a maximum value at $r = 0.11$ a.u. for Rh, 0.37 a.u. for Ir, which corresponds to the $r_{\text{const.}}$ The present calculations indicate that the radial wave function of Ir-5d electrons possesses a large distribution at the distance close the center, compared with those of Rh-4d, Ge-4p, and Sn-5p electrons, which produces the relatively large value of the spin-orbit coupling in Ir. Intuitively, it can be understood that the closer the electron is to the nucleus, the faster it is accelerated by the Coulomb potential, resulting in increasing the relativistic effect and the spin-orbit coupling.

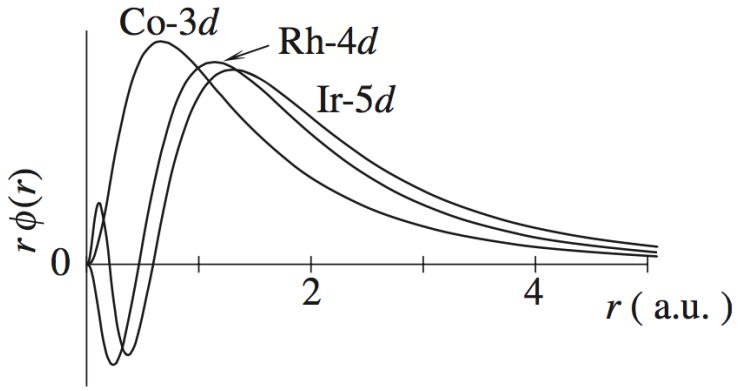

Figure 2.11: Radial wavefunction $r\phi(r)$ as a function of the distance r for Ir-5d, Rh-4d, and Co-3d electrons in the isolated atoms, cited from ref. [2].

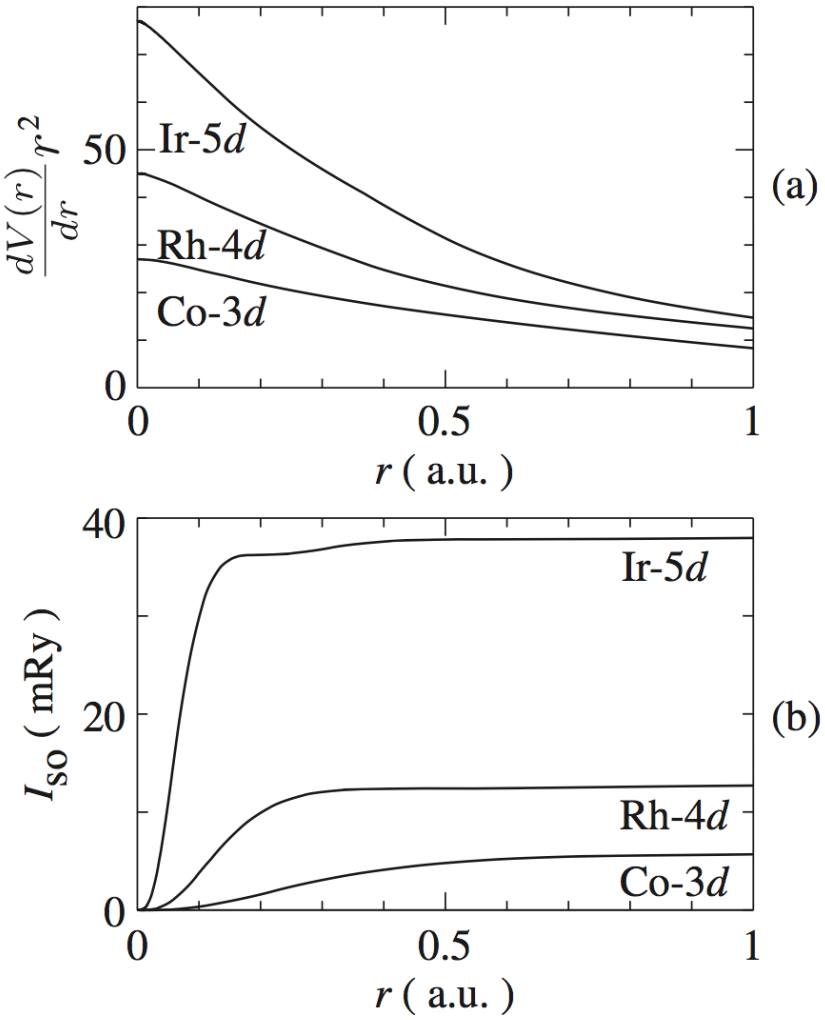

Figure 2.12: (a) Coupling constant of the spin-orbit interaction $\left(d^2V(r)/dr^2\right)r^2$, and (b) the spin-orbit interaction I_{SO} as a function of the r for Ir-5d, Rh-4d, and Co-3d electrons in the isolated atoms, cited from ref. [2]. Simply thinking, $r^2dV(r)/dr$, corresponds to the effective atomic number Z_{eff} in the potential $V(r) = -Z_{eff}/r$. Z_{eff} at $r = 0$ is very close to the atomic number Z in the nuclear potential $V(r) = -Z/r$, where Z is 77, 45, and 27 for Ir, Rh, and Co, respectively.

Figure 2.13 shows the value of λ, or ζ_{cal} as a function of atomic number Z. λ of p electrons are larger than those of d and f electrons. This is because the orbital wave function $r\phi$ of p electron has a large value near the atomic center compared to those of d and f electrons. In other words, the spin-orbit coupling is larger when l is smaller. Comparing the elements with the same main quantum number n and azimuthal quantum number l, the larger Z is, the larger the spin-orbit coupling is.

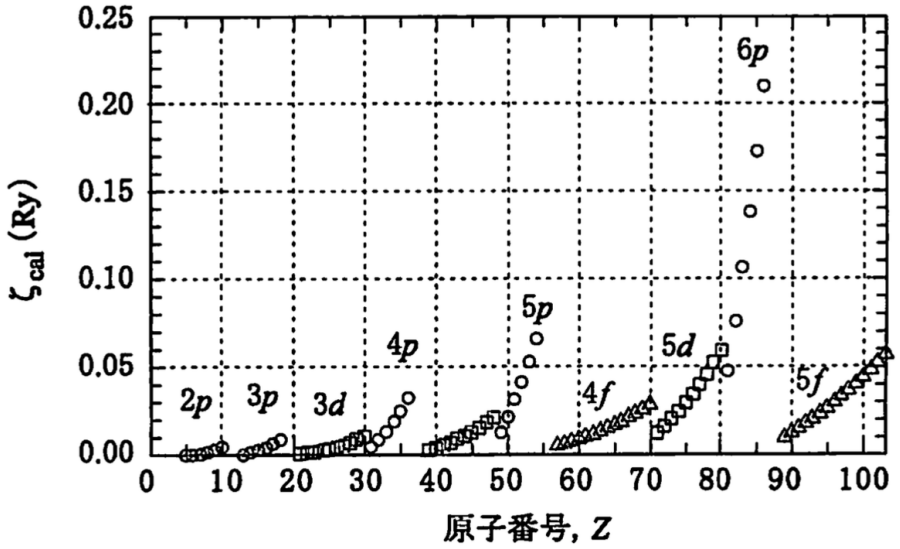

Figure 2.13: Spin-orbit interaction ζ_{cal} as a function of atomic number Z. Note that ζ_{cal} corresponds to λ in eq. (2.18), cited from ref. [24].

Antisymmetric spin-orbit interaction

The result of spin-orbit interaction for isolated atoms mentioned above is also applicable to the crystalline lattice with noncentrosymmetric symmetry. In this case, the magnitude of the antisymmetric spin-orbit interaction that alters the degenerate Fermi surface into two Fermi surfaces is roughly proportional to the spin-orbit interaction in eq. (2.19). Since the band structure calculation uses, in principle, the same potential $V(\boldsymbol{r})$ as mentioned above. When the antisymmetric spin-orbit interaction, mentioned above very frequently, is at work, the splitting of Fermi surfaces with very similar topology to each other but with different volumes occurs. The following therm of the antisymmetric spin-orbit interaction

$$\mathcal{H}_{\mathrm{so}} = -\frac{\hbar}{4m^{*2}c^2}\left(\nabla V(\boldsymbol{r}) \times \boldsymbol{p}\right) \cdot \boldsymbol{\sigma} \tag{2.20}$$

$$= \alpha\left(\boldsymbol{n} \times \boldsymbol{p}\right) \cdot \boldsymbol{\sigma}, \tag{2.21}$$

where α is the strength of the spin-orbit interaction, $\boldsymbol{n}$ is the unit vector for the $\nabla V(r)$ direction, and $\boldsymbol{\sigma}$ is the Pauli matrix, is added to the Hamiltonian for conduction electrons, as follows;

$$\varepsilon_{\boldsymbol{p}} = \frac{\boldsymbol{p}^2}{2m^*} + \alpha\left(\boldsymbol{n} \times \boldsymbol{p}\right) \cdot \boldsymbol{\sigma}, \tag{2.22}$$

where $\boldsymbol{p} = \hbar\boldsymbol{k}$. Here, $\alpha\,(\boldsymbol{n} \times \boldsymbol{p}) \cdot \boldsymbol{\sigma}$ is described as $\alpha \boldsymbol{g}(\boldsymbol{k})$.

With the splitting of the band, the Fermi surface also splits into two Fermi surfaces due to the antisymmetric spin-orbit interaction. The spin direction of each band is antisymmetric with respect to $\boldsymbol{k}$. This strong coupling between spin and momentum is called spin-momentum locking, and the wave number dependence of the spin on the Fermi surface is called spin texture. The spin texture is also described by $\alpha \boldsymbol{g}(\boldsymbol{k})$. Figure 2.14(c) shows Fermi surfaces with Rashba-type antisymmetric spin-orbit interaction appearing in the polar point groups $C_{3\mathrm{v}}$, $C_{4\mathrm{v}}$ and $C_{6\mathrm{v}}$. On the Fermi surface with constant k_z, the spins rotate clockwise and counterclockwise, corresponding to up-spin and down-spin, respectively. Figure 2.14(d) shows the spin texture appearing in the point group D_3 to which this research object of TrX_4 systems belongs. The spin direction is perpendicular to the Fermi surface and shows inward and outward directions, respectively. This spin texture is called the hedgehog or Zeeman type. Note that the Fermi surface for the centrosymmetric compound is degenerated under $H = 0$, as shown in Fig. 2.14(a), but splits into two Fermi surfaces with up ($\uparrow$) and down ($\downarrow$) spin states in magnetic field, as shown in Fig 2.14(b). The splitting of the Fermi surface is described next.

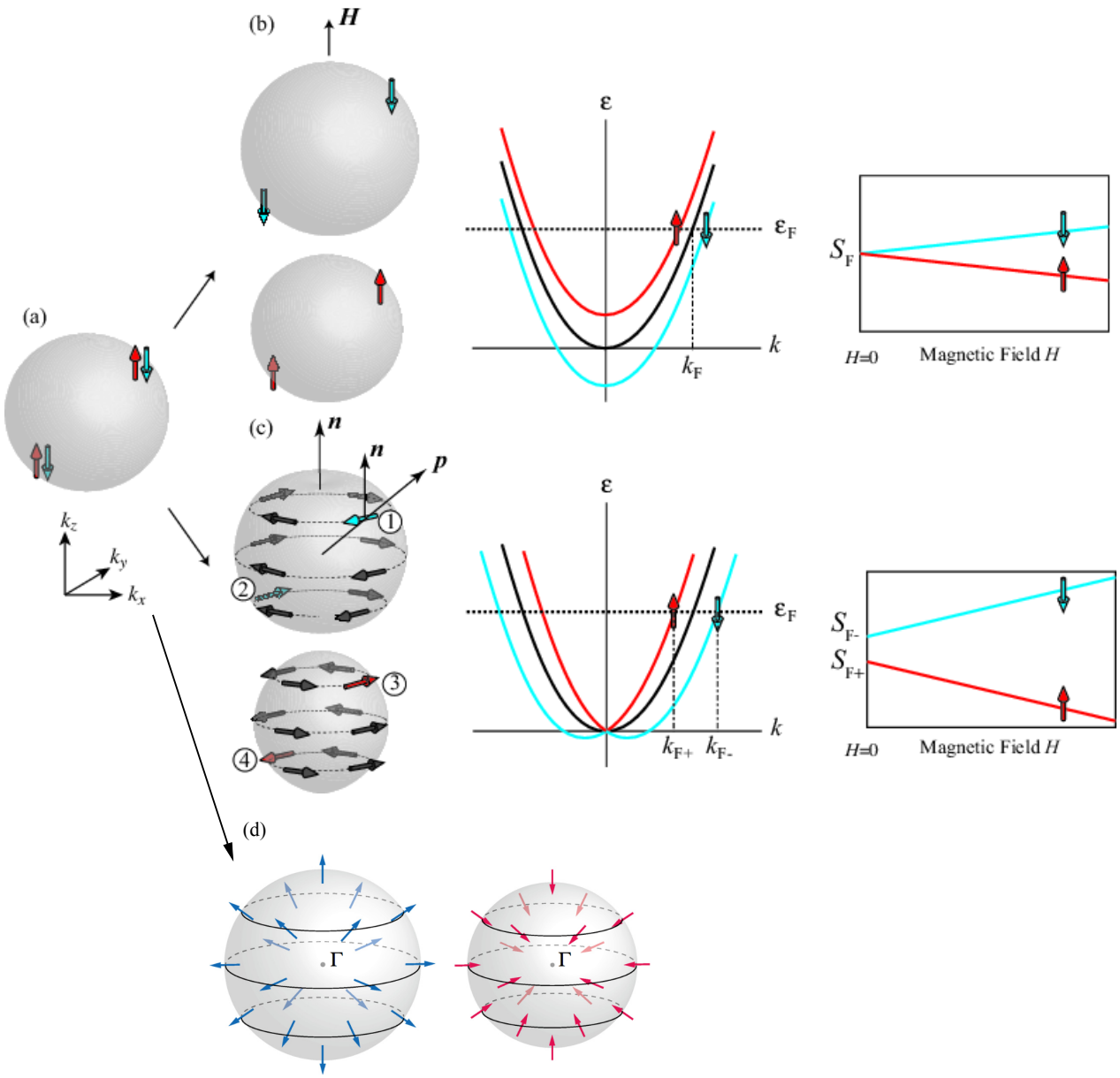

Figure 2.14: (a) Spherical Fermi surface with generated up (↑) and down (↓) spin state, and (b) the Fermi surface and the corresponding energy band split into two components depending on the up- and down-spin states when the magnetic field H is applied to the material. The maximum cross-sectional areas S_{F} are also split into two components as a function of the magnetic field, well known as Zeeman splitting. The Fermi surface and the corresponding energy band are split into two components depending on the up- and down-spin states due to (c) the Rashba-type and (d) the hedgehog type of the antisymmetric spin-orbit interaction even when $H = 0$. The field dependence of the maximum cross-sectional areas $S_{\mathrm{F}-}$ and $S_{\mathrm{F}+}$ are also shown in the noncentrosymmetric structure, after courtesy of Y Ōnuki and cited from ref. [9].

Splitting of Fermi surface

Figure 2.14(a) is a spherical Fermi surface with up- and down-spin states degenerated at zero magnetic field for the centrosymmetric compound. Under an external magnetic field, the energy band and corresponding the Fermi surface splits into majority and minority spin states in the magnetic field, as shown in Fig 2.14(b).

In the noncentrosymmetric compound, the Fermi surface splits into two Fermi surfaces at zero magnetic field, as shown in Figs. 2.14(c) and 2.14(d), which is based on the antisymmetric spin-orbit interaction. The dHvA frequency F also splits into F_+ and F_-. From the relations $m^* = \left(\hbar^2/2\pi\right)\partial S/\partial\varepsilon$, $S = (2\pi e/c\hbar)\,F$, we have the following

$$\begin{aligned}\Delta\varepsilon &= \frac{\hbar^2}{2\pi m^*}\Delta S \\ &= \frac{\hbar e}{m^* c}\Delta F \\ &= \frac{\hbar e}{m^* c}|F_+ - F_-|. \end{aligned} \tag{2.23}$$

Here, $\Delta\varepsilon$ is the magnitude of the antisymmetric spin-orbit interaction and can be determined from the dHvA frequencies and the cyclotron effective masses of the split Fermi surfaces.

Fermi surface properties and the magnitude of the antisymmetric spin-orbit interaction for La*Tr*Ge$_3$ (*Tr*: Co, Rh, Ir) were investigated [2]. La*Tr*Ge$_3$ crystallizes in the BaNiSn$_3$-type structure, as shown in Fig. 2.7(b), whose space group is $I4/mm$ (No. 107) and crystal point group is C_{4v}. Similar to CePt$_3$Si, there is no mirror symmetry in the c-axis direction. The angular dependences of dHvA frequencies of the Fermi surface are essentially the same among La*Tr*Ge$_3$ (*Tr*: Co, Rh, Ir), as shown in Fig. 2.15. This is plausible because the valence electron configuration of La*Tr*Ge$_3$ is $3d^7 4s^2$ for Co, $4d^8 5s^1$ for Rh, and $5d^9$ for Ir, with no difference in the number of valence electrons. The dHvA frequency of the main branch α for LaCoGe$_3$ is, however, slightly smaller than those of LaRhGe$_3$ and LaIrGe$_3$, namely, the Fermi surface of LaCoGe$_3$ is slightly smaller in volume than those of LaRhGe$_3$ and LaIrGe$_3$. Moreover, it should be noted that the width of the split dHvA frequency $|F_+ - F_-|$ of the branch α for LaIrGe$_3$ is larger than those for LaCoGe$_3$ and LaRhGe$_3$. Therefore, the antisymmetric spin-orbit interaction $\Delta\varepsilon$ in LaIrGe$_3$ is larger than those in LaCoGe$_3$ and LaRhGe$_3$. Here, the magnitude of $\Delta\varepsilon$ of branch α is 460 K for LaCoGe$_3$, 510 K for LaRhGe$_3$, and 1090 K for LaIrGe$_3$. A large antisymmetric spin-orbit interaction of LaIrGe$_3$ due to both the characteristic

radial wave function $\phi(r)$ of the Ir-5d electrons near the nuclear center and the relatively large effective atomic number Z of Ir [2].

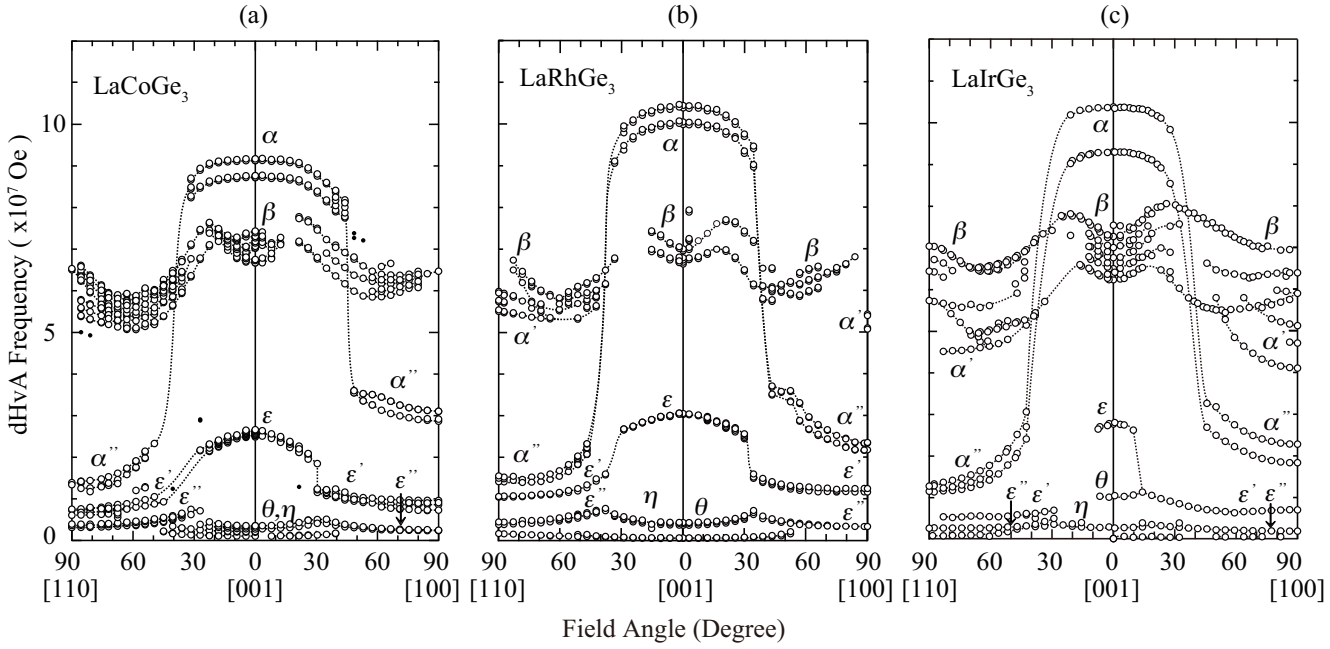

Figure 2.15: Angular dependences of dHvA frequencies in $LaCoGe_3$, $LaRhGe_3$, and $LaIrGe_3$, cited from ref. [2].

In the noncentrosymmetric crystal structures, typical examples are of the Rashba-type mentioned above and chiral nature. The spins in the chiral structure are directed from the Γ point (center of the Brillouin zone) to outside for one Fermi surface, as in Fermi velocity, while spins are centered in the Γ point for the other Fermi surface, as shown in Fig 2.14(d) [9]. Note that this is applicable to a special case. Namely, the Fermi surface is spherical and exists in the Γ point in the Brillouin zone.

Next, we present three cases. The first case is the hexagonal chiral structure. $CrSi_2$, VSi_2, and $TaSi_2$ belongs to $P6_422$, while only $NbSi_2$ belongs to $P6_222$, as shown in Fig. 2.16. Note that the crystal structure in Fig. 2.16(c) for $TaSi_2$ and VSi_2 and the structure in Fig. 2.16(d) for $NbSi_2$ are mirror-symmetryc.

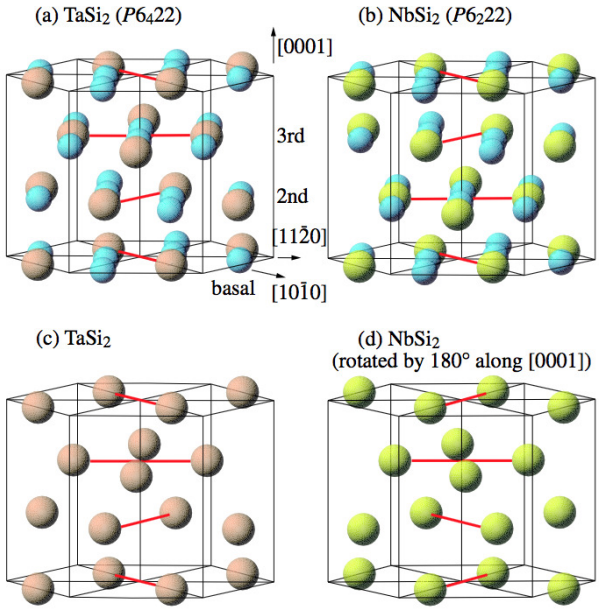

Figure 2.16: Crystal structure of (a) $TaSi_2$, VSi_2, and $CrSi_2$ ($P6_422$), (b) VSi_2 (6_222), (c) Ta (V, Cr) atoms in $TaSi_2$ (VSi_2, $CrSi_2$) for simplicity and (d) Nb atoms in $NbSi_2$, rotated the crystal structure by 180° along the [0001] direction, cited from ref. [9].

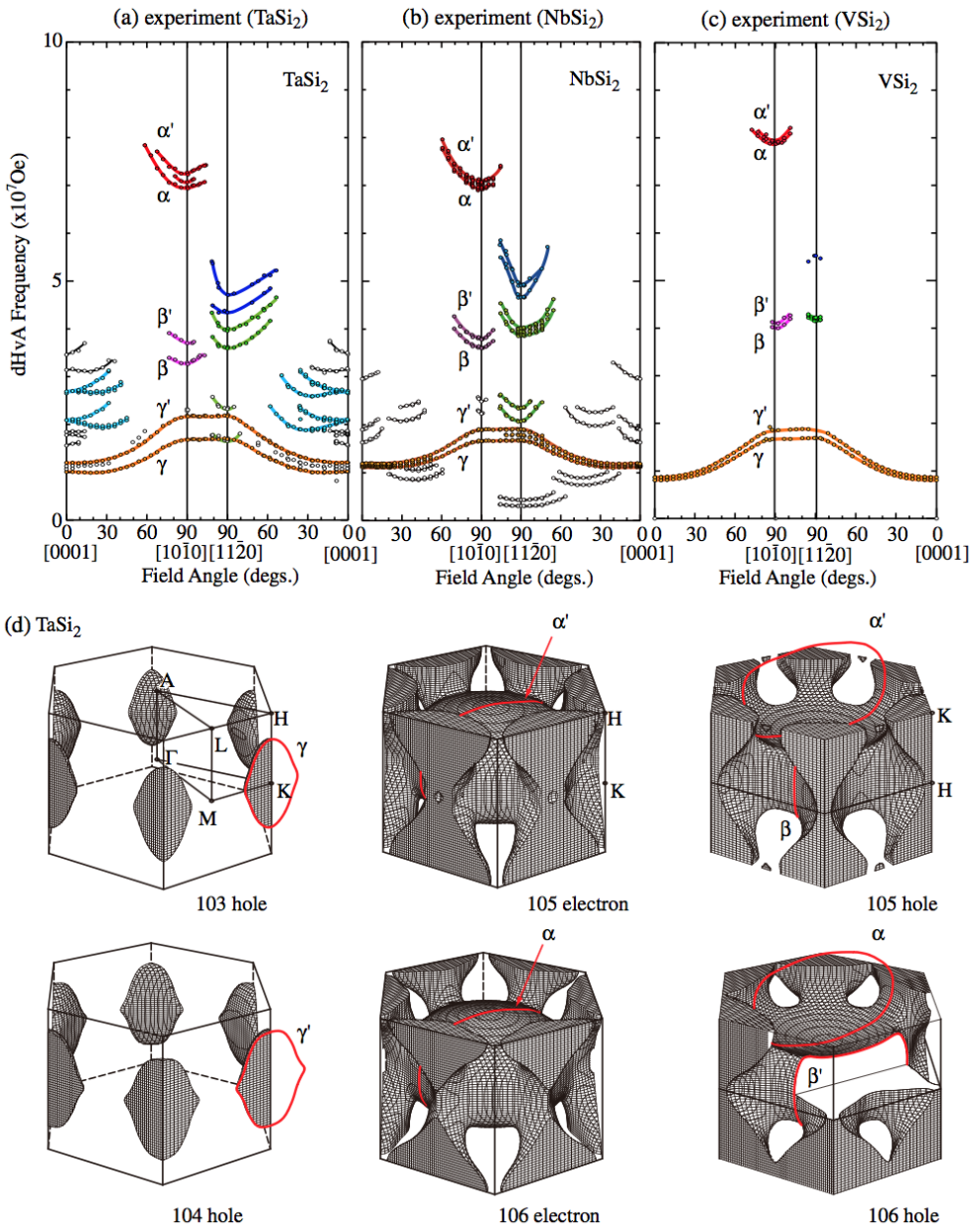

Figure 2.17: Angular dependences of the dHvA frequencies in (a) $TaSi_2$, (b) $NbSi_2$, and (c) VSi_2 and (d) the theoretical Fermi surfaces in $TaSi_2$, cited from ref. [9]

Figure 2.17 shows the angular dependences of dHvA frequencies in $TaSi_2$, $NbSi_2$, and VSi_2 and the corresponding theoretical Fermi surfaces. A magnitude of the spin-orbit interaction or a splitting energy between two main Fermi surfaces named $\alpha(\alpha')$ is experimentally determined to be 493 K in $TaSi_2$, 209 K in $NbSi_2$, and 19 K in VSi_2. The splitting energy is large in Ta-5*d* conduction electrons than those in the Nb-4*d* and

V-3d electrons.

Since the crystal point group $D_6(222)$ provides $\boldsymbol{g}(\boldsymbol{k}) = \alpha_1(k_x\hat{x} + k_y\hat{y}) + \alpha_2 k_z\hat{z}$, the hedgehog-like spin texture is expected to realize near the Γ point. The spin textures of conduction electrons are theoretically calculated, as shown in Fig 2.18. We remark the cross-sections of the bands 103- and 104- hole Fermi surfaces at the K point in the hexagonal basal plane. The directions of the spins are approximately opposite each other between two split Fermi surfaces, but the direction of the band 104-hole Fermi surface do not simply directed toward the K point, This is because the corresponding cross-section is not a circle but a triangle.

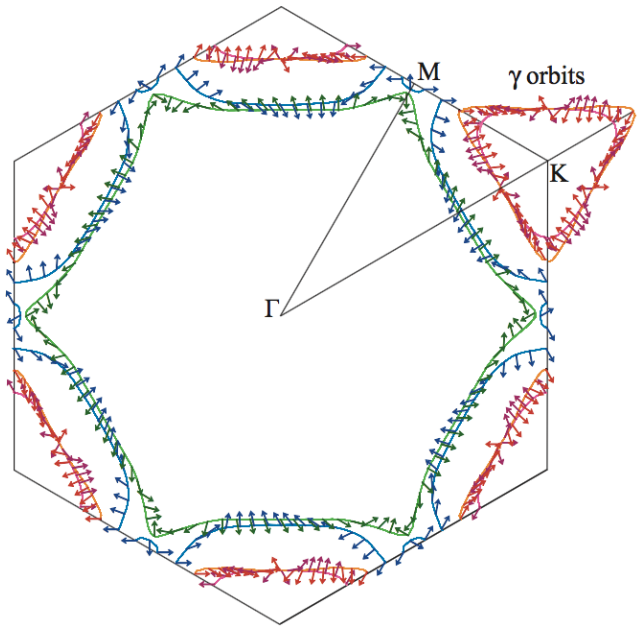

Figure 2.18: Cross-section and the spin structure in the $k_z = 0$ plane calculated for the Fermi surfaces of $TaSi_2$, cited from ref. [25]

The next case is the cubic chiral structure in EuPtSi, which is known to exhibit the magnetic skyrmion as in MnSi. The crystal structure of EuPtSi is the ullmannite NiSbS-type or LaIrSi-type chiral structure (space group: $P2_13$, No. 198, T^4), described later [26, 27]. Since this crystal structure has neither spatial inversion symmetry nor mirror symmetry, chiral (left- and right-handed) structures are allowed for this compound. As for NiSbS, the left panel of Fig 2.19(a) shows the crystal for as-grown single-crystalline sample, meaning that there was no mixing of both-handed crystals. Figures 2.19(b) and 2.19(c) show the crystal structures of MnSi and as-grown EuPtSi single-crystalline samples, respectively. These compounds belong to the same space

group in the crystal structure. As for EuPtSi, the four Eu atoms form a tetrahedron, and the four Si atoms also form a similar tetrahedron, and they are combined, as shown in Fig 2.19(c). Eight Pt atoms are at the corners of the cubic structure, and three Pt atoms are located very close to the fcc atomic sites. The fourfold symmetry in the {100} plane is lost, but there is threefold rotational symmetry around the ⟨111⟩ direction in this chiral cubic structure.

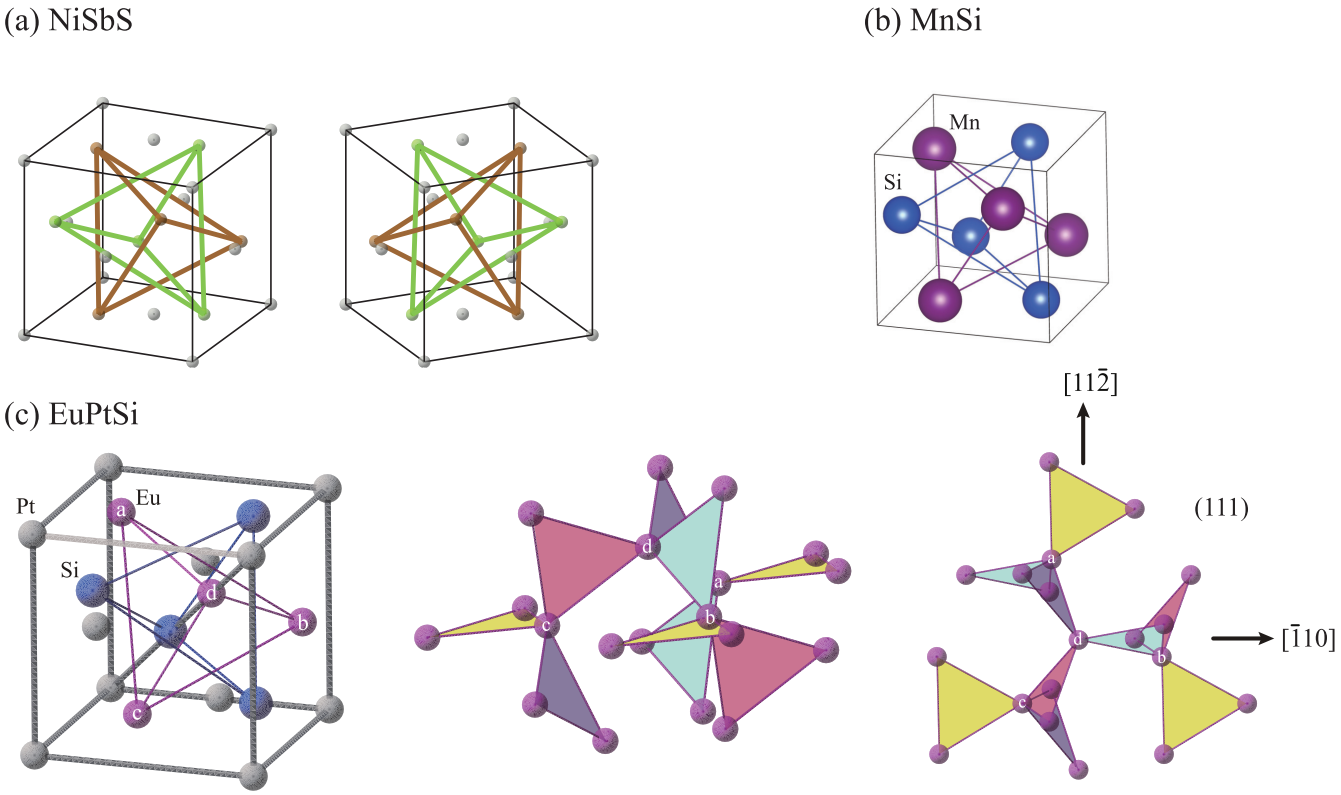

Figure 2.19: (a) Crystal structures of right-handed and left-handed NiSbS. (b) structure of MnSi, and (c) structure of EuPtSi where red spheres labeled a, b, c, and d represent Eu atoms, gray ones are Pt atoms, and blue ones are Si atoms, cited from ref. [28].

Fermi surface properties are characteristic in EuPtSi. In the previous studies on NiSbS and PdBiSe with the same ullmannite-type crystal structure as EuPtSi, it was found that each Fermi surface splits into two different Fermi surfaces. This splitting of the Fermi surface is due to the noncentrosymmetric (cubic chiral) crystal structure of these compounds. The energy difference between two splits of nearly spherical Fermi surfaces named α, and α' was estimated to be 200 K for NiSbS and 1050 K for PdBiSe for $H \parallel [100]$ or [001]. Note that the splitting energy is highly different, depending on the compound. This difference can be explained by the difference in the spin-orbit coupling of the constituent elements. The spin-orbit interactions for Ni-3d, Sb-5p, and

S-3p electrons in NiSbS are smaller than those for Pd-4d, Bi-6p, and Se-4p electrons in PdBiSe.

Figure 2.20(a) and 2.20(b) show typical dHvA oscillations for $H \parallel [001]$ and the corresponding FFT spectrum in EuPtSi, respectively [29, 28]. The dHvA frequency $F(= c\hbar S_{\rm F}/2\pi e)$ is proportional to the maximum or minimum cross-sectional area $S_{\rm F}$ of the Fermi surface, which is expressed as a unit of the magnetic field. The main dHvA branches were identified as α, α', β_2', $\beta(\beta_1')$, and so forth, by comparing with theoretical Fermi surfaces for the non-4f reference compound SrPtSi shown in Fig 2.20(d) and 2.20(e). The angular dependences of the dHvA frequency were studied by rotation of a single-crystalline sample with respect to the magnetic field. Figure 2.20(c) show experimentally observed angular dependences of dHvA frequency. The dHvA branches were observed in the whole field direction. This means that all the observed dHvA branches correspond to closed Fermi surfaces, namely, the Fermi surfaces are corrugated but nearly spherical. These dHvA branches are theoretically explained for SrPtSi, as shown in Figs. 2.20(d) and 2.20(e).

The cyclotron effective mass for each dHvA branch was determined from the temperature dependence of dHvA amplitude. The cyclotron effective masses were 0.96 m_0 for branch α and 0.88 m_0 for branch α'. The energy difference $\Delta\varepsilon$ for two split dHvA branches α and α' (or two split Fermi surfaces) was estimated to be $\Delta\varepsilon = (\hbar e/m_c^* c)|F_+ - F_-| = 1200$ K.

The spintexture of conduction electrons in EuPtSi is theoretically calculated. Here, we focus on the main band-121 and band-122 electron Fermi surfaces (α and α') at the Γ point in Figs. 2.20(f) and 2.20(g). Colors on the Fermi surface indicate the spin orientation. Color values of red, green, and blue correspond to the magnitudes of S_x, S_y, and S_z, respectively. Spins on these Fermi surfaces are complementary, exhibiting the opposite spin hedgehog structure, as shown in Figs. 2.20(f) and 2.20(g). These spin structures can be seen more clearly in the cross-sectional views of α and α' Fermi surfaces, as shown in Figs. 2.20(h)-(k). In these figures, direction and magnitude of spins are projected in the (001) and (111) planes. In the (001) plane, spins on the Fermi surface of branch α point to the Γ point, whereas spins on the Fermi surface of branch α' point to outside. These are ideal cases for the chiral structure.

On the other hand, spin directions for $H \parallel [111]$ are similar to those of the Rashba-type spin texture, as shown in Figs 2.20(j) and 2.20(k). Spins on the Fermi surface of branch α circulate counterclockwise with rotations, while spins on the Fermi surface of branch α' circulate clockwise with rotations [30].

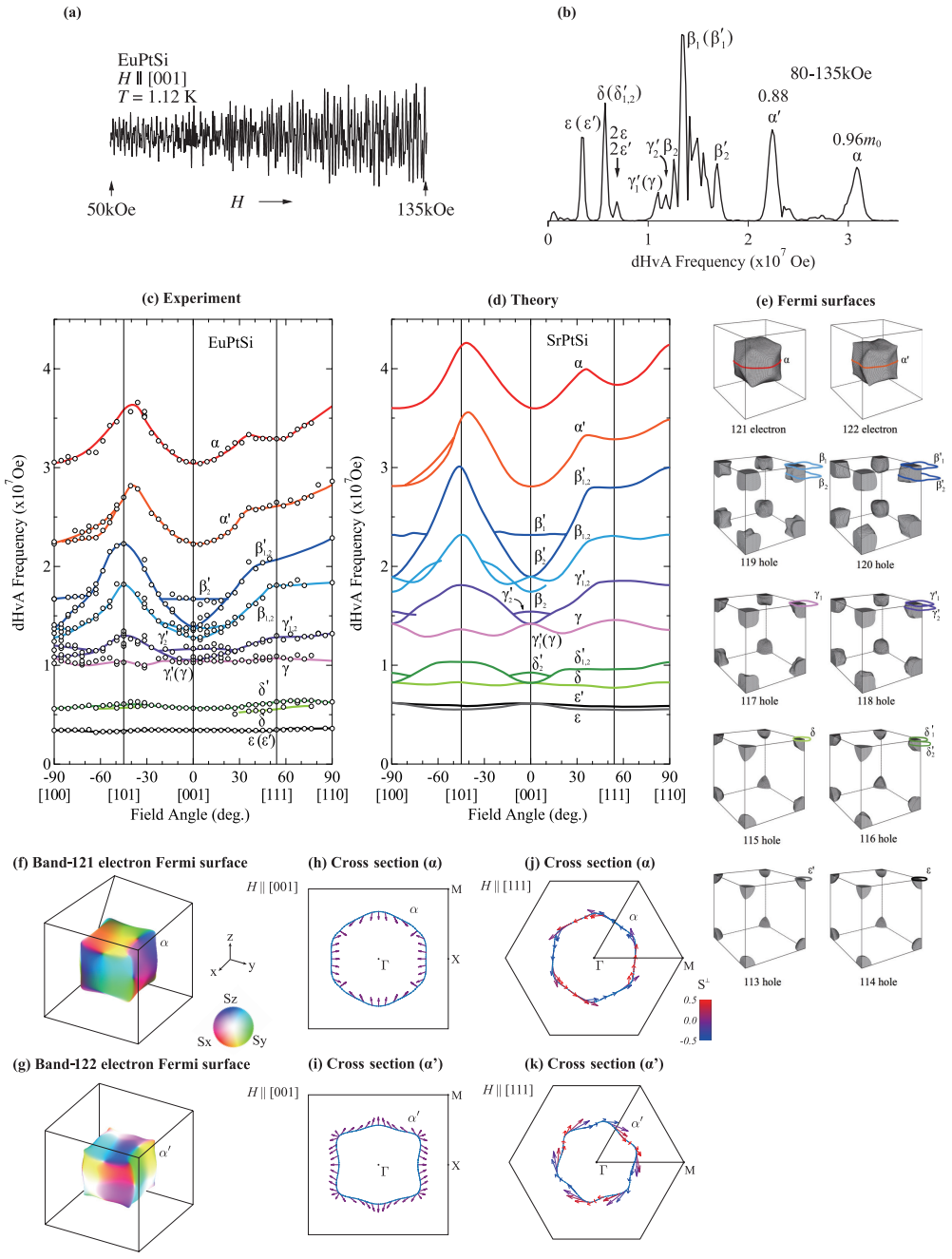

Figure 2.20: (a) dHvA oscillations for $H \parallel [001]$ and (b) the corresponding FFT spectrum for EuPtSi. (c) Detected angular dependences of the dHvA frequency, (d) theoretical angular dependences of dHvA frequency for SrPtSi, and (e) corresponding theoretical Fermi surfaces and spin textures for (f) band-121 (branch α) and (g) band-122 (branch α') Fermi surfaces, (h) and (i) cross-sectional views of the spin texture in the (001) plane, and (j) and (k) those in the (111) plane for SrPtSi, cited from ref. [30].

Spin textures on the Fermi surface can be observed using spin angle-resolved photoemission spectroscopy (SARPES). Recently, the research for Te has been studied extensively [31, 32]. The crystal structure of Te is shown in Fig. 2.10. The space group belongs to $P3_121$ (No. 152) or $P3_221$ (No. 154), and the crystal structure is a chiral structure. A calculated the Fermi surface on the basis of the result of SARPES show the spin orientations is opposite between left- and right-handed crystal: In the left-handed crystal, the spin orientation is outward from the center, whereas in the right-handed system, the spin orientation is inward to the center. The crystal point group of Te is D_3, giving $\alpha \boldsymbol{g}(\boldsymbol{k}) = \alpha_1(k_x\hat{x} + k_y\hat{y}) + \alpha_2 k_z\hat{z}$, which is consistent with the experimental result.

2.4 Superconductivity, magnetic, and transport properties of Noncentrosymmetric compunds

Noncentrosymmetric compounds exhibit characteristic superconductivity, magnetic, and transport properties such as the huge upper critical field H_{c2} in $CeIrSi_3$, magnetic skyrmion in MnSi and EuPtSi, and magnetochiral anisotropy.

Huge upper critical field H_{c2} in $CeIrSi_3$ amd related compounds

The BCS theory of superconductivity, which was proposed by Barden, Cooper, and Schrieffer in 1957, is based on the following idea [33]. When an attractive interaction between fermions is present, the stable ground state is no longer the degenerate Fermi gas but a coherent state in which the electrons are combined into pairs of spin-singlets with zero total momentum ($\boldsymbol{k}\uparrow, -\boldsymbol{k}\downarrow$: Cooper pairs). The conduction electrons distort the lattice by moving in the lattice and attracting the positive ion. This distortion attracts another conduction electron. Namely, the interaction between two electrons mediated by the phonon forms the Cooper pair of the two electrons. A BCS-type superconductor has an isotropic superconducting gap which is opened over the entire Fermi surface. Superconductivity was regarded as one of the well-known many-body problems. The BCS-supercinductivity has been, however, altered in heavy fermion superconductors. The pairing mechanism is not due to phonons. These alternative mechanisms are as follows: pairing mechanism correlated with antiferromagnetism (or antiferromagnetic fluctuations), ferromagnetism vs superconductivity, quadrupole interaction vs superconductivity, and a nobel pairing state in the noncentrosymmetric crystal structure. Here we describe the superconductivity in $CeIrSi_3$.

First, we summarize the BCS-superconductivity. In the superconducting state, the

Fermi surface shrinks by

$$\Delta = 2\hbar\omega_{\mathrm{D}} e^{-\frac{1}{D(\varepsilon_{\mathrm{F}})V}}, \tag{2.24}$$

where ω_{D} ($\hbar\omega_{\mathrm{D}} = k_{\mathrm{B}}\theta_{\mathrm{D}}, \theta_{\mathrm{D}}$; Debye temperature of about 10^2 K) is the Debye cutoff frequency, $D(\varepsilon_{\mathrm{F}})$ is the density of states at Fermi energy ε_{F} of about 10^4 K, and the interaction of the two electrons V is attractive ($V > 0$). Following the BCS theory, a superconducting energy gap 2Δ is produced at 0 K

$$2\Delta = 4\hbar\omega_{\mathrm{D}} e^{-\frac{1}{D(\varepsilon_{\mathrm{F}})V}}. \tag{2.25}$$

This means that depaired electrons occupy the electronic states separated by Δ from the Fermi energy, or by 2Δ from the highest energy levels of the Fermi surface.

The superconducting transition temperature T_{sc} in the BCS theory is obtained for $\Delta(T = T_{\mathrm{sc}}) \to 0$,

$$k_{\mathrm{B}} T_{\mathrm{sc}} = 1.13\hbar\omega_{\mathrm{D}} e^{-\frac{1}{D(\varepsilon_{\mathrm{F}})V}}. \tag{2.26}$$

The Debye cutoff frequency ω_{D} is proportional to $M^{-1/2}$ (M: atomic mass). The well-known isotope effect is naturally explained by the BCS theory, namely, $T_{\mathrm{sc}} \sim M^{-1/2}$. Since 2Δ in eq. (2.25) and $k_{\mathrm{B}}T_{\mathrm{sc}}$ in eq. (2.26) have the same form, the ratio is independent of $D(\varepsilon_{\mathrm{F}})$ and V, revealing the parameters free value

$$\frac{2\Delta}{k_{\mathrm{B}} T_{\mathrm{sc}}} = 3.53. \tag{2.27}$$

The temperature dependence of the specidic heat C and the nuclear spin-lattice relaxation rate $1/T_1$, obeys the exponential law. The electronic specific heat based on $C_e = \gamma T$ in the normal state possesses a jump at T_{sc}, ΔC is expressed as

$$\frac{\Delta C}{C(T = T_{\mathrm{sc}})} = \frac{\Delta C}{\gamma T_{\mathrm{sc}}} = 1.43. \tag{2.28}$$

This is a result of the weak coupling BCS theory. Note that the BCS superconductivity is based on the weak coupling of the electron-phonon interaction, which produces a relation of $2\Delta/k_{\mathrm{B}}T_{\mathrm{sc}} = 3.53$ and $\Delta C/\gamma T_{\mathrm{sc}} = 1.43$. In the exact superconductor, the electron-phonon coupling is not always weak. Strong-coupling superconductors exists: Pb, for example, $CeIrSi_3$ shown later.

The temperature dependence of the electronic specific heat C_e below T_{sc} is

$$C_e \sim T^{-\frac{3}{2}} e^{-\Delta/k_{\mathrm{B}}T} (T < 0.1T_{\mathrm{sc}}) \tag{2.29}$$

$$C_e \sim e^{-\Delta'/k_{\mathrm{B}}T} (0.2 < T < 0.5T_{\mathrm{sc}}), \tag{2.30}$$

where eq. (2.29) is an expression based on the BCS theory at $T << T_{\rm sc}$, but eq. (2.30) is an empirical one. The gap Δ' in eq. (2.30) is not the same as Δ but is close to Δ. The nuclear spin-lattice relaxation rate $1/T_1$ is expressed below $T_{\rm sc}$ as

$$\frac{1}{T_1} \sim e^{-\frac{\Delta}{k_{\rm B}T}}. \tag{2.31}$$

Heavy fermion superconductors are known not to display an exponential dependence as predicted by the BCS theory but to follow the power law for C_e and $1/T_1$ [34],

$$C_e = \begin{cases} \sim T^3 & \text{(axial type, point node)} \\ \sim T^2 & \text{(polar type, line node)} \\ \sim T & \text{(gapless)} \end{cases} \tag{2.32}$$

$$\frac{1}{T} = \begin{cases} \sim T^5 & \text{(axial type, point node)} \\ \sim T^3 & \text{(polar type, line node)} \\ \sim T & \text{(gapless)} \end{cases} \tag{2.33}$$

This indicates the existence of an anisotropic gap, namely the existence of a node in the energy gap. When we compare the phonon-mediated attractive interaction based on the BCS theory with the strong repulsive interaction among the heavy fermions, it is theoretically difficult for the former interaction to overcome the latter one. To avoid a large overlap of the wave functions of the paired particles, the heavy fermion system would rather choose an anisotropic channel, like a p-wave spin triplet or a d-wave spin singlet state, to form Cooper pairs.

Typical superconductors of compounds are not pure compounds with elemental superconductors. When decreasing the magnetic field for these superconductors, superconductivity will spontaneously nucleate at $H = H_{\rm c2}$,

$$H_{\rm c2} = \frac{h/e^*}{2\pi\xi^2} = \frac{\phi_0}{2\pi\xi^2} = \sqrt{2}\kappa H_{\rm c}, \tag{2.34}$$

where $e^* = 2e$, $\kappa = \lambda/\xi$ is a Ginzburg-Landau (GL) parameter [35], λ is the London penetration depth, ξ is the width of the superconducting order parameter, called the coherence length, and $H_{\rm c}$ is the thermodynamic critical field. If $\kappa > 1/\sqrt{2}$, $H_{\rm c2}(> H_{\rm c})$ is realized and the corresponding superconductor is called the type-II, while the type-I is in the case of $\kappa < 1/2$. The type-II superconducting properties are the main subject

of this thesis. The type-II superconductor is in the vortex state for $H_{c1} < H < H_{c2}$. Below the lower critical field H_{c1}, the magnetic field is expelled as in the type-I superconductor. The vortex is a normal phase with a cylindrical shape of radius ξ. As for the upper critical field H_{c2}, we note the conventional analyses. From the slope of the upper critical field $(-dH_{c2}/dT)_{T=T_{sc}}$, we can estimate the $H_{c2}(0)$ value. The temperature dependence of $\mu_0 H_{c2}(T)$ was theoretically discussed by Werthamen, Helfand, and Hohenberg (known as WHH) [36, 37]. The upper critical field at $T = 0\ K$, $H_{c2}(0)$, can be described using the WHH formula:

$$\mu_0 H_{c2}(0) = 0.7 \left| \frac{dH_{c2}}{dT} \right|_{T_{sc}} \cdot T_{sc}. \tag{2.35}$$

Here we described briefly the superconducting properties of $CeIrSi_3$ with the Rashba-type tetragonal structure [38, 39]. We show in Fig. 2.21 the pressure dependence of (a) the Néel temperature T_N and the superconducting transition temperature T_{sc}, (b) the jump in specific heat at T_{sc}, and (c) the superconducting upper critical field $H_{c2}(0)$ at 0 K for the [001] direction in $CeIrSi_3$ [38, 39]. The critical pressure at which T_N becomes 0 K is estimated to be $P_c = 2.25$ GPa. On the other hand, T_{sc} reaches its maximum at about 2.6 GPa. At the same time, the jump in specific heat at T_{sc} is very large, $\Delta C_{ac}/C_{ac}(T_{sc})$=5.8 at 2.58 GPa, indicating strong-coupling superconductivity, as shown in Fig. 2.21(b). Note that in BCS theory $\Delta C/C(T_{sc}) = \Delta C/\gamma T_{sc} = 1.43$. Also, as shown in Fig. 2.21(c), the upper critical field $H_{c2}(0)$ for $H \parallel [001]$ is maximum at $P_c^* = 2.63$ GPa.

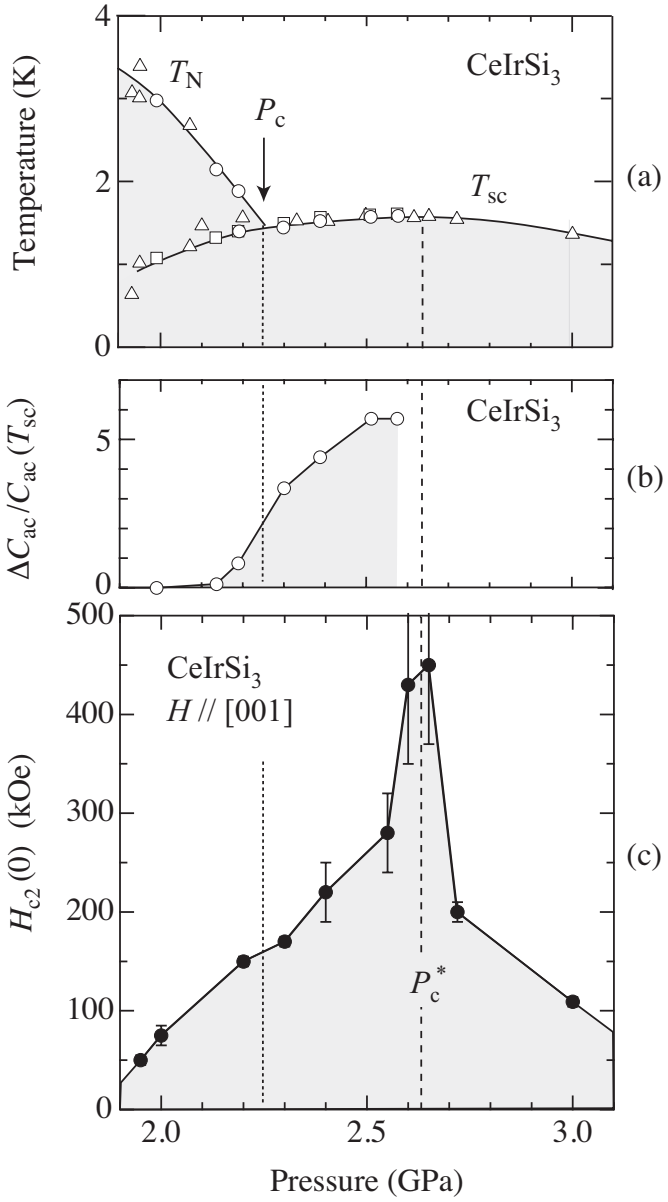

Figure 2.21: Pressire dependences of (a) Néel temperature T_N and superconducting transition temperature T_{sc}, (b) specific heat jump $\Delta C_{ac}/C_{ac}(T_{ac})$, and (c) the upper critical field $H_{c2}(0)$ for $H \parallel [001]$in $CeIrSi_3$, cited from refs. [38, 39].

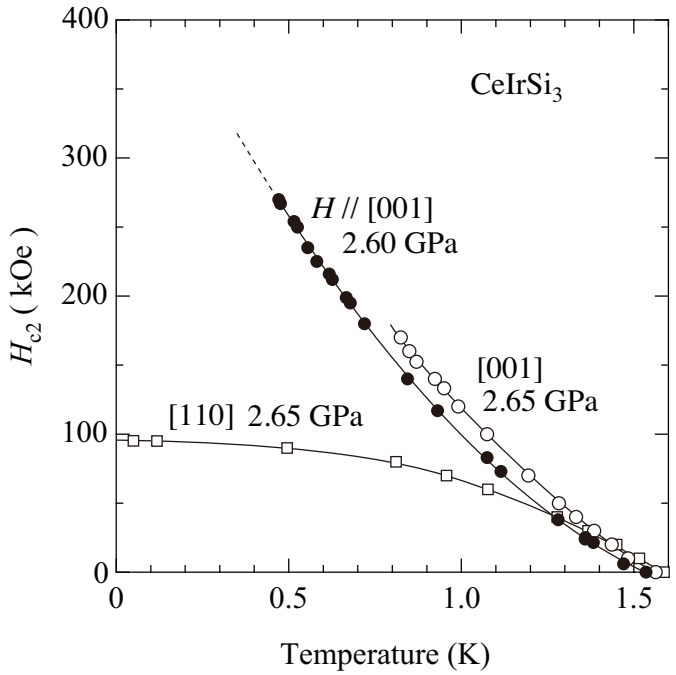

Figure 2.22: a
t 2.65 GPa in $CeIrSn_3$.]Temperature dependences of upper critical field H_{c2} for the magnetic field along [001] at 2.65 GPa in $CeIrSn_3$, cited from ref [38].

The superconducting properties in magnetic fields are highly anisotropic, as shown in Fig. 2.22 [38]. For example, as mentioned above, the upper critical field around $P_c^* \simeq 2.6\,\mathrm{GPa}$ is $H_{c2}(0) = 450\,\mathrm{kOe}$ for $H \parallel [001]$, while $H_{c2}(0) = 95\,\mathrm{kOe}$ for $H \parallel [110]$. Also, the slope $(-dH_{c2}/dT)_{T=T_{sc}}$ at $T_{sc} \simeq 1.6\,\mathrm{K}$ is 170 kOe/K for $H \parallel [001]$, whereas it is 145 kOe for $H \parallel [110]$. The striking difference between $H \parallel [001]$ and [110] is not only the value of the upper critical field at 0 K but also its temperature dependence. The upper critical field $H_{c2}(T)$ for $H \parallel [110]$ is suppressed by the spin polarization based on the Zeeman splitting, namely Pauli paramagnetic suppression with decreasing temperature. Indeed, the orbital limiting field $H_{orb}(= -0.73(dH_{c2}/dT)T_{sc})$ estimated from the slope of H_{c2} at T_{sc} is to be 170 kOe [36, 37] and is much larger than $H_{c2}(0)$=95 kOe, indicating the strong Pauli paramagnetic suppression. On the other hand, the upper critical field $H_{c2}(0) \simeq 450\,\mathrm{kOe}$ for $H \parallel [001]$ is not suppressed by the Pauli paramagnetic limiting. Moreover, $H_{c2}(T)$ exhibits an upward behavior with decreasing temperature, reflecting strong-coupling superconductivity. This is because all the spins of the conduction electrons are perpendicular to the magnetic field direction for $H \parallel [001]$, as shown in Fig. 2.14(c), and therefore the spin susceptibility for $H \parallel [001]$ does not change below T_{sc}.

Thus, we conclude that in $CeIrSi_3$, due to the combined effects of the strong coupling superconductivity and the spin-orbit interaction working in a system without inversion symmetry, the field-robust superconducting state with the huge $H_{c2}(0) \simeq 450\,\mathrm{kOe}$ is realized despite the low superconducting transition temperature $T_{sc} = 1.6\,\mathrm{K}$. We summarize in Table 2.3 the superconductivity properties for chiral superconductors, which are mainly non-magnetic superconductors.

Table 2.3: Chiral superconductors

crystal system	material	point group	space group	transition temperature (K)	upper critical field H_{c2} (T)
Monoclinic	BiPd [40]	2 (C_2)	$P2_1$	3.8	0.8
Trigonal	$NbRh_2B_2$ [41]	3 (C_3)	$P3_1$	7.6	18.0
	$TaRh_2B_2$ [41]	3 (C_3)	$P3_1$	5.8	11.7
Hexagonal	$TaSi_2$ [42]	622 (D_{6h})	$P6_222$	0.35	0.003
Cubic	PdBiSe [43]	23 (T)	$P2_13$	1.5	
	BeAu [44]	23 (T)	$P2_13$	3.3	0.034
	LaRhSi [45]	23 (T)	$P2_13$	4.35	
	LaIrSi [45]	23 (T)	$P2_13$	2.3	
	Mo_3Al_2C [46, 47, 48]	432 (O)	$P4_132$	9.2	15.1
	Cr_2Re_3B [49]	432 (O)	$P4_132$	9.2	10.0
	Li_2Pd_3B [50, 51, 52, 53]	432 (O)	$P4_332$	7.2	4.5
	Li_2Pt_3B [50, 51, 52, 53]	432 (O)	$P4_332$	2.6	1.9
	W_3Al_2C[54, 55]	432 (O)	$P4_132$	7.6	13.1
	Mo_3Rh_2N [56]	432 (O)	$P4_132$	4.6	7.32
	$Mo_7Re_{13}B$ [57]	432 (O)	$P4_132$	8.3	15.4
	$Mo_7Re_{13}C$ [57]	432 (O)	$P4_132$	8.1	14.8
	$W_7Re_{13}B$ [58]	432 (O)	$P4_132$	7.1	11.4
	$W_7Re_{13}C$ [58]	432 (O)	$P4_132$	7.3	12.6

magnetic skyrmion in EuPtSi and MnSi

Since EuPtSi has a characteristic chiral crystal structure, it has been studied as a frustrated magnet from the theoretical viewpoints [59, 60, 61]. The magnetic long-range ordering in geometrically frustrated magnets with the lattices such as triangular, honeycomb, Kagomé, and pyrochlore lattices is known to be suppressed to unusually low temperatures, and interesting phenomena often appear at low temperatures. EuPtSi is a new type of geometrically frustrated magnetic system, in which Eu atoms form a corner-sharing equilateral triangular lattice named trillium lattice, as shown in

Fig. 2.19(c). A macroscopically degenerated trillium spin-ice state was suggested from the local ferromagnetic Ising model for Eu spins on the trillium lattice [61], and a first-order magnetic transition was predicted on the basis of the Heisenberg model on the trillium lattice [59, 60].

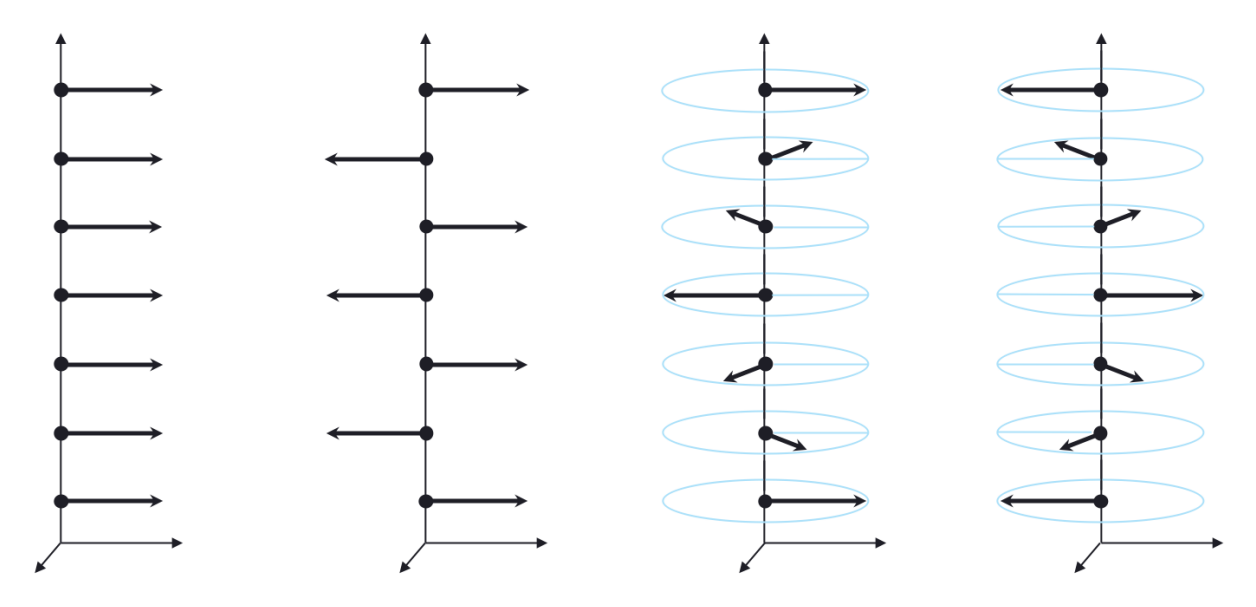

Figure 2.23: Simplified (a) ferromagnetic, (b) antiferromagnetic, and (c) helical magnetic structures.

EuPtSi shows an antiferromagnetic order which is mediated by the RKKY interaction, as in the usual divalent Eu compounds. We show in Fig. 2.23 the simplified ferromagnetic, antiferromagnetic, and helical magnetic structures, where the lattice parameter along the z-direction is c. Here, it was assumed that the magnetic moments in the xy-plane (c-plane) are arranged ferromagnetically. Figure 2.23(a) shows the ferromagnetic structure with the magnetic easy-axis along the y-direction. The antiferromagnetic propagation vector for the antiferromagnetic structure in Fig. 2.23(b) is $\boldsymbol{q} = (0, 0, 1)$, while the magnetic propagation vector for the helical structure in Fig. 2.23(c) is $\boldsymbol{q} = (0, 0, 1/6)$.

The ground state magnetic structure of EuPtSi at $H = 0$ kOe was found to be helical. When the magnetic field is applied for the $\langle 111 \rangle$ direction, a skyrmion lattice phase is induced in a limited magnetic field and temperature region. The skyrmion can be expressed by a superposition of three helical states or a triple-$\boldsymbol{q}$ order which satisfies the equation of $\boldsymbol{q}_1 + \boldsymbol{q}_2 + \boldsymbol{q}_3 = 0$. The ground state helical magnetic structure is

closely related to the crystal structure. As mentioned above, since the crystal structure of EuPtSi lacks the inversion symmetry, canting of spins could be realized owing to an additional magnetic exchange term; the Dzyaloshinskii–Moriya (DM) interaction $H_{\mathrm{DM}} = \boldsymbol{D} \cdot \left(\boldsymbol{S}_i \times \boldsymbol{S}_j\right)$, where $\boldsymbol{D}$ is related to both the exchange interaction and the spin-orbit interaction [7, 8]. When two spins $\boldsymbol{S}_1$ and $\boldsymbol{S}_2$ are situated at the sites without inversion symmetry, a magnetic exchange term $\boldsymbol{S}_1 \times \boldsymbol{S}_2$ leads to complex magnetic states such as the helical magnetic structure [7, 8, 62, 63, 64]. We show later clarified the existence of the magnetic skyrmion phase in the antiferromagnetic phase of EuPtSi, which is highly different from the well-known skyrmion phase of MnSi.

The magnetization at $T = 2$ K for $H \parallel [111]$ increases almost linearly as the magnetic field is increased, exhibiting two small anomalies at $H_{\mathrm{A1}} = 9.2$ kOe and $H_{\mathrm{A2}} = 13.8$ kOe, and saturates at $H_{\mathrm{c}} = 26.6$ kOe, as shown in Fig. 2.24(a). The corresponding differential magnetization dM/dH has two peaks at H_{A1} and H_{A2}. In this narrow field region between H_{A1} and H_{A2}, the ac susceptibility, χ_{ac}, and the Hall resistivity, $-\rho_{\mathrm{H}}$, exhibit characteristic dips, as shown in Figs. 2.24(b) and 2.24(c), respectively. The magnetic field versus temperature H–T phase diagram for $H \parallel [111]$ is shown in Fig. 2.24(d). The present magnetic-field-induced phase between H_{A1} and H_{A2} was found to be closed in the H–T plane, ranging from $T = 0.5$ to 3.6 K. The A-phase for MnSi, however, only exists as a small phase pocket in the vicinity of the magnetic ordering temperature of 29.5 K [65].

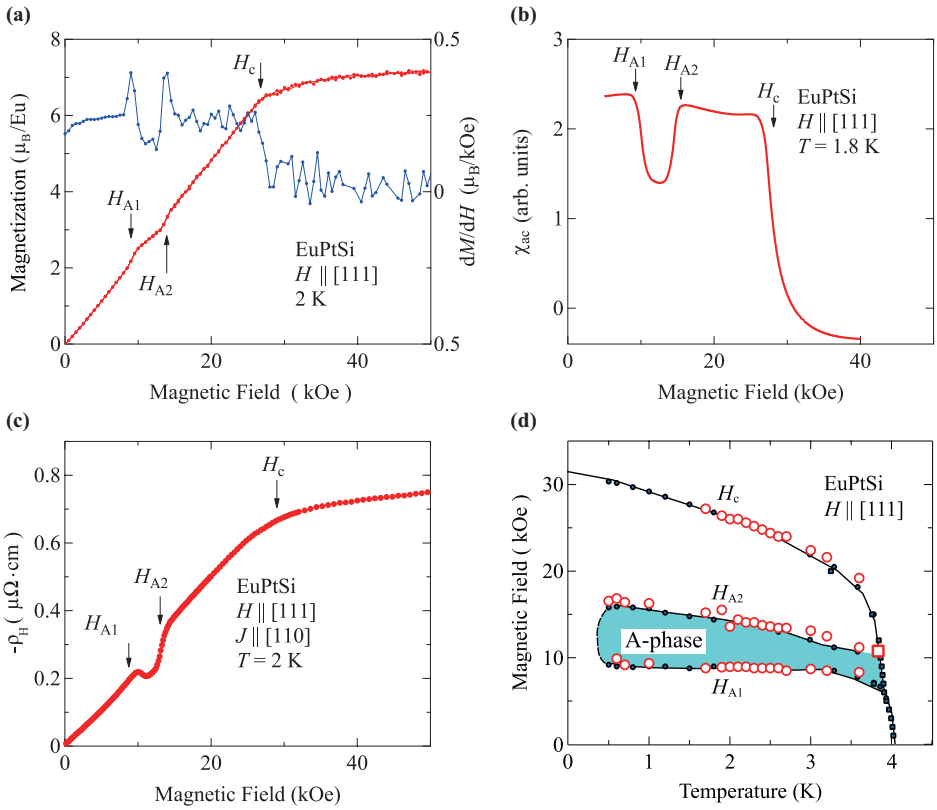

Figure 2.24: (a) Magnetization curve for H ||[111]and field derivative of magnetization dM/dH, (b) ac susceptibility $\chi_{\rm ac}$, (c) Hall resistivity $-\rho_{\rm H}$, and (d) magnetic phase diagram for EuPtSi, cited from [28].

The ground state magnetic structure below $T_{\rm N}$ in EuPtSi was revealed as a helical structure with the propagation vector $\boldsymbol{q} = (0.2, 0.3, 0)$ at zero magnetic field by the recent neutron and resonant X-ray scattering experiments [6, 66]. In addition, the A-phase of EuPtSi for $H \parallel [111]$ was clarified as the skyrmion lattice phase with the triple-$\boldsymbol{q}$ order of $\boldsymbol{q}_1 = (-0.09, -0.2, 0.29)$, $\boldsymbol{q}_2 = (-0.2, 0.29, -0.09)$, and $\boldsymbol{q}_3 = (0.29, -0.09, -0.2)$. These magnetic wave vectors are three-fold symmetric around the [111] direction and perpendicular to $H \parallel [111]$.

We consider the large additional (topological) Hall resistivity $\Delta\rho_{\rm H} = 0.12\,\mu\Omega$·cm at $T \simeq 1$ K for EuPtSi, which is compared with $\Delta\rho_{\rm H} = 0.005\ \mu\Omega$·cm for MnSi [65]. It is speculated that the large additional Hall resistivity for EuPtSi might be due to the small size of the skyrmion, 18 Å. This value is 10 times as small as that of 180 Å in MnSi, as shown schematically in Fig. 2.25. The size of the skyrmion $\xi = 18$ Å for EuPtSi was estimated using relations $\xi = 2\pi/|\boldsymbol{q}|$ and $|\boldsymbol{q}| = 0.36(2\pi/a)$ with the magnetic wave vector $\boldsymbol{q} = (0.2,0.3,0)$ and the lattice constant $a = 6.4336$ Å. The present $|\boldsymbol{q}|$ value is quite reasonable for the rare-earth compounds. In these compounds, the magnetic ordering

is mediated by the RKKY interaction, and the Friedel oscillation is strongly damped as the distance between rare-earth atoms is increased. As for the skyrmion of 3*d*-electron systems, the helical propagation vector is small in magnitude, $\boldsymbol{q} = (0.017, 0.017, 0.017)$ for MnSi. The size of the skyrmion is estimated to be 180 Å for $H \parallel [111]$ [63, 67, 4]. By a simple calculation, the number of skyrmions in the unit area in EuPtSi is 100 times as large as those in MnSi. Large numbers of skyrmions might induce a large emergent magnetic field in EuPtSi, leading to a large $\Delta\rho_{\mathrm{H}}$. It should be mentioned that MnSi shows spin-fluctuating magnetism owing to itinerant 3*d*-electrons, which is highly different from the localized magnetism of 4*f*-electrons based on the RKKY interaction for EuPtSi.

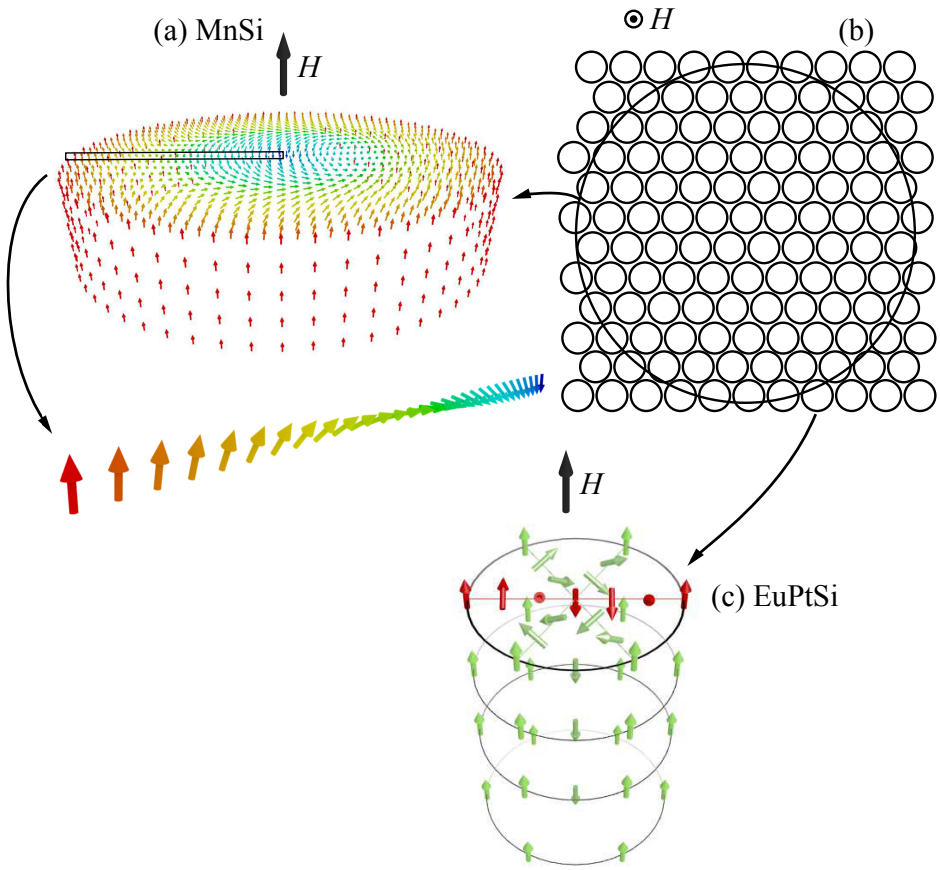

Figure 2.25: Schematic representations of a skyrmion for (a) MnSi and (c) EuPtSi. The large circle in (b) shows the size of the skyrmion for MnSi (180 Å), while the small circles indicate the size of the skyrmion of EuPtSi (18 Å) in the A-phase for $H \parallel [111]$, cited from ref. [28].

chiral soliton lattice

There exist two kinds of magnets with helical magnetic structures. One is a Yoshimori-type or symmetric helimagnet, as shown in Fig. 2.26. In this case, the nearest exchange interaction J_1 is ferromagnetic ($J_1 > 0$), while the next nearest exchenge interaction J_2 is antiferromagnetic ($J_2 < 0$). The pitch angle in this helical magnetic structure is defined as $\tan^{-1}(-J_1/2J_2)$. When the magnetic field is applied for the helical axis, the magnetic structure is changed from "helical" to "conical" and finally become a field-induced ferromagnetic state. On the other hand, the field is perpendicular to the helical axis, the magnetization indicates a metamagnetic transition at a certain field and the magnetic structures changes into a fan structure, finally changing into a field-induced ferromagnetic state, as shown in Fig. 2.26.

If the crystal structure is chiral, the other type of a helimagnet might be realized due to the Dzyaloshinskii-Moriya (known as DM) interaction, where the antisymmetric exchange interaction is the source of the chiral helimagnet, as shown in Fig. 2.26. In this case, the pitch angle is defined as $\tan^{-1}(D/J)$, where the DM interaction is defined as $\boldsymbol{D} \cdot \boldsymbol{S}_i \times \boldsymbol{S}_j$, $\boldsymbol{D}$ is directed along the helical axis, and the exchange interaction J between $\boldsymbol{S}_i$ and $\boldsymbol{S}_j$ is ferromagnetic ($J > 0$). The pitch angle is small because $\boldsymbol{D}$ is by one order smaller than J, revealing a long period of $L = 480$ Å in $CrNb_3S_6$, for example. When the magnetic field is applied perpendicularly to the herical axis, a chiral soliton is realized as shown schematically in Figs. 2.27(a) and 2.27(b). The period of the soliton $L(H)$ becomes large as a function of the magnetic field H.

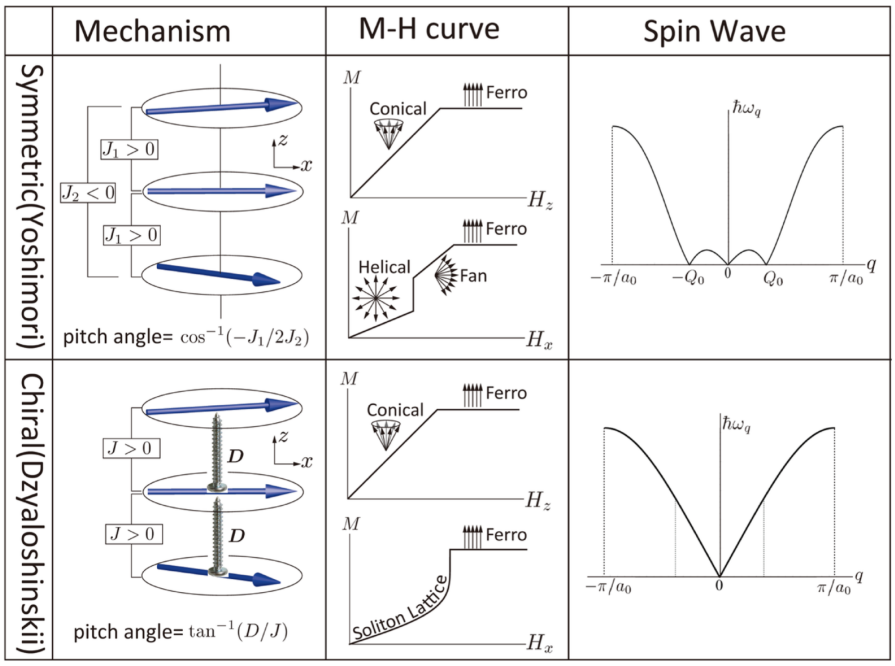

Figure 2.26: Basic properties of symmetric and chiral helimagnets, cited from ref. [68].

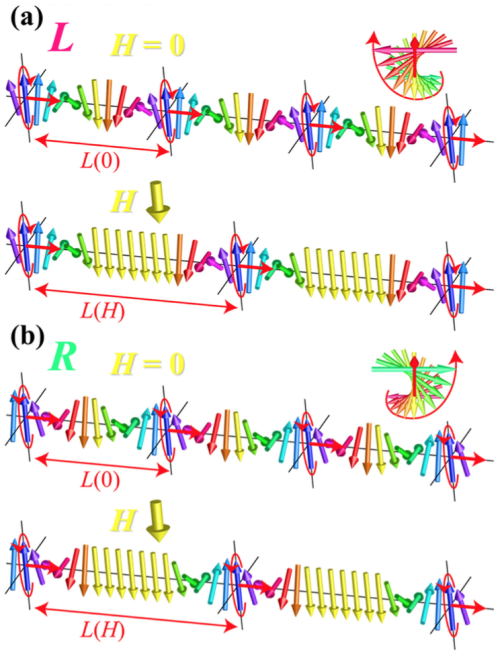

Figure 2.27: Left- and right-handed helimagnetic structures and soliton lattices, cited from ref. [68].

In 1983, Miyadai *et al.* measured the magnetization of $Cr_{1/3}NbS_2$ and observed

the characteristic magnetization curve for $H \perp c$-axis, as shown in Fig. 2.29 [69]. $Cr_{1/3}NbS_2$ was a layered compound, where the mother crystal of NbS_2 with the hexagonal structure is metallic, and Cr is intercalated among the van der Waals gap of S and S layers. At present, $Ce_{1/3}NbS_2$ is altered in the unit cell of the crystal structure, as shown in Fig. 2.28 [70]. The corresponding compound is $CrNb_3S_6$, where a localized spin of $S = 3/2$ in Cr^{3+}, forms a helimagnet ($T_c = 127\ K$). A saturation field H_s at 4.2 K is H_s =20 kOe or 2 T fot $H \parallel c$-axis, whereas H_c is extremely small for $H \perp c$-axis, H_c = 1.4 kOe = 0.14 T. This is mainly based on the small value of J and D, although each Cr layer is ferromagnetic and this exchange interaction is very strong.

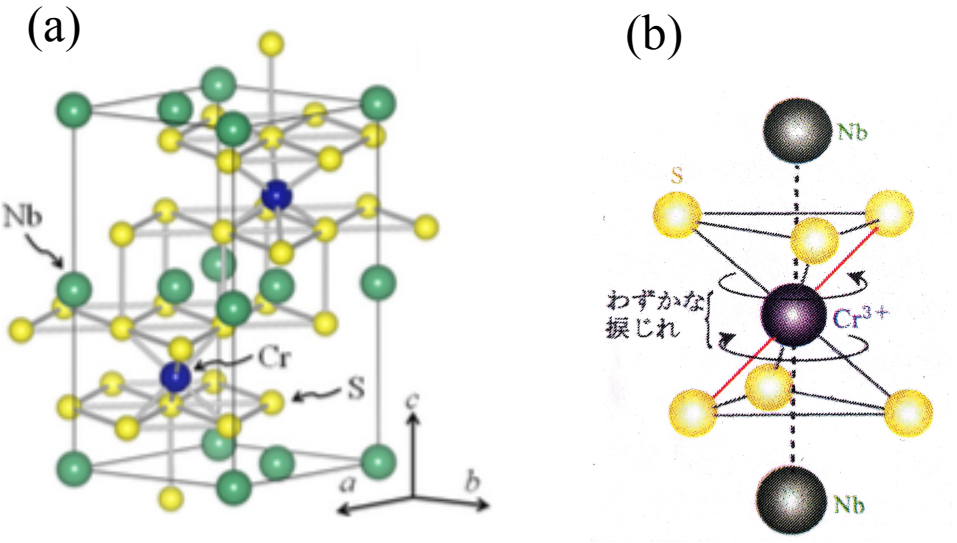

Figure 2.28: (a) Crystal structure of $CrNb_3S_6$ and (b) atomic configuration around Cr, cited from ref. [70].

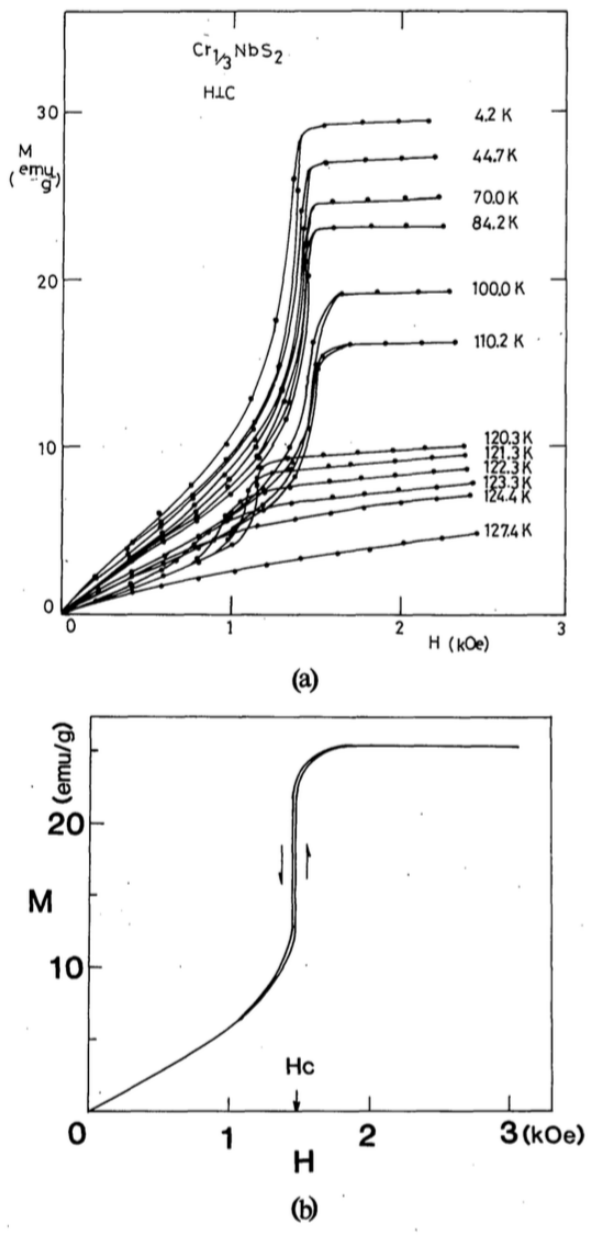

Figure 2.29: Magnetization curves in c-plane ($H \perp c$) at various temperatures. (b) A typical example of the metamagnetic behavior observed at 77 K with a Foner-type magnetometer, cited from ref. [69].

The chiral soliton lattice was experimentally found in 2012 for this compound [71]. Figure 2.30 indicates Lorentz Fresnel micrographs in $CrNb_3S_6$ at 110 K under 0 Oe and 2.08 kOe. $L(H)$ increases from 48 nm at 0 Oe to 92 nm at 2.08 kOe. Note that H_s value is enhanced when the size of the crystal becomes small. Namely, a small size of the sample is used in this experiment.

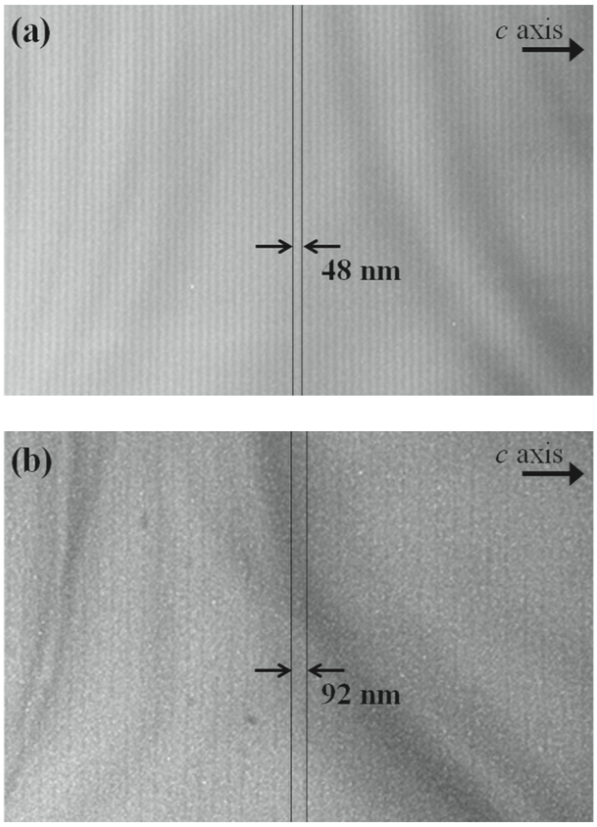

Figure 2.30: Lorents Fresnel micrographic of the chiral helimagnet and chiral soliton lattice in $CrNb_3S_6$ at 110 K in (a) 0 Oe and (b) 2.08 kOe, cited from ref. [68].

Magnetochiral anisotropy

Magnetochiral anisotropy is a phenomenon in which the physical properties of chiral compounds differ between left-handed and right-handed crystals on the basis of the chirality of the crystal under the magnetic field. Optical magnetochiral anisotropy, which exhibits a different response in the absorption and refraction of unpolarized light propagating parallel or antiparallel to the magnetic field in a chiral medium, was predicted theoretically in the 1960s [72].

This magnetochiral anisotropy has been studied not only in optical physics but also in a wide range of fields such as sound propagation [73, 74, 75, 76, 77], photochemistry [78, 79], electrochemistry [80]. In the case of intermetallic compounds, electrical magnetochiral anisotropy, in which the electrical resistivity in magnetic fields is different between left-handed and right-handed crystals, has been studied extensively. One of the origins of electrical magnetochiral anisotropy with chiral compounds is reflected

in magnetoresistance, which is induced by the helical motion of conduction electrons. In a chiral structure, atoms are arranged in a helical configuration; therefore, the conduction electron, as it were, moves in a spiral motion through the crystal. By analogy with a solenoid, a spontaneous magnetic field $\boldsymbol{B}_{\mathrm{int}}$ is generated by the conduction electrons in a spiral motion at zero external magnetic field. When the external magnetic field $\boldsymbol{B}_{\mathrm{ext}}$ is applied to the herical crystal, the magnetic field $\boldsymbol{B}$ becomes $\boldsymbol{B} = \boldsymbol{B}_{\mathrm{int}} + \boldsymbol{B}_{\mathrm{ext}}$ and contributes to the magnetoresistance, as shown in Fig. 2.31. The direction of the spontaneous magnetic field $\boldsymbol{B}_{\mathrm{int}}$ changes with the direction of the atomic helix; namely, left-handed crystals generate magnetic fields with a different orientation compared to the right-handed crystals. This is because the electrical resistivity is different between the right-handed and left-handed systems.

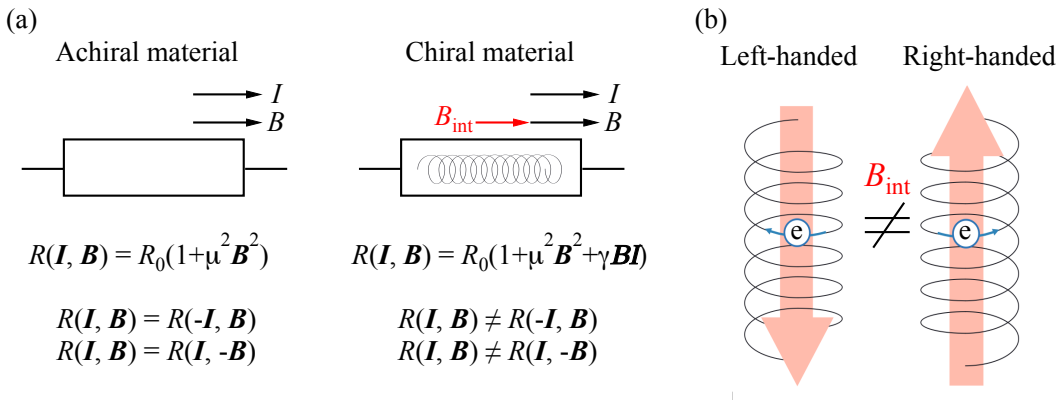

Figure 2.31: (a) Illustration of electrical resistances of achiral and chiral conductors and (b) illustration of the internal magnetic fields which are produced from the helical motion of the conduction electrons in left- and right-handed crystals.

Regarding the theory of electrical magnetochiral anisotropy, Rikken generalized Onsergar's reciprocal theorem into the nonlinear regime, and obtained the following equation;

$$R^{D/L} = R_0 \left[1 + \mu^2 B^2 + \gamma^{D/L} B \cdot I\right], \tag{2.36}$$

where μ is the mobility of the conduction electron, and γ^{D} and γ^{L} are the magnetochiral coefficient corresponding to the right-handed and left-handed crystals, respectively, satisfying $\gamma^{\mathrm{D}} = -\gamma^{\mathrm{L}}$. In eq. (2.36), the first term represents the electrical resistivity at zero field, the second term represents the normal magnetoresistance, and the third term represents the magnetoresistance due to the electrical magnetochiral anisotropy. The first report of electrical magnetochiral anisotropy was conducted by Rikken using

single crystals of twisted Bi [81]. The crystal structure of Bi belongs to the space group $R\bar{3}c$ (No.167). Although the crystal structure is an achiral structure, twisting the crystals to right and left rotation gives chirality to the crystals. The field dependence of the electrical magnetochiral anisotropy was studied in Bi helix, namely $\Delta R \equiv R(I,B) - R(-I,B)$ for two samples (L-torsion and D-torsion samples), where correspond to the left-twisted and right-twisted samples, respectively. The L-torsion sample has a positive correlation to the magnetic field, while the D-torsion sample has a negative correlation.

The electrical magnetochiral anisotropy was also observed in Te, a semiconductor with a chiral structure [82]. The angular dependence of the electrical magnetochiral anisotropy was studied in Te. $\Delta R/R = 4V^{2\omega}/V$, or V_{EMChA}, where $V^{2\omega}$ is the second harmonics of the voltage when a an alternating current $I^{\omega} = I_0 \sin\omega t$ is applied to the sample, is expressed as follow;

$$
\begin{aligned}
V_{\mathrm{EMChA}} &= IR_{\mathrm{EMChA}} && (2.37)\\
&= \gamma^{D/L} R_0 B I^2 && (2.38)\\
&= \gamma^{D/L} R_0 B I_0^2 \sin^2\omega t && (2.39)\\
&= \frac{\gamma^{D/L}}{2} R_0 B I_0^2 \left[1 - \sin\left(2\omega t + \frac{\pi}{2}\right)\right]. && (2.40)
\end{aligned}
$$

The last variant of the equation is based on the double angle formula. The magnitudes of V_{EMChA} shows approximately the same value in the right- and left-handed crystals, while the signs of V_{EMChA} are different. Namely, the electrical magnetochiral anisotropy has opposite responses in the right- and left-handed crystals in Te. The temperature dependence of $\Delta R/R$ in Te was studied for the left-handed crystal. The temperature range is approximately from 260 K to 340 K. The $\Delta R/R$ increases with decreasing temperature. Rikken discussed this behavior using the electrical conductivity σ derived from the Boltzmann equation;

$$
\sigma_{ij} = \frac{q^2\tau}{4\pi^3\hbar^2} \int \left(\frac{\partial\varepsilon(\boldsymbol{k})}{\partial k_i}\right)^2 \frac{\partial f}{\partial\varepsilon} d^3\boldsymbol{k}, \tag{2.41}
$$

where f is the distribution function, q is the charge, τ is the scattering lifetime, m^* is the effective mass, and for Maxwell-Boltzmann statistics, $\partial f/\partial\varepsilon = -f/k_bT$. By assuming the splitting of the Fermi surface to be $\Delta\varepsilon = \chi^{D/L}\boldsymbol{k}\cdot\boldsymbol{B}_{\perp}$, the energy dispersion around the H point is expressed as $\varepsilon(\boldsymbol{k}) = \hbar^2\boldsymbol{k}^2/2m^* + \chi^{D/L}\boldsymbol{k}\cdot\boldsymbol{B}_{\perp}$, and then eq. (2.41) is expressed as

where

$$\gamma^{D/L} = m^* \chi^{D/L} / N q \hbar k_b T \tag{2.42}$$

and N is the carrier density. Using the carrier density of Te, the temperature dependence of $\gamma^{D/L}$ is obtained as $T^{-\frac{5}{2}} \exp(E_g / 2k_B T)$, which is in good agreement with the experimental results. Semiconductors and semimetals are extremely small in the m^* of order 0.01 m_0 and then $\gamma^{D/L}$ is enhanced for these materials with high-quality and longer τ values.

The electrical magnetochiral anisotropy requires both inversion and time-reversal symmetry breaking. In a non-magnetic chiral crystal, the inversion symmetry is broken, but the time-reversal symmetry is preserved. Therefore, applying an external magnetic field breaks the time-reversal symmetry in the crystal. On the other hand, ferromagnetic and antiferromagnetic materials break the time-reversal symmetry, and it is expected to show a large electrical magnetochiral anisotropy. MnSi crystallizes in the cubic chiral structure with space group $P2_13$ (No. 198), in which the helical and skyrmion phases exist below $T_c = 35$ K. The electric magnetochiral anisotropy was studied for MnSi, together with the chiral helimagnetic compound $CrNb_3S_6$ [83, 84].

CHAPTER 3

Exprimantal

3.1 Single crystal growth

High-purity samples are essential for physical properties experiments. Physical properties, especially at low temperatures, are often strongly affected by impurities and lattice distortions, which mask essential phenomena. In particular, as described in Chaper 3, the dHvA signal is greatly attenuated by impurity scattering, so that the purity of the single crystal is of utmost importance. In this study, we synthesized single or polycrystalline crystals and succeeded in obtaining high-quality single crystals through trial and error.

Single crystals of α-$RhSn_4$ and α-$IrSn_4$ were synthesized by the flux method. Single crystals of $IrGe_4$ were synthesized by the Czochralski method. Moreover, the polycrystals of $RhGe_4$ were synthesized by the high-pressure method. The crystal growth will be introduced in this section.

Previous report

$IrSn_4$

Three types of crystal structure have been reported: low temperature phase of α-$IrSn_4$, high temperature phase of β-$IrSn_4$, and high pressure phase of $IrSn_4$. α-$IrSn_4$ crystallizes in a trigonal $IrGe_4$-type structure with space group either $P3_121$ (No. 152) or $P3_221$ (No. 154), as shown in Fig. 3.2(a). The first synthesis of α-$IrSn_4$ was reported by Lang [85]. Single crystals of α-$IrSn_4$ were obtained by annealing the transition

metals with tin in the atomic ratio 1 : 10 in evacuated silica tubes at 550 °C for 2 days, followed by 5 days at 300 °C and subsequent quenching in water. The largest dimension of single crystals is approximately 0.5 mm. The residual resistivity ratio RRR is 1.5, indicating a low-purity single crystal. Recently, Omura succeeded in synthesizing high quality of single crystals by the Sn self-flux method [86]. The synthesis method is as follows: Ir powder (99.99% (4N)) and an excessive amount of Sn (5N) at an atomic ratio of Ir : Sn = 1 : 10 were loaded into a quartz tube and sealed under vacuum. The sealed quartz ampoule was heated up to 800 °C, maintained at this temperature for 100 h, cooled down to 200 °C at a rate of 6 °C/h, and furnace cooled down to RT. The RRR value is 628, attesting to the high quality of the crystal. However, the size of the single crystals is approximately 0.3 mm, which is too small to determine the orientation and to detect the dHvA effect.

β-$IrSn_4$ crystallizes in a tetragonal $MoSn_4$-type structure with space group $I4_1/acd$ (No. 141), as shown in Fig. 3.2(b). The first synthesis of β-$IrSn_4$ was reported by Nordmark in 2002 [87]. The synthesis method is as follows: Starting materials were powder of Ir (3N) and Sn (5N) which were mixed in a molar ratio of 1 : 10. The reactants were pressed into pellets and loaded into quartz ampoules, which were sealed under vacuum. The quartz ampoules were heated to 800°C, annealed for 24 h and subsequently quenched in water. In addition, they reported that α-$IrSn_4$ was synthesized at temperatures below 600 °C and β-$IrSn_4$ at temperatures above 700 °C.

HP-$IrSn_4$ crystallize in a tetragonal $PtSn_4$-type structure with space group $Aba2$ (No. 42), as shown in Fig. 3.2(c). The first synthesis was reported by Larchev in 1984 [88]. The synthesis method is as follows; Ir powder (3N) and Sn powder (4N) at a molar ratio of Ir : Sn = 1 : 4 were compressed and heated at temperatures of 900-1100 at pressures above 6.0 GPa for 30 min.

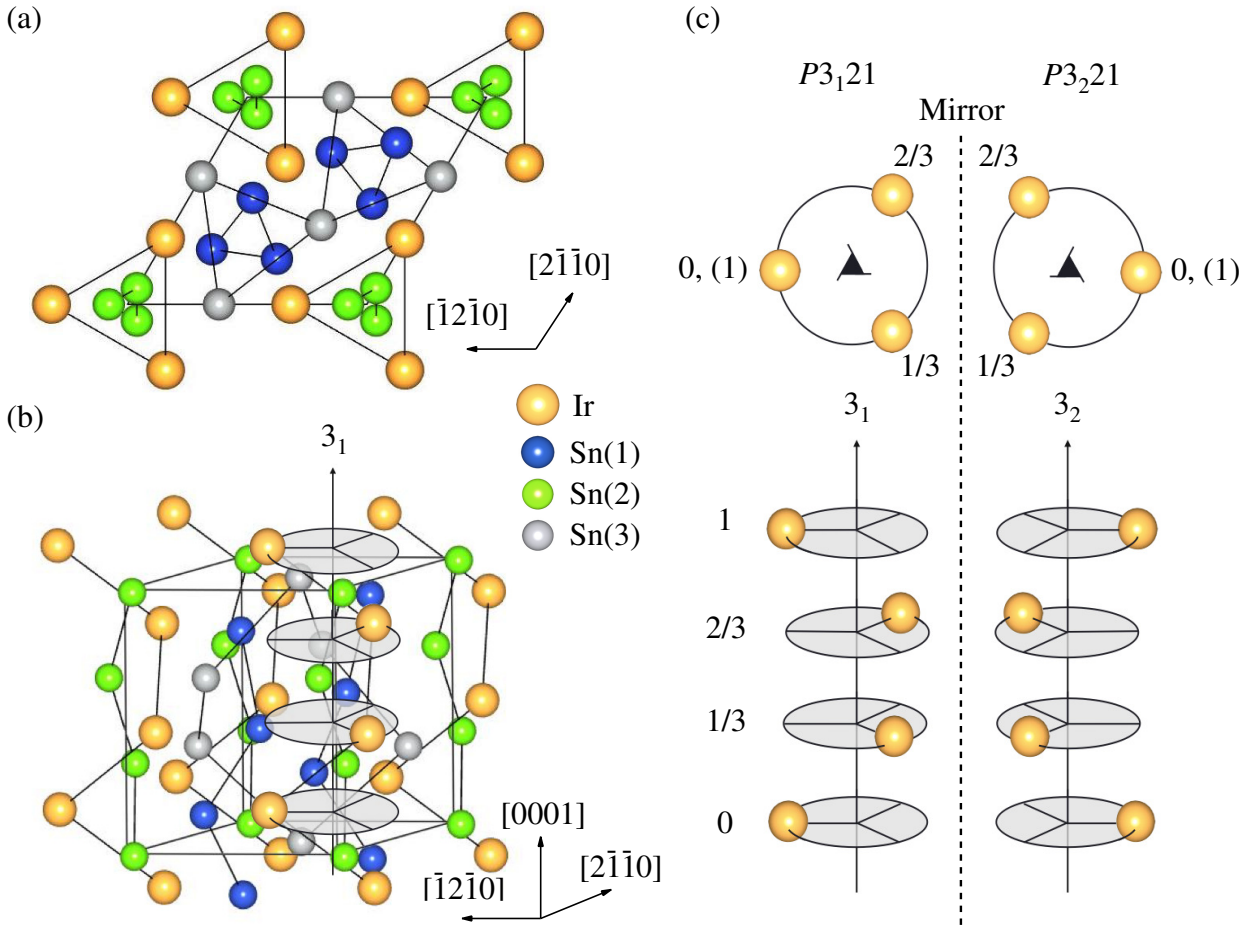

Figure 3.1: Crystal structure of αIrSn$_4$. (a) and (b) correspond to the top view from [0001] and the crystal structure with space group of No. 152, respectively. (c) Left and right figures show the spiral structure of Ir-atoms based on the crystal structure. Upper figures of (c) show the 3-fold screw axis 3$_1$ for $P3_121$ and 3$_2$ for $P3_221$ with graphical symbols.

RhSn$_4$

As for RhSn$_4$, two types of crystal structures have been reported: a low temperature phase of α-RhSn$_4$ and a high temperature phase of β-RhSn$_4$. α-RhSn$_4$ crystalizes in a trigonal IrGe$_4$-type structure same as α-IrSn$_4$, as shown in Fig. 3.2(a). The first synthesis of α-RhSn$_4$ was reported by Lang [85]. Single crystals of α-RhSn$_4$ were obtained by annealing the transition metals with tin in the atomic ratio 1 : 10 in evacuated silica tubes at 550 °C for 2 days, followed by 5 days at 300 °C and subsequent quenching in water. The largest dimension of single crystals is approximately 0.5 mm. The residual resistivity ratio RRR is approximately 10, indicating a low-purity single crystal.

β-$RhSn_4$ crystallizes in the tetragonal $MoSn_4$-type structure same as β-$IrSn_4$, as shown in Fig. 3.2(b). The first synthesis of β-$RhSn_4$ was reported by Xing in 2002 [89]. The synthesis method is as follows; Rh powder (4N) and Sn grains (4N) were mixed in a molar ratio of Rh : Sn = 1 : 20, sealed in an evacuated quartz tube, and then heated up to 1050 °C. Subsequently, the sample was slowly cooled down to 650 °C over 7 days and cooled to RT.

$IrGe_4$

Unlike the case of $IrSn_4$ and $RhSn_4$, only one structure of $IrGe_4$ has been reported so far by Panday in 1969 [90]. The crystal structure is shown in Fig.3.2(a). The detailed synthesis method is not described.

$RhGe_4$

Polycrystal growth of $RhGe_4$ under high pressure was reported by Larchev in 1984 [88]. Rh powder (3N) and Sn powder (4N) at a molar ratio of Rh : Sn = 1 : 4 were compressed and heated at temperatures of 1000-1300 at pressures above 2.5 GPa for 30 min. The superconducting transition was reported in Ref. [88]. The superconducting transition temperature is T_{sc} = 2.5 K determined by zero resistivity, described only by sentence without any figures. Crystal structures for TrX_4 are summarized in Table. 3.1

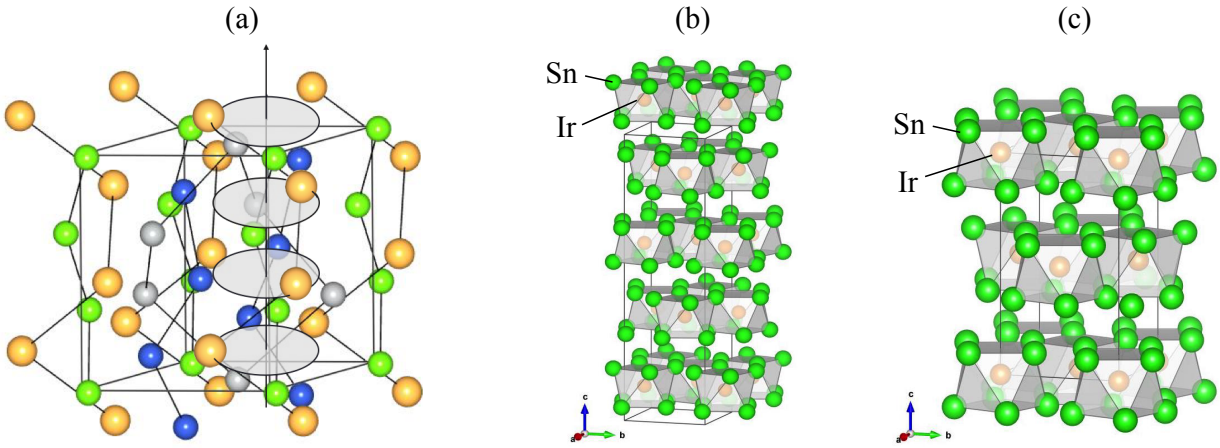

Figure 3.2: Crystal structure of (a) $IrGe_4$-type structure, (b) $MoSn_4$-type structure, and (c) $PtSn_4$-type structure.

Table 3.1: Crystal structures for TrX_4

	$IrGe_4$-type structure $P3_121$ (No. 152) or $P3_221$ (No. 154)	$MoSn_4$-type structure $I4_1acd$ (No. 41)	$PtSn_4$-type structure $Aba2$ (No. 68)
$IrSn_4$	α-$IrSn_4$ [85] (low temperature phase)	β-$IrSn_4$ [87] (high temperature phase)	HP-$IrSn_4$ [88] (high pressure phase 6.0 GPa)
$RhSn_4$	α-$RhSn_4$ [85] (low temperature phase)	β-$RhSn_4$ [89] (high temperature phase)	
$IrGe_4$	$IrGe_4$ [90]		
$RhGe_4$	$RhGe_4$ [88] (high pressure phase 5.0 GPa)		

Phase diagram

Phase diagram is a graphical representation of the physical states of a substance under different conditions of temperature, composition, and pressure. A typical phase diagram of a binary alloy system consists of temperature along the y-axis and composition along the x-axis under ambient pressure. A phase diagram is essentially important for material syntheses.

Figures 3.3(a) and (b)3.3 show phase diagrams of Rh-Sn and Rh-Ge, respectively [91]. The red arrows in the figure indicate where the composition ratios of Rh to Sn and Rh to Ge are 1 : 4. The purple area at the top of the figure indicates the liquid phase, while the lines in the white area indicate the solid phase. The Rh-Sn binary phase diagram shows

that $RhSn_4$ is an incongruent melting, indicating that $RhSn_4$ cannot be synthesized with a composition of Rh : Sn = 1 : 4. Two types of $RhSn_4$ have been reported: the low temperature phase of α-$RhSn_4$ which crystallizes in the $IrGe_4$-type structure with space group of $P3_121$ (No. 152) and the high temperature phase of β-$RhSn_4$ which crystallizes in the β-$IrSn_4$-type structure with space group of $I4_1/acd$ (No. 140). Note that their phase boundaries have not been shown in Fig. 3.3(a). As for $RhGe_4$, the Rh-Ge binary phase diagram shows that $RhGe_4$ does not exist under ambient pressure. For Ir-Sn and Ir-Ge binary systems, no phase diagrams have been reported.

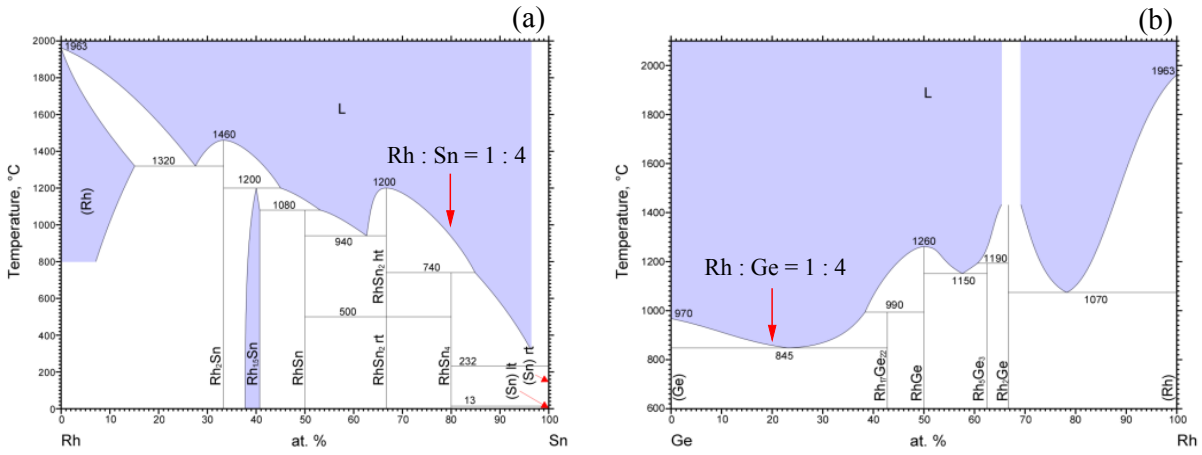

Figure 3.3: Phase diagrams of (a) Rh-Sn and (b) Rh-Ge, cited from ref. [91].

Thermal Gravity-Differential Thermal Analyses

The phase diagram is essential to synthesize the high quality of single crystals. In the case of $RhSn_4$, the boundary between the low-temperature phase α-$RhSn_4$ and high-temperature phase β-$RnSn_4$ has not been reported. As for Ir-Sn and Ir-Ge binary systems, there have been no reports for a phase diagram. To investigate the binary phase diagrams, we carried out thermal gravity-differential thermal analyses (TG-DTA). TG measurement is a technique to measure the weight change of a sample when it is heated and cooled at a constant rate or held at a constant temperature. DTA is an analysis method that measures the temperature difference between a sample and a thermally inert reference while heating and cooling them at a constant rate. When the temperature difference is plotted as a function of temperature (DTA curve), the temperature difference shows a peak structure at an endothermic or exothermic phase transition such as

crystallization or melting. Figures 3.4(a) and 3.4(b) show the DTA curves when a sample melts and crystallizes, respectively, together with the TG curves. Since melting is an endothermic reaction, the DTA curve has a minimum value. The melting temperature T_m is defined by the temperature at which the DTA curve begins to change. On the other hand, since crystallization is an exothermic reaction, the DTA curve has a maximum value, and the coagulation temperature T_c is defined by the temperature at which the DTA curve begins to change. The TG curve is constant when the sample melts or crystallizes.

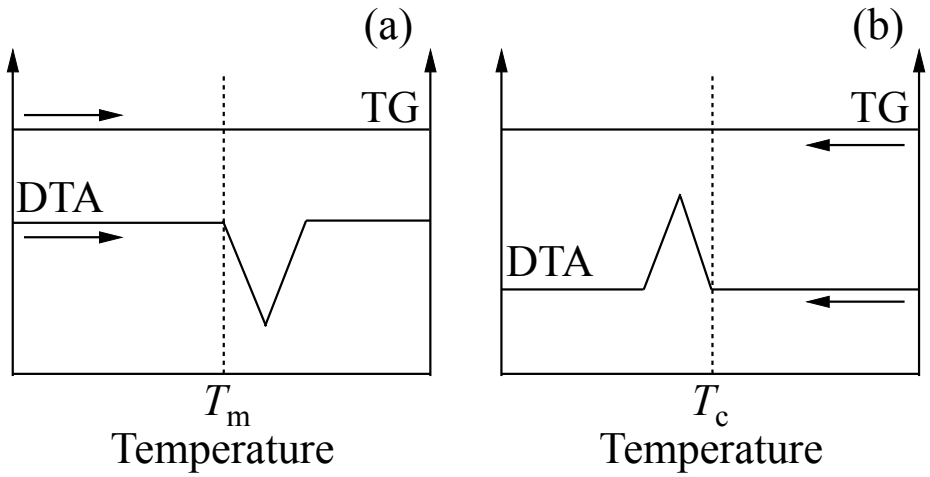

Figure 3.4: Schematic examples of DTA curves for (a) melting (b) crystallizing of samples, together with TG curves. T_m and T_c represent the melting temperature and coagulation temperature, respectively. T_m is defined with temperature increasing measurement and T_c is defined with temperature decreasing measurement.

TG-DTA was measured using a STA 2500 Regulus (NETZSCH), as shown in Fig. 3.5(a). Figure 3.5(b) shows a photograph of the balance which measures the weight of the sample. The sample and reference are put in an almina cup and placed on the balance. A thermocouple is placed under the balance to measure the temperature of the sample and the reference. Figure 3.5(c) shows the almina cup and Pt reference. The sample is single crystals of powdered α-$IrSn_4$ and α-$RhSn_4$. TG-DTA measurements were performed by increasing the temperature from room temperature to 900 (1200) °C at 10 °C/min, keeping for 10 min under 900 (1200) ∘C, then decreasing to room temperature at 10 °C/min for α-$RhSn_4$ (α-$IrSn_4$).

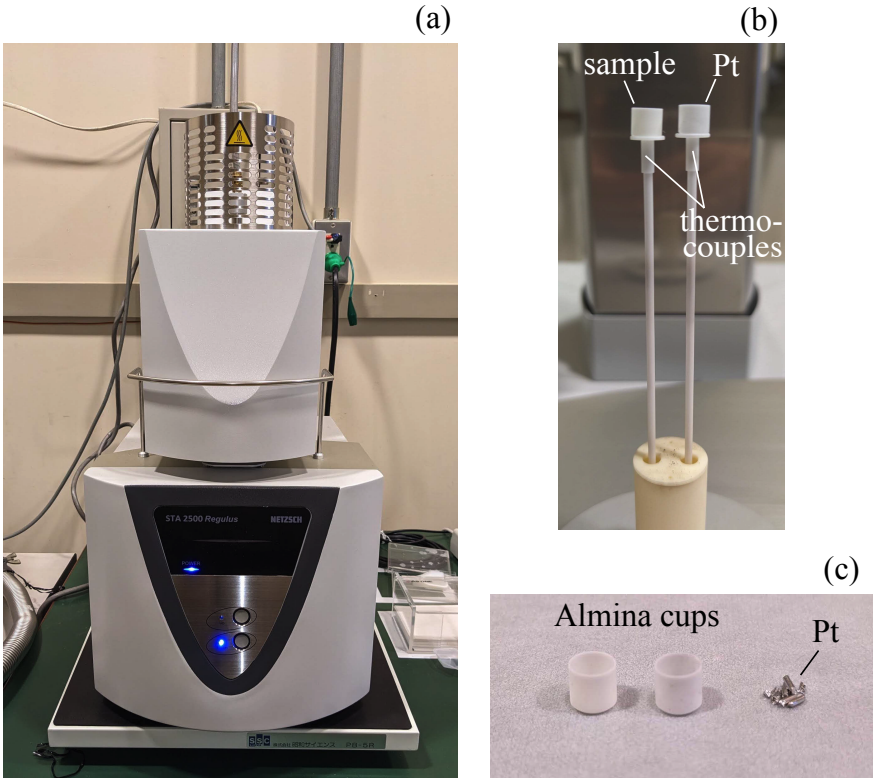

Figure 3.5: Pictures of (a) TG-DTA apparatus of STA 2500 Regulus (NETZSCH), (b) the balance for TG, and (c) almina cups and Pt references.

Figure 3.6(a) shows the temperature dependence of TG-DTA measurement for α-$RhSn_4$. The left axis represents the DTA, and the right axis represents the TG. In a temperature-increasing measurement, there are two minimums corresponding to the endothermal reaction. The temperatures at which the DTA curve begins to change are 450 °C and 500 °C. 450° might correspond to the boundary between α-$RhSn_4$ and β-$RhSn_4$. 500 °C is also written in the reported phase diagram. The result of temperature increasing measurement is different from that of decreasing measurement, indicating that β-$RhSn_4$ is an incongruent melting. Based on the reported phase diagram of Rh-Sn binary system and the present TG-DTA results, the phase diagram of Rh-Sn binary system can be deduced, as shown in Fig. 3.6(c). Figure 3.6(b) shows the temperature dependence of TG-DTA measurement for α-$IrSn_4$. In the temperature-increasing measurement, there are two minima corresponding to the endothermal reaction at 610 °C and 770 °C. 660 °C might correspond to the boundary between α-$IrSn_4$ and β-$IrSn_4$. With reference to the phase diagram of Rh-Sn binary system, the phase diagram of Ir-Sn binary system can be deduced, as shown in Fig. 3.6(c).

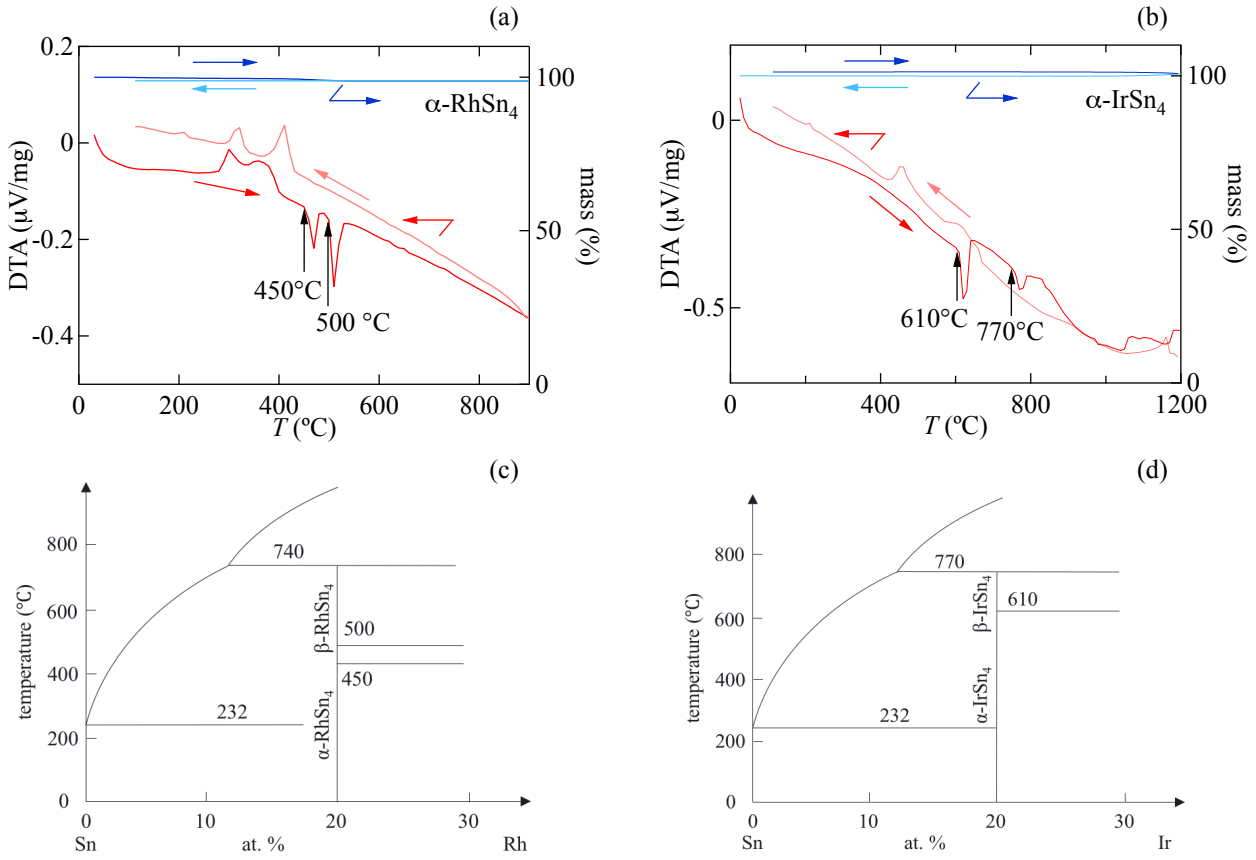

Figure 3.6: Temperature dependences of DTA and TG for (a) α-$RhSn_4$ and (b) α-$IrSn_4$, and deduced phase diagrams for (c) Rh-Sn binary systems and (d) Ir-Sn binary systems.

Flux method: α-$RhSn_4$ and α-$IrSn_4$

The flux method is a kind of single crystal growth method, which corresponds to a slow-cooling process of the premelted components, taken in non-stoichiometric amounts [92]. The advantages of this technique are shown below:

1. Single crystals can be grown often well below their melting points, and this often produces single crystals with fewer defects and much less thermal strain.

2. Flux minerals offer a clean environment for growth since the flux getters impurities which do not subsequently appear in the crystal.

3. There are no stoichiometric problems caused, for instance, by oxidation or evaporation of one of the components. Single crystal stoichiometry ”controls” itself.

4. This technique can be applied to the compounds with high evaporation pressure since the crucible is sealed in the ampoule and the flux prevents evaporation.

5. No special technique is required during the crystal growth, and it can be done with a simple and inexpensive equipment. This is a season why the flux method is sometimes called "poor man's" technique.

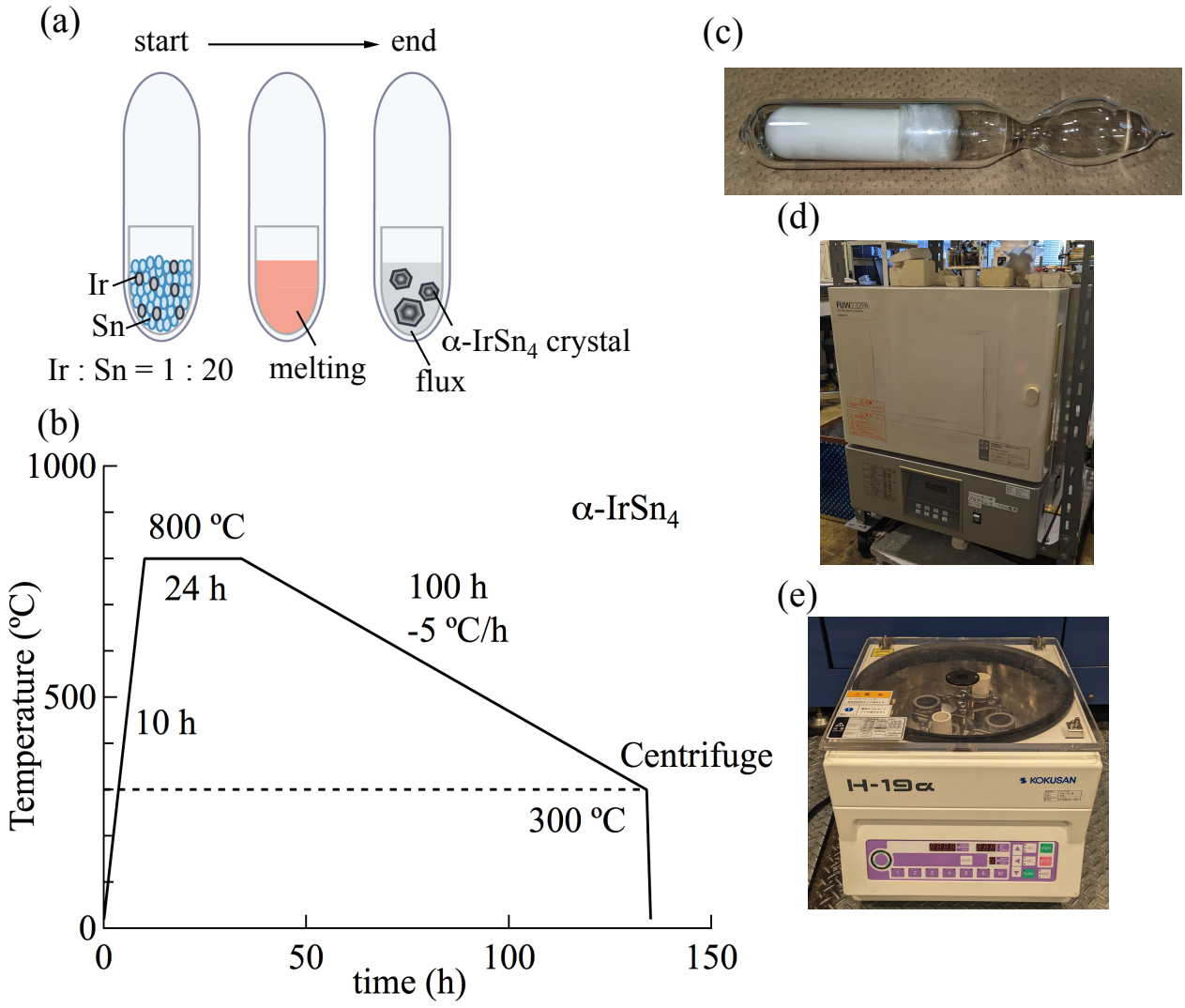

Figure 3.7: (a) Schematic figure of flux methods and (b) the synthesis condition for α-$IrSn_4$. Pictures of (c) a prepared quartz tube for crystal growth, (d) a box furnace of FUW232PA (ADVANTEC), and (e) a centrifuge of H-19α (KOKUSAN).

There are, to be sure, a number of disadvantages to the technique. The first and

foremost is that it is no always an applicable method: an appropriate metal flux from which the desired compound will crystallize may not be found. In addition, difficulties are encountered with some flux choices, when the flux enters the crystal as an impurity, Excessive nucleation causes small crystals, which takes place either due to a too fast cooling rate, or supercooling of the melt by subsequent multiple nucleations and fast growth of large but imperfect crystals usually containing inclusions. The contamination from the crucible cannot be ignored, when reactions with materials occur at high temperatures. Finally, the ability to separate crystals from the flux at the end of growth needs special considerations.

Single crystals of α-$RhSn_4$ and α-$IrSn_4$ were grown by the Sn-self flux method. Starting materials of 4N (99.99 % pure)-Ir powder and 5N-Sn with the composition of Ir : Sn = 1 : 10 were inserted in an alumina crucible, which was sealed in a quartz tube under vacuum (less than 1×10^{-5} torr), as shown in Fig. 3.7(c). The sealed quartz tube was heated to 800 °C, maintained at this temperature for 100 h, cooled slowly to 200 °C at a rate of −6 °C/h, and cooled rapidly to room temperature, as in our previous study [86]. The Sn-flux was removed by spinning the ampoule in a centrifuge at 300 °C. The synthesis condition is shown in Fig. 3.7(b). The excess Sn-flux on the sample was further removed by dissolving the sample into diluted HCl.

We also grew single crystals of α-$IrSn_4$ by the Sn-flux method with a temperature gradient in a horizontal two-zone electric furnace. This modified flux method was reported to be useful for high-quality single crystal growth [93]. Ir and Sn materials with the composition of Ir : Sn = 1 : 15 were inserted in a 15 cm-long quartz tube and sealed under vacuum, which was heated to 675 °C at zone 1 (starting materials zone) and 600 °C at zone 2 (single crystals zone), maintained at these temperatures for 168 h, and cooled to 325 °C and 250 °C, respectively, with a rate of −0.5°C/h. The obtained single crystals are later shown in the inset of Fig. 3.14(a). In the case of $RhGe_4$ and $IrGe_4$, single crystals were not synthesized using the Sn-, Pb-, and Bi-flux methods.

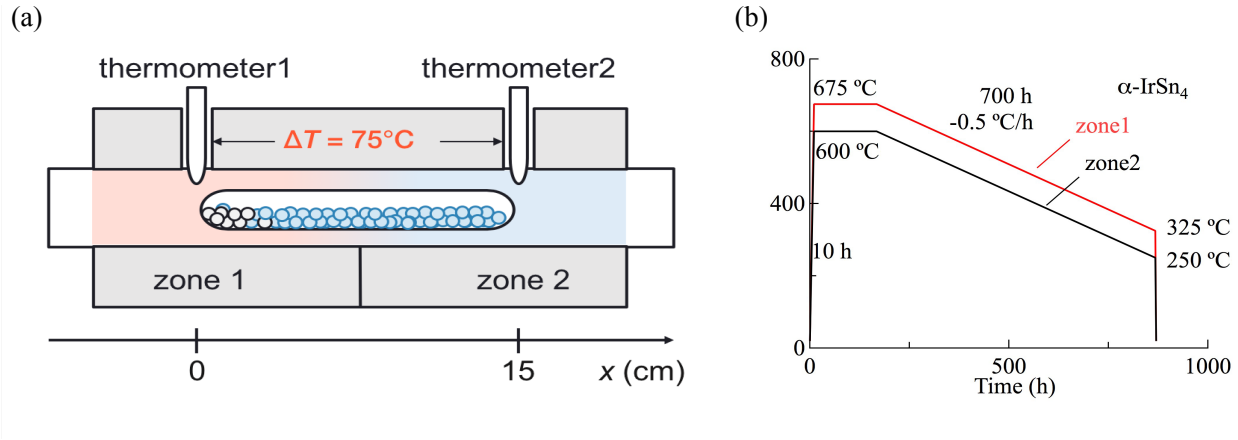

Figure 3.8: (a) Hirizontal two-zone furnace and (b) the synthesis condition for α-IrSN$_4$.

Czochralski method: IrGe$_4$

The Czochralski method is a crystal growth technique that starts with the insertion of a seed crystal or tungsten rod into melting materials in a crucible, pulling the seed upwards to obtain a single crystal. A high-frequency furnace or arc furnace is used to melt the raw materials. The pull-up speed is set at about 10 - 15 mm/h, and each synthesis takes only a few hours - 10 hours. The advantage is that materials with high melting points can be reacted such as Ir (melting point: 2,446 °C) and large single crystals can be synthesized in a short time. The schematic view of the arc furnace is shown in Fig. 3.9(a). The tungsten torches are used for melting the materials using arc melting. There are four torches to improve the stability of the temperature of the melted material. A Cu-hearth corresponds to the crucible and is a water-cooled one. Arc melting was conducted under a high-quality (6N) argon gas atmosphere. Before synthesizing a single crystal, a homogeneous polycrystal sample was synthesized. The procedure of synthesizing the polycrystal was repeated several times to ensure sample homogeneity. The Czochralski method is only applicable to compounds with low-vapor pressure. When we pull up a single crystal from the melting raw materials, it is important to control the diameter of the crystal, the pulling speed, and the power of the torches. A typical necking diameter is about 1 mm, while the single crystal ingot has 3 $\simeq$ 4 mm in diameter. The growth rate is 10 - 15 mm/h to avoid stacking faults in the sample.

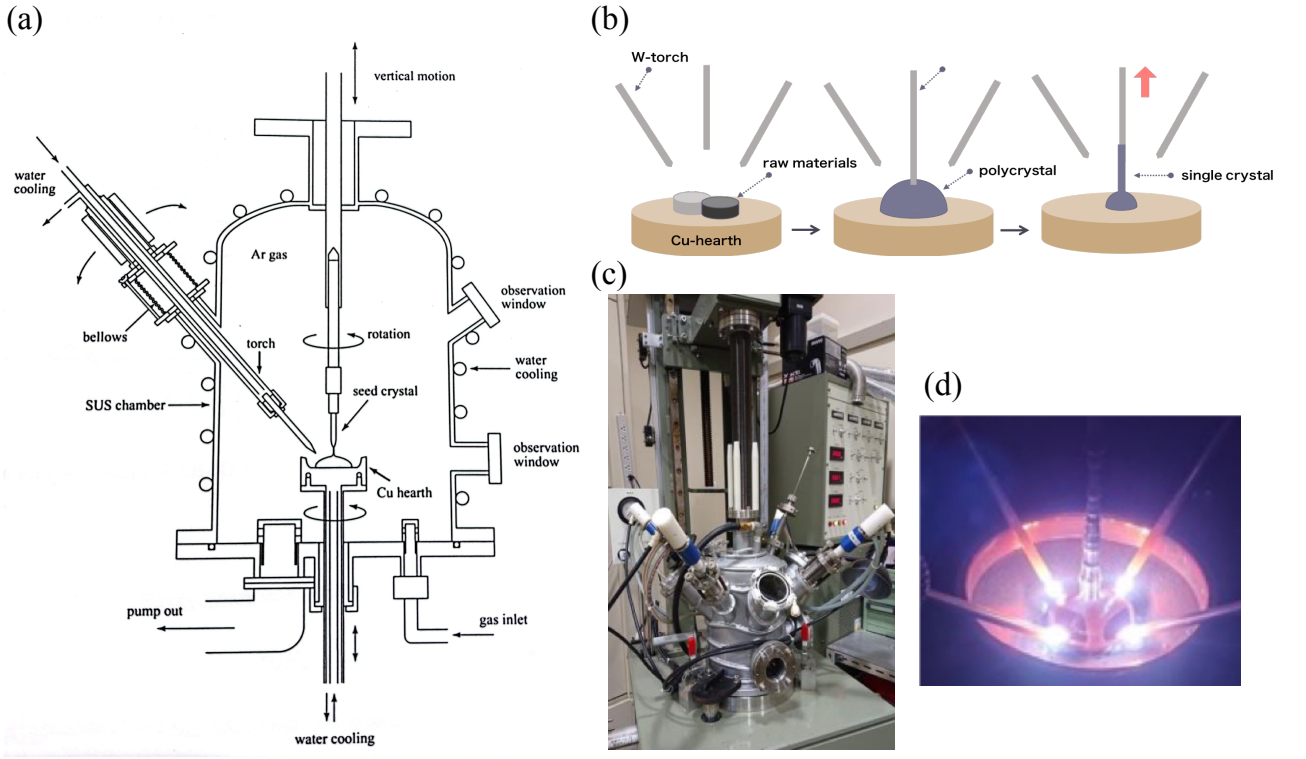

Figure 3.9: (a) Illustration of the tetra-arc furnace, after courtesy of Y Ōnuki. (b) Schematic picture of Czochralski method. Picture of (c) tetra-arc furnace (TCA4-6P, TECHNO SEARCH CORP.) and (d) a single crystal of $IrGe_4$ in growth.

Starting materials of $IrGe_4$ ware powder of 4N-Ir and ingot of 6N-Ge with a composition ratio of Ir : Ge = 1 : 4 and the total weight is 10 g. Ir-powders were pressed to make pellets for easier handling. Ir-pellets and Ge-ingots were melted using the arc furnace to ensure sample homogeneity. Since Ge has a low melting point T_m (= 938.2 °C) compared to Ir (T_m = 2.448°C), we first melted Ge, and then melted Ir. After melting the homogeneous material, the single crystal was pulled up at the speed of 15 mm/h. The photographs of single crystals are later shown in the inset of Fig. 3.14(b). As described later, one ingot is found to be an enantiopure crystal of the trigonal structure with space group $P3_121$ (No. 152), while the other ingot belongs to the chiral $P3_221$ (No. 154).

High-pressure syntheses: $RhGe_4$

High-pressure synthesis is a crystal growth method with applying ultra-GPa pressure to a sample. The high-pressure syntheses can produce materials that cannot be realized under ambient pressure; synthesizing polycrystalline diamond [94] and exploring

new superconductors such as iron-based superconductors [95, 96, 97]. In our laboratory, we have succeeded in resolving the rare-earth ion deficiency in filled skutterudite compounds using high-pressure syntheses method, leading to the elucidation of their essential physical properties [98].

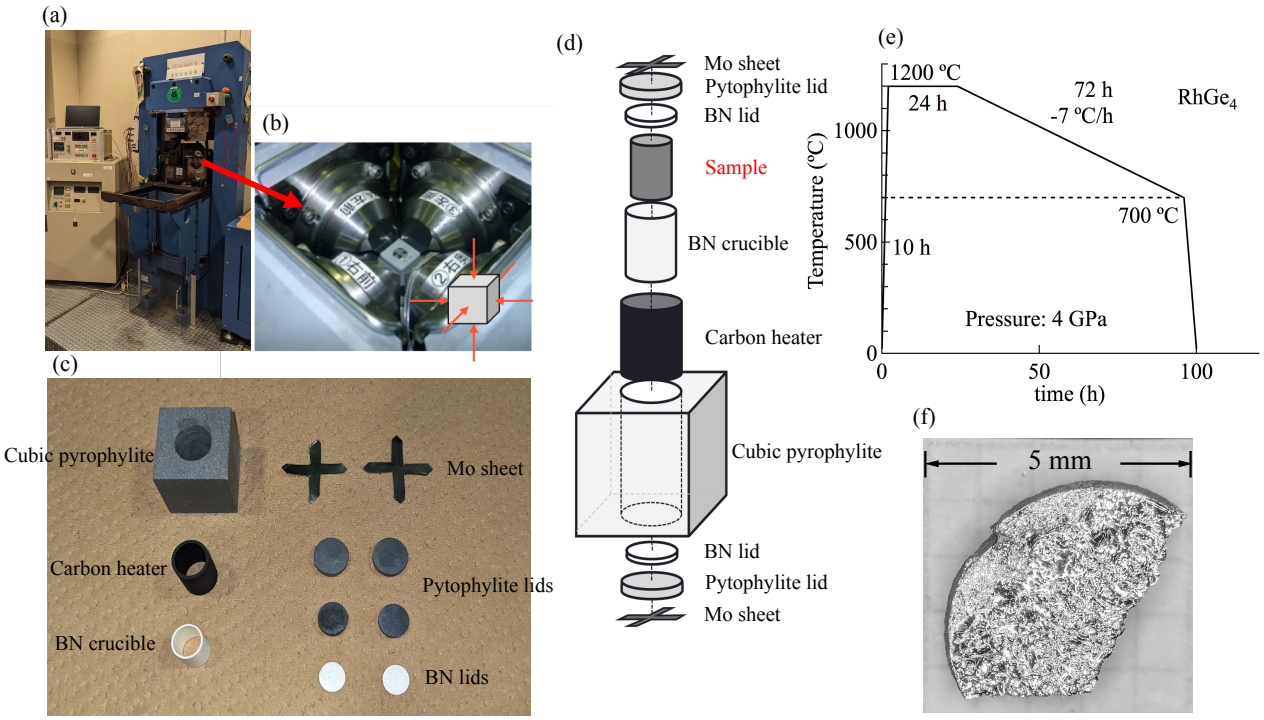

Figure 3.10: (a) Cubic-anvil high-pressure apparatus and (b) enlarged view of the cubic-anvil cell. (c),(d) Cell components of high-pressure synthesis. (e) Synthesis conditions of $RhGe_4$ and (f) synthesized crystal of $RhGe_4$.

Figure 3.10(a) shows a high-pressure syntheses apparatus of ”Piglet II” in our laboratory. This apparatus makes high pressure by a static method using a piston-cylinder and a cubic anvil cell and apply a maximum load of 700 tons. Figure 3.10(b) shows an enlarged view of the cubic anvil. The sample cell is placed in the center of the anvil system. The sample cell consists of a pyrophyllite cell, a graphite heater, Mo sheets for electrodes, and a BN crucible as shown in Fig. 3.10(c) and 3.10(d). The sample space is $6.5\phi \times 5.5$ mm^3, which is relatively larger than that of normal high-pressure syntheses apparatus. The sample cell is set in the anvil system, and then the pressure is applied to the cell, where the maximum pressure is about 6 GPa. The sample is heated up using the carbon heater, where the maximum temperature is about 1600 °C. A current flows the carbon heater through the Mo electrode sheet attached to the top and bottom of the

sample cell. After the heating process under high pressure, the sample cell was taken out from the apparatus. The sample cell becomes smaller after high-pressure treatment.

The characteristic feature of the present high-pressure syntheses apparatus is as follows. It can keep high temperatures under maximum pressure for one week. Therefore, in addition to the usual crystal syntheses in the solid state of the material, it is possible to perform the flux method under high pressure. We have succeeded in growing many single crystals such as filled skutterudite compounds of $PrFe_4Sb_{12}$ [98], $YbOs_4Sb_{12}$ [99], the pyrite compounds of CuS_2 and $CuSe_2$ [29], and so on. In particular, the crystal quality of CuS_2 and $CuSe_2$ was high enough to detect the dHvA signals [29].

In the case of $RhGe_4$, polycrystalline samples were synthesized using the present cubic-anvil-type high-pressure apparatus. Starting materials of Rh and Ge with a stoichiometric ratio were placed in a cylindrical BN crucible, which was compressed to 4 GPa, heated to 1200 °C under 4 GPa, maintained for 24 h, cooled to 700 °C in 3 days, and quenched to room temperature, as shown in Fig. 3.10(e). The polycrystalline sample was found to consist of tiny single crystals with a size of less than 1 mm. The photograph of a $RhGe_4$ is shown in Fig. 3.10(f).

3.2 Analyses of crystal structures

Powder X-ray analyses

Powder X-ray diffraction is a widely used technique to obtain information on crystal structures, such as the identification of crystalline phase and determination of lattice constant, and so on. Powder X-ray diffraction is based on Bragg's law;

$$2d_{hkl}\sin\theta = n\lambda, \tag{3.1}$$

where d_{hkl} is the lattice spacing of the crystal plane with the Miller index (h k l), λ is the wavelength of the X-ray, and n is the order of the diffraction. Figure 3.11(a) shows a schematic picture of powder X-ray diffraction. The incident X-rays hits the sample. The angle of the incident X-ray with the sample plane is θ, while the angle with the diffracted X-ray is 2θ, therefore, the detector is placed at the angle of 2θ with the incident X-rays ($\theta/2\theta$-scan). Analyzing a graph that plots the intensities of the detector as a function of the 2θ provides various information about the crystal structure. The basic information obtained from powder X-ray diffraction is the lattice constant. In the case of the hexagonal lattice, The d_{hkl} is expressed using the lattice constant and the

Miler index as follows;

$$d_{hkl} = \frac{1}{\sqrt{\frac{4}{3}\frac{(h^2+hk+k^2)}{a^2} + \frac{l^2}{c^2}}}. \tag{3.2}$$

Since d_{hkl} is obtained from eq. (3.1) using the peak position, it is essential to read the peak position accurately. Differentiating eq. (3.1) by θ gives the following equation,

$$\frac{\Delta d}{d} = -\Delta\theta \cot\theta. \tag{3.3}$$

As θ approaches 90° (high angle region), the error of the lattice constant $\Delta\theta/\theta$ decreases. The lattice constant is obtained by extrapolating to $2\theta = 180°$, where the angle error is the smallest. X-ray powder diffraction measurements were performed using a Rigaku SmartLab with Cu-K_α radiation.

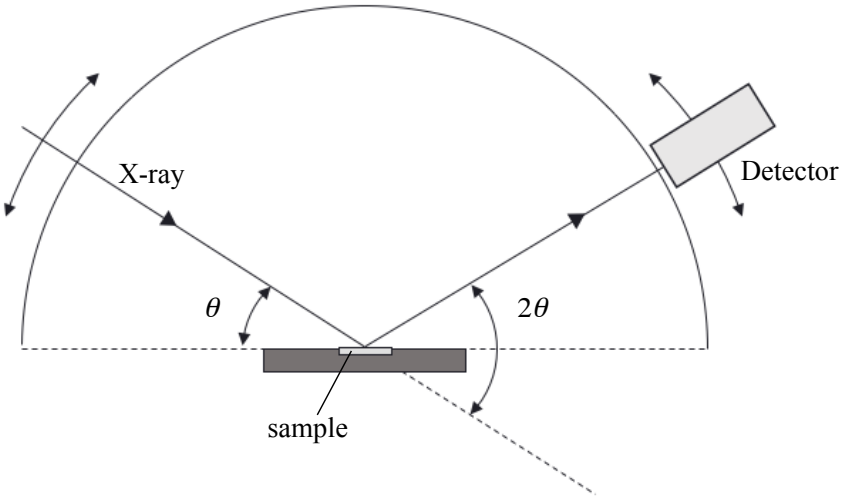

Figure 3.11: Schematic illustration of θ-2θ-scan of powder X-ray diffraction.

Figures 3.12(a), 3.12(b), 3.12(c), and 3.12(d) show the powder X-ray diffraction patterns for α-$IrSn_4$, α-$RhSn_4$, $IrGe_4$, and $RhGe_4$, respectively. No impurities were found in α-$IrSn_4$, α-$RhSn_4$, and $IrGe_4$ within the experimental accuracy, while Ge impurities were present in $RhGe_4$, as shown by the arrows in Fig. 3.12(d). The lattice constants determined from the powder X-ray are summarized in Table 3.2.

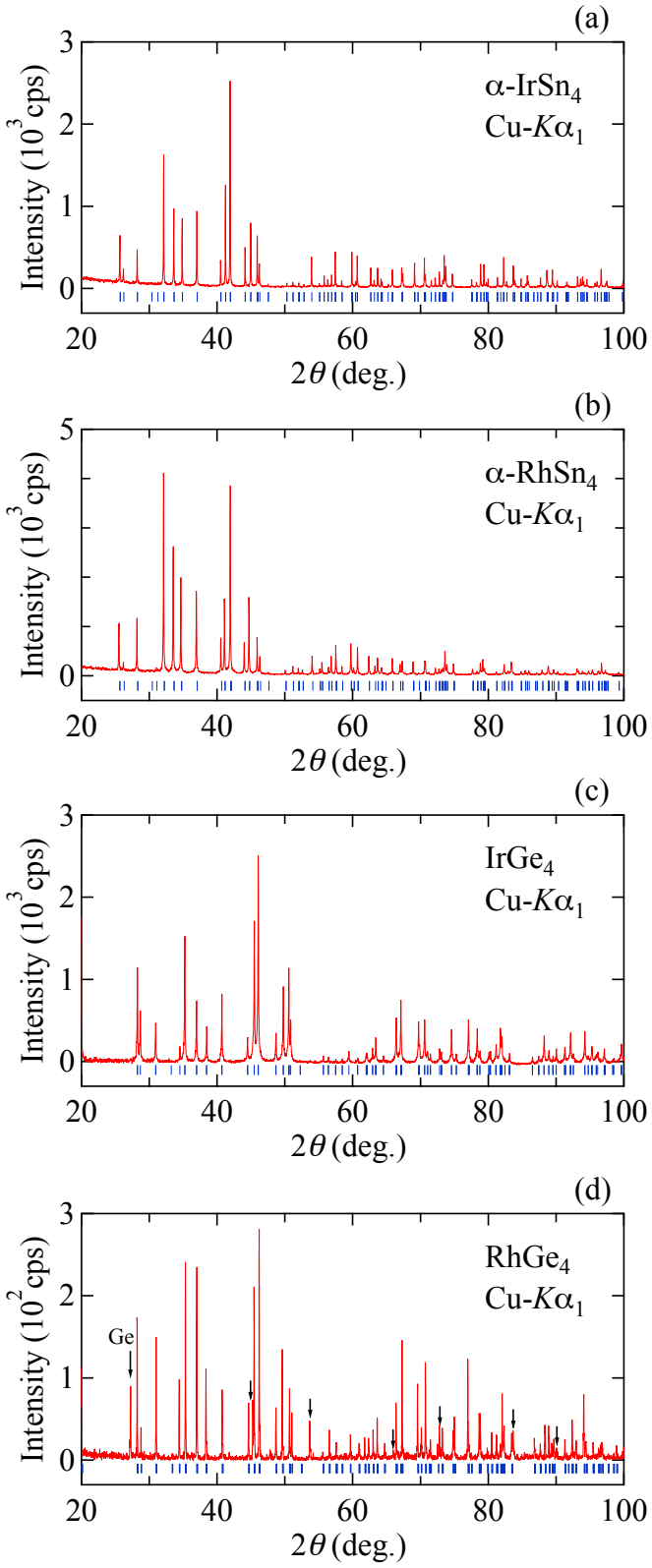

Figure 3.12: Powder X-ray diffractions of (a) α-$IrSn_4$, (b) α-$RhSn_4$, (c) $IrGe_4$, and (d) $RhGe_4$.

Table 3.2: Atomic coordinates and thermal parameters of (a) α-$IrSn_4$, (b) α-$RhSn_4$, (c) $IrGe_4$, and (d) $RhGe_4$ at 300 K determined by single-crystal X-ray diffraction measurements ($2\theta_{max}$ = 54.9 °). R_1 and wR_2 are the reliability factors and B_{eq} is the equivalent isotropic atomic displacement parameter.

(a) α-$IrSn_4$

$P3_121$ (No. 152), a = 6.8017(9) Å, c = 8.5769(15) Å, V = 343.63(9) Å^3, Z = 3

			Position				
Atom	Site		x	y	z	B_{eq}(Å^2)	occ
Ir	3b	(.2.)	0.31214(11)	0	5/6	0.46(2)	1
Sn(1)	6c	(2)	0.23332(2)	0.4980(3)	0.4330(9)	0.71(3)	1
Sn(2)	3a	(.2.)	0.08990(2)	0	1/3	0.69(3)	1
Sn(3)	3a	(.2.)	0.63130(2)	0	1/3	0.69(2)	1

R_1 = 2.86 %, wR_2 = 5.89 %, Flack parameter = 0.04(4)

(b) α-$RhSn_4$

$P3_121$ (No. 152), a = 6.7836(7) Å, c = 8.6159(10) Å, V = 343.31(8) Å^3, Z = 3

			Position				
Atom	Site		x	y	z	B_{eq}(Å^2)	occ
Rh	3b	(.2.)	0.3111(4)	0	5/6	0.48(2)	1
Sn(1)	6c	(2)	0.2364(9)	0.5001(10)	0.4299(7)	0.75(1)	1
Sn(2)	3a	(.2.)	0.0912(9)	0	1/3	0.78(2)	1
Sn(3)	3a	(.2.)	0.6305(11)	0	1/3	0.75(2)	1

R_1 = 2.25 %, wR_2 = 4.56 %, Flack parameter = 0.05(4)

(c) $IrGe_4$

$P3_121$ (No. 152), a = 6.209(8) Å, c = 7.779(10) Å, V = 259.8(6) Å^3, Z = 3

			Position				
Atom	Site		x	y	z	B_{eq}(Å^2)	occ
Ir	3b	(.2.)	0.3177(2)	0	5/6	0.39(2)	1
Ge(1)	6c	(2)	0.22030(2)	0.48590(2)	0.44788(14)	0.68(2)	1
Ge(2)	3a	(.2.)	0.07839(3)	0	1/3	0.66(3)	1
Ge(3)	3a	(.2.)	0.61759(7)	0	1/3	0.63(3)	1

R_1 = 2.58 %, wR_2 = 5.14 %, Flack parameter = 0.03(2)

(d) $RhGe_4$

$P3_121$ (No. 152), a = 6.1941(11) Å, c = 7.8035(16) Å, V = 259.28(8) Å^3, Z = 3

			Position				
Atom	Site		x	y	z	B_{eq}(Å^2)	occ
Rh	3b	(.2.)	0.3172(2)	0	5/6	0.38(2)	1
Ge(1)	6c	(2)	0.2232(2)	0.4883(8)	0.4451(10)	0.68(2)	1
Ge(2)	3a	(.2.)	0.0771(2)	0	1/3	0.71(3)	1
Ge(3)	3a	(.2.)	0.6159(2)	0	1/3	0.65(3)	1

R_1 = 2.98 %, wR_2 = 5.99 %, Flack parameter = 0.04(4)

Analyses of single crystal structures

The crystal structural analyses are a technique to determine the crystal information, such as lattice parameters, positional parameters, thermal parameters, and so on. The X-ray diffraction intensity from the crystal plane d_{hkl} is proportional to the structural factor, which gives information about the structure. The structural factor is related to the electron density distribution $\rho(\boldsymbol{r})$ in the unit cell and is expressed as follows;

$$F(\boldsymbol{k}) = \int_{\text{unit cell}} \rho(\boldsymbol{r}) e^{2\pi i \boldsymbol{k}\cdot\boldsymbol{r}} d^3\boldsymbol{r}. \tag{3.4}$$

The inverse Fourier transforming of the structural factor provides the charge density distribution in the unit cell;

$$\rho(\boldsymbol{r}) = \frac{1}{V} \int_{\Sigma} F(\boldsymbol{k}) e^{-2\pi i \boldsymbol{k}\cdot\boldsymbol{r}} d^3\boldsymbol{k}, \tag{3.5}$$

where V is the volume of the unit cell and Σ is the entire reciprocal lattice space. The parameters of the atomic coordinates are adjusted to minimize the difference between the measured value $|F_0(hkl)|$ and the calculated value $|F_c(hkl)|$. The degree of agreement between $|F_0(hkl)|$ and$|F_c(hkl)|$ is given by two factors called the R factor and wR_2 factor (reliability factor);

$$R_1 = \frac{\sum_{hkl}(|F_0(hkl)| - |F_c(hkl)|)}{\sum_{hkl}|F_0(hkl)|} \tag{3.6}$$

$$wR_2 = \left[\frac{\sum_{hkl} w(hkl) \left\{ |F_0(hkl)|^2 - |F_c(hkl)|^2 \right\}^2}{\sum_{hkl} w(hkl) |F_0(hkl)|^4} \right]^{\frac{1}{2}}. \tag{3.7}$$

In the case of the chiral structure, the Flack parameter is useful to determine the chirality of the noncentrosymmetric structure by the single crystal X-ray diffraction analyses under consideration of the resonant scattering (the anomalous dispersion effect) as described in Sect. 2.2.

Single crystal X-ray diffraction analyses were also performed using a Rigaku XtaLABmini with graphite monochromated Mo-K_α radiation, as shown in Fig. 3.13(b). A small single crystal with a size of 0.1^3 mm^3 was selected to minimize the absorption as well as a secondary extinction effect. Every single crystal was mounted on a glass fiber with epoxy, as shown in Fig. 3.13(a). The structural parameters were refined using the program SHELXL-97 [100].

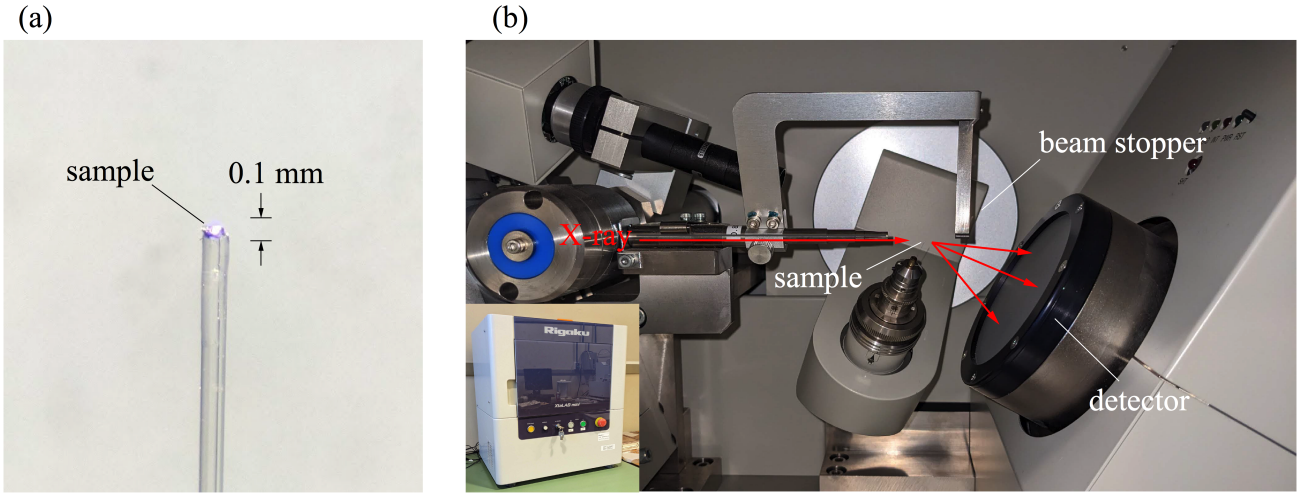

Figure 3.13: (a) Prepared single crystal sample for single crystal structural analyses and (b) single crystal structural analyses apparatus of XtaLABmini (Rigaku).

Tables 3.2(a), 3.2(b), 3.2(c), and 3.2(d) indicate the crystallographic parameters of α-$IrSn_4$, α-$RhSn_4$, $IrGe_4$, and $RhGe_4$, respectively. Note that we succeeded in carrying out the single crystal X-ray diffraction analyses of $RhGe_4$.

Figure 3.14(a) shows the determined Flack parameters for twelve single crystalline pieces of α-$IrSn_4$. It was found that the values of x fall into two groups: $-0.035 < x < 0.01$ for $P3_121$ and $0.95 < x < 0.99$ for $P3_221$. For both groups, the absolute deviation from $x = 0$ is smaller than 0.05, which is the typical criterion for the sufficiently precise determination of the absolute structure. This fact strongly indicates that each crystal is not twinned and is composed of a single phase categorized into either $P3_121$ (No. 152) or $P3_221$ (No. 154). Similar results were also obtained for $IrGe_4$ single crystal ingots grown using the Czochralski method, as shown in Fig. 3.14(b).

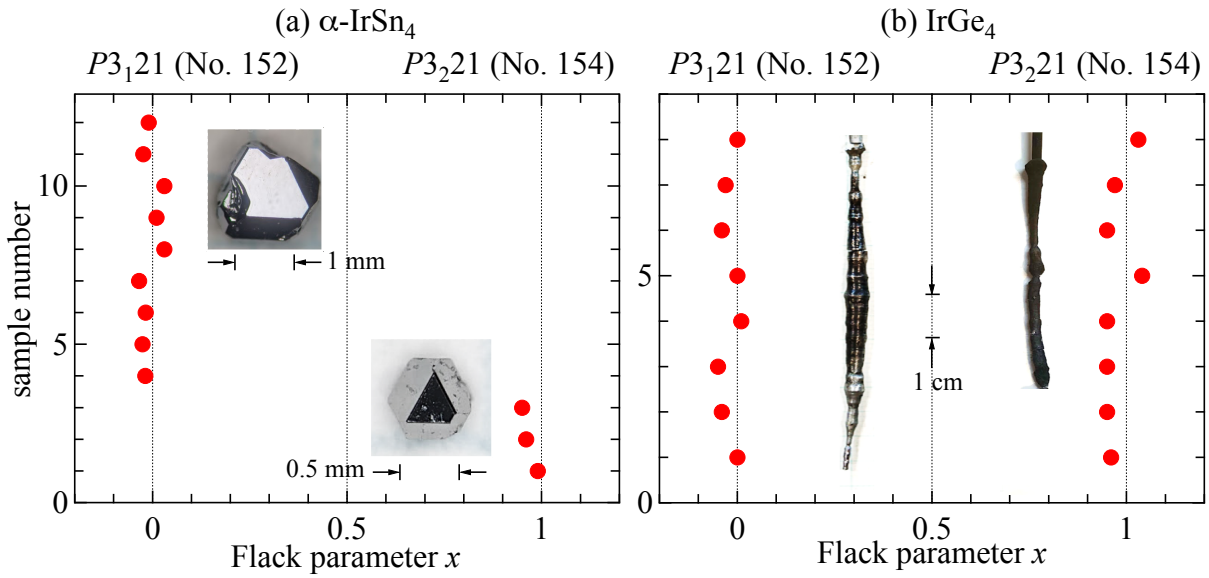

Figure 3.14: Flack parameters x based on $P3_121$ and $P3_221$ determined by the single-crystal X-ray diffractions for twelve α-$IrSn_4$ single crystals and (b) sixteen $IrGe_4$ single crystals.

Crystal orientation: Laue method

It is necessary to process the sample for various measurements properly. In particular, the determination of the sample orientation is the most important. The crystal orientation was determined using the back reflection Laue method. White X-rays are incident on a fixed crystal from a fixed direction. Reflections from each crystal plane are enhanced when Bragg's law is satisfied, producing Laue spots. Since the Laue spots correspond one-to-one with the lattice planes, the obtained Laue photograph is related to the orientation of the crystal.

Figures. 3.16(a)-(c) show simulation of Laue photograph of α-$IrSn_4$ for the $\langle 0001 \rangle$, $\langle 11\bar{2}0 \rangle$, and $\langle 10\bar{1}0 \rangle$ directions. Since the Laue group of α-$IrSn_4$ is D_{3d} ($\bar{3}$m), there are $\bar{3}$ rotoinversion axis parallel to $\langle 0001 \rangle$, 2 rotation axis parallel to $\langle 11\bar{2}0 \rangle$, and a mirror plane perpendicular to $\langle 11\bar{2}0 \rangle$. The simulation satisfies the symmetry of the Laue group. The 4-axis representations of the Hexagonal lattice are shown in Fig. 3.17(c) and 3.17(b).

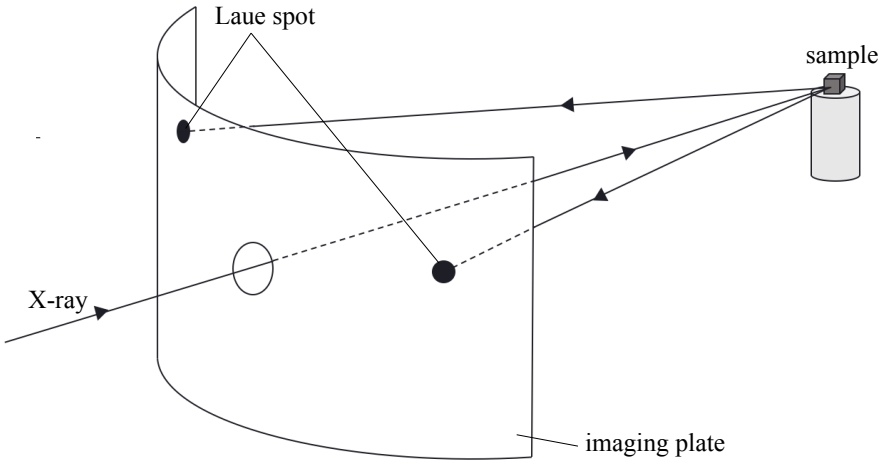

Figure 3.15: (a) Schematic picture of back reflection Laue method.

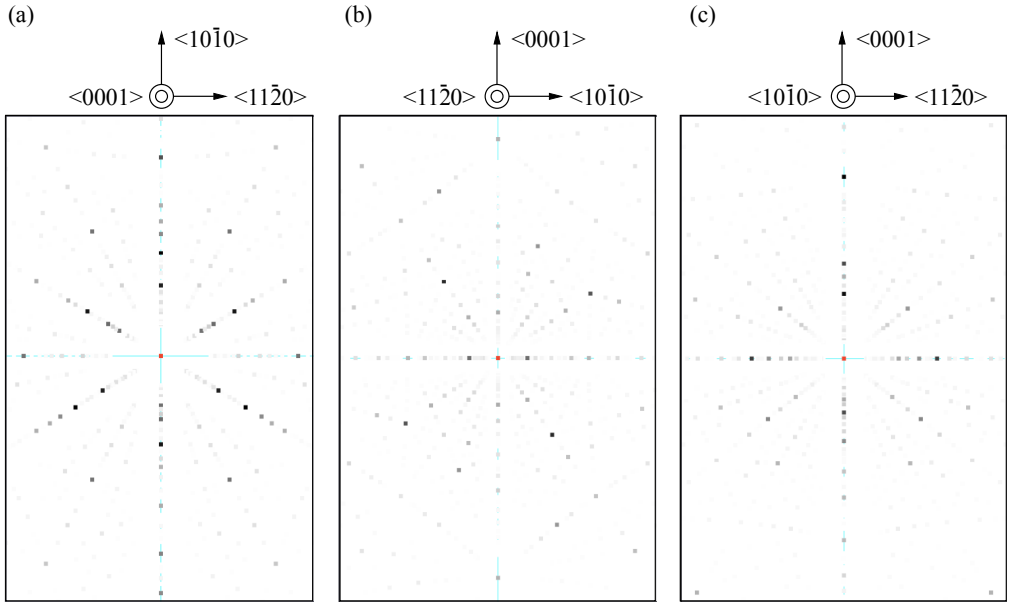

Figure 3.16: Simulation of Laue photographs of α-$IrSn_4$ for (a) $\langle 0001 \rangle$, (b) $\langle 11\bar{2}0 \rangle$, and (c) $\langle 10\bar{1}0 \rangle$

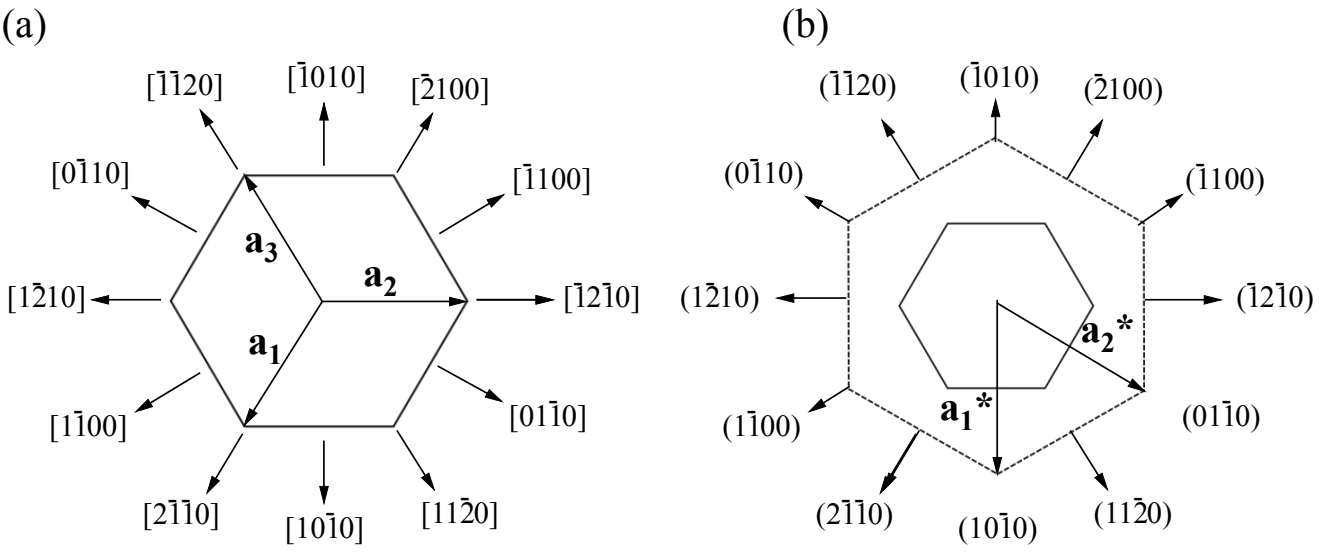

Figure 3.17: 4-axis representation of Hexagonal lattice in (a) real space and (b) reciprocal space.

3.3 Experimental method

Electrical resistivity

Electrical resistivity is a physical property of a material that measures how strongly it resists the electric current. In the electric field E_x along the x-axis, which is parallel to the direction of the current J, the average velocity of a conduction electron v_x is expressed as

$$m^* \frac{dv_x}{dt} = -eE_x - \frac{m^* v_x}{\tau}, \tag{3.8}$$

where $-m^* v_x/\tau$ is the frictional or dumpling force and τ is the scattering lifetime. In a steady state where $dv_x/dt = 0$, Ohm's law is obtained using the expression for a steady current $J_x = -nev_x$ (n: carrier density);

$$J_x = \frac{ne^2\tau}{m^*} E_x = \sigma E_x = \frac{1}{\rho} E_x, \tag{3.9}$$

$$\rho = \frac{m^*}{ne^2\tau}, \tag{3.10}$$

where ρ is the electrical resistivity and $\sigma(= 1/\rho)$ is the electrical conductivity.

The electrical resistivity $\rho(T)$ in non-magnetic intermetallic compounds consists of three contributions: the electron scattering due to non-magnetic impurities and crys-

talline defects ρ_0, the electron-phonon scattering $\rho_{\mathrm{ph}}(T)$, and the electron-electron scattering $\rho_{\mathrm{e-e}}(T)$,

$$\rho(T) = \rho_0 + \rho_{\mathrm{ph}}(T) + \rho_{\mathrm{e-e}}(T). \tag{3.11}$$

This yields Mattiessen's rule.

The ρ_0 value is constant with temperature variation. This value is important for one to know the quality of a sample, which is estimated by determining the residual resistivity ratio (RRR = $\rho_{\mathrm{RT}}/\rho_0, \rho_{\mathrm{RT}}$: resistivity at room temperature). A large value of RRR indicates a high-quality sample which corresponds to a low ρ_0 value.

The temperature dependence of ρ_{ph} is based on the well-known Grüneisen's formula. It is proportional to T above the Debye temperature θ_{D} and proportional to T^5 far below the Debye temperature. Grüneisen's formula is

$$\rho_{\mathrm{ph}}(T) = \frac{C}{M\theta_{\mathrm{D}}}\left(\frac{T}{\theta_{\mathrm{D}}}\right)^5 \int^{\theta_D/T} \frac{x^5}{(1-e^{-x})(e^x-1)}dx \tag{3.12}$$

$$= \begin{cases} \propto T & \left(T \geq \frac{\theta_{\mathrm{D}}}{2}\right) \\ \propto T^5 & (T \ll \theta_{\mathrm{D}}), \end{cases} \tag{3.13}$$

where C is constant and independent of the compound, and M is the mass of the compound.

The electron-electron scattering contribution $\rho_{\mathrm{e-e}}(T)$ at low temperatures is expressed as

$$\rho_{\mathrm{e-e}}(T) = AT^2, \tag{3.14}$$

where the coefficient $\sqrt{A}$ is proportional to the effective mass. In a simple metal, $\rho_{\mathrm{e-e}}$ is much smaller than ρ_{ph}.

The electrical resistivity ρ is measured using a very simple technique but contains abundant information about the sample under consideration. The electrical voltage V between two lead wires on the sample, with a length l, is measured for a rectangle sample, with a cross-sectional area S in a current I. The electrical resistance R is obtained via Ohm's law, where $R = V/I$. We usually consider the electrical resistivity $\rho = (S/l)R$ instead of R, as it is independent of the sample dimensions and geometry.

Magnetoresistance

The electrical resistivity ρ under magnetic field H is called magnetoresistance $\rho(H)$. The transverse magnetoresistance in the configuration of $\boldsymbol{J} \perp \boldsymbol{H}$ provides important

information about the Fermi surface. The longitudinal magnetoresistance in the configuration of $\boldsymbol{J} \parallel \boldsymbol{H}$ is also measured to determine the effect of the magnetic field on the sample. We consider a non-magnetic metal with two kinds of carriers with electron and hole Fermi surfaces. H is parallel to the k_z direction $\boldsymbol{H} = (0, 0, H)$ and J is parallel to the k_x direction $\boldsymbol{J} = (J_x, 0, 0)$. The relationship between the current J_x and the electric field E_x is expressed as

$$J_x = \left[\left(\frac{n_1 q_1}{\mu_1} + \frac{n_2 q_2}{\mu_2} \right) \left(\frac{c}{H} \right)^2 + \frac{(n_1 q_1 + n_2 q_2)^2}{\dfrac{n_1 q_1}{\mu_1} + \dfrac{n_2 q_2}{\mu_2}} \right] E_x. \tag{3.15}$$

Under the high field condition $\alpha = \mu H/c = \omega_c \tau \gg 1$, the magnetoresistance varies depending on whether the sample is a compensated metal with an equal carrier number of electrons and holes, $n_\mathrm{e} = n_\mathrm{h}$, or an uncompensated metal, $n_\mathrm{e} \neq n_\mathrm{h}$, and whether an open orbit exists or not. Here, $\omega_c \tau = qH/m_c^* c$ is the cyclotron frequency, τ is the scattering lifetime, m_c^* is the cyclotron effective mass, and $\omega_c \tau / 2\pi$ is the number of cyclotron motions performed by the carrier without being scattered.

(I) only closed orbit under high field limit condition ($\alpha \gg 1$)

a) compensated metal ($n_\mathrm{e} = n_\mathrm{h}$)
In the case of a compensated metal of $n_1 q_1 + n_2 q_2 = 0$, namely $q_1 = +e$, $q_2 = -e$, and $n_1 = n_2 = n$, the magnetoresistance is expressed as

$$\rho(H) = \frac{1}{\dfrac{n_1 q_1}{\mu_1} + \dfrac{n_2 q_2}{\mu_2}} \left(\frac{H}{c} \right)^2 \tag{3.16}$$

b) uncompensated metal ($n_\mathrm{e} \neq n_\mathrm{h}$)
The magnetoresistance is expressed as

$$\rho(H) = \left[\frac{(n_1 q_1 + n_2 q_2)^2}{\frac{n_1 q_1}{\mu_1} + \frac{n_2 q_2}{\mu_2}} \right]^{-1}, \tag{3.17}$$

where $n_1 q_1 + n_2 q_2 \neq 0$. Namely, $\rho(H)$ saturates under the high field.

Schematic figures of the magnetoresistance with only closed orbits are shown in Fig. 3.18.

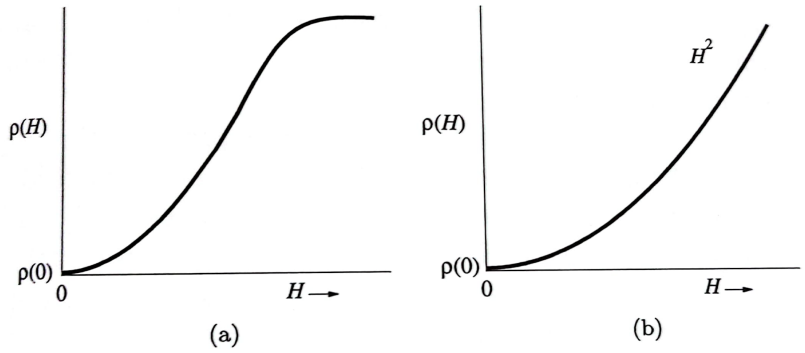

Figure 3.18: Magnetoresistance with only closed orbits in the case of (a) an uncompensated metal and (b) a compensated metal.

(II) existence of open orbit under high field condition ($\alpha \gg 1$)
The magnetoresistance is independent of the state of compensation and increases quadratically as

$$\rho(H) \sim H^2 \cos^2\phi, \tag{3.18}$$

where ϕ is the angle between the current and open orbit direction in $\boldsymbol{k}$-space. Figure 3.19 shows the transverse magnetoresistance behavior for a metal with a partially cylindrical Fermi surface whose cylinder axis is in the k_z-plane and deviates by an angle Φ from the k_x-axis. The current $\boldsymbol{J}$ is directed along the k_x-axis and the magnetic field $\boldsymbol{H}$ rotates in the k_x-plane. In this case, the transverse magnetoresistance increases as $H^n(1 < n \leq 2)$ for the general direction of the field. When the magnetoresistance saturates for a particular field direction, some open orbits exist with directions parallel to $\boldsymbol{J} \times \boldsymbol{H}$; $\phi = \pi/2$ in $\boldsymbol{k}$-space. Experimentally, the current direction is fixed with respect to a crystal symmetry axis of the sample which is slowly rotated in a constant magnetic field perpendicular to the current direction. The presence of open orbits is revealed through the presence of spikes against a low background for the uncompensated metal and dips against a large background for the compensated metal, as shown in Figs. 3.19(c) and 3.19(d), respectively.

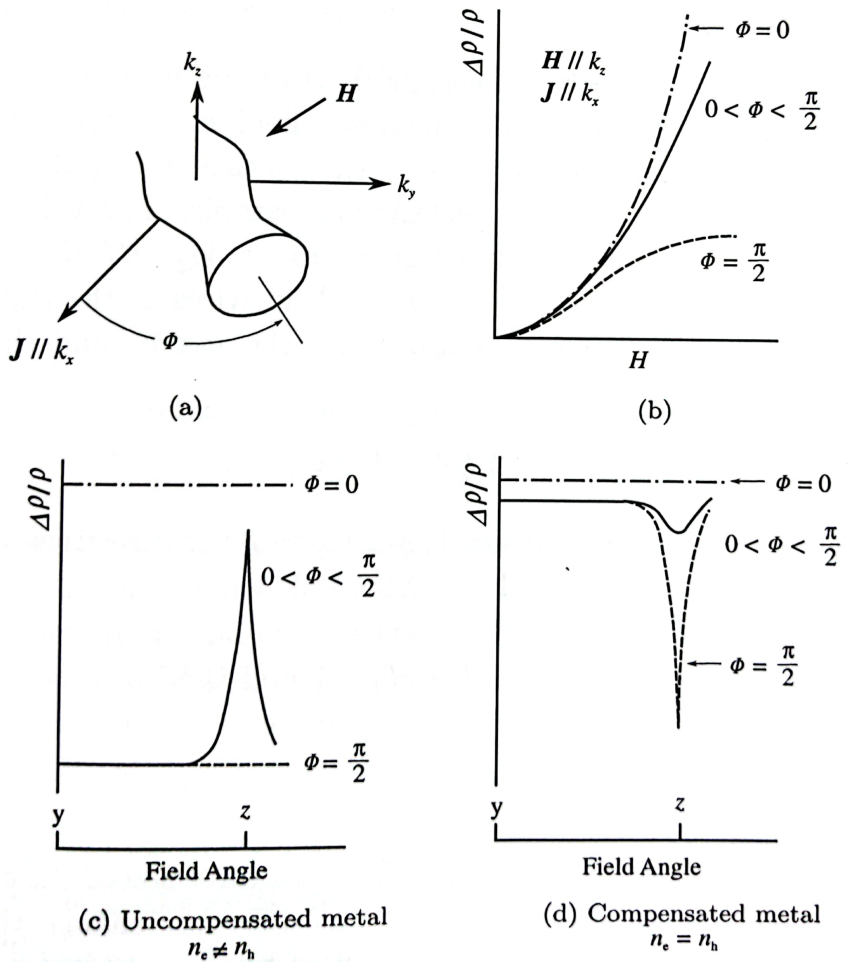

Figure 3.19: Schematic pictures of the transverse magnetoresistance with a open orbit in uncompensated and compensated metals.

specific heat

The specific heat (heat capacity) C is measured by the quasi-adiabatic heat pulse method. We give a heat pulse ΔQ to the sample and measure a change of the temperature ΔT, then

$$C = \frac{\Delta Q}{\Delta T} = \frac{I \cdot V \cdot \Delta t}{\Delta T}, \tag{3.19}$$

where I and V are the current and the voltage flowing to the heater, respectively, Δt is the duration of heating. At low temperatures, the specific heat is written as the sum of

electronic, lattice, magnetic and nuclear contributions,

$$C = C_{\rm el} + C_{\rm ph} + C_{\rm nuc} \tag{3.20}$$

$$= \gamma T + \beta T^3 + \frac{A}{T^2} \tag{3.21}$$

$$A = \frac{\hbar^2 \gamma_n^2}{3k_{\rm B}^2} I(I+1) H_{\rm in}^2, \tag{3.22}$$

where A, γ and β are the constants.

The electronic term $C_{\rm e}$ is linear in T. If we can neglect the magnetic and nuclear contributions, it is convenient to exhibit the experimental values of C as a plot of C/T versus T^2:

$$\frac{C}{T} = \gamma + \beta T^2. \tag{3.23}$$

Then we can estimate the electronic specific heat coefficient γ. Using the density of states $D(E_{\rm F})$, the coefficient can be expressed as

$$\gamma = \frac{2\pi^2}{3} k_{\rm B}^2 D(E_{\rm F}). \tag{3.24}$$

Since $D(E_{\rm F})$ is proportional to the electron mass, γ possesses an extremely large value in the heavy fermion compound.

Next, we consider $C_{\rm ph}$ based on the Debye T^3 law;

$$C_{\rm ph} = 9Nk_{\rm B} \left(\frac{T}{\theta_{\rm D}}\right)^3 \int_0^{\theta_D/T} \frac{x^4 e^x}{(e^x - 1)^2} dx \tag{3.25}$$

$$\simeq \frac{12\pi^4 N k_{\rm B}}{5} \left(\frac{T}{\theta_{\rm D}}\right)^3 \tag{3.26}$$

$$\equiv \beta T^3 \left(T < \frac{\theta_{\rm D}}{50}\right) \tag{3.27}$$

where $\theta_{\rm D}$ is the Debye temperature and N is the number of atoms. For the actual lattices, the temperatures at which the T^3 approximation holds are quite low. Temperatures below $T = \theta_{\rm D}/50$ may be required to get a reasonably pure T^3 law, where $\theta_{\rm D}$ is usually in the range 150-400 K.

de Haas-van Alphen (dHvA) effect

Under a strong magnetic field, the orbital motion of conduction electrons is quantized and forms Landau levels. A sharp change in the free energy of the electron system appears when a Landau level crosses the Fermi energy E_{F}. Thereby, various physical quantities show a periodic variation as a function of H^{-1}. In a three-dimensional system, this sharp structure is observed when a Landau level is just across the extremal areas of the Fermi surface, perpendicular to the field direction and enclosed by the Fermi energy because the density of states also becomes extremal. From the field and temperature dependences of the oscillations in the various physical quantities, we can obtain the extremal area S, the cyclotron mass m_{c}^{*} and the scattering lifetime τ for the cyclotron orbit, and is called the de Haas-van Alphen (dHvA) effect. It provides one of the best tools for the investigation of Fermi surfaces of metals.

The theoretical expression for the oscillatory component of magnetization M_{osc} due to the conduction electrons was given by Lifshitz and Kosevich as follows [101, 102],

$$M_{\mathrm{osc}} = \sum_{r}\sum_{i} \frac{(-1)^{r}}{r^{3/2}} A_i \sin\left(\frac{2\pi r F_i}{H} + \beta_i\right), \tag{3.28}$$

$$A_i = F H^{1/2} \left|\frac{\partial^2 S_i}{\partial k_{\mathrm{H}}^2}\right|^{-1/2} R_{\mathrm{T}} R_{\mathrm{D}} R_{\mathrm{S}}, \tag{3.29}$$

$$R_{\mathrm{T}} = \frac{\alpha r m_{\mathrm{c}i}^{*} T/H}{\sinh(\alpha r m_{\mathrm{c}i}^{*} T/H)}, \tag{3.30}$$

$$R_{\mathrm{D}} = \exp(-\alpha r m_{\mathrm{c}i}^{*} T_{\mathrm{D}}/H), \tag{3.31}$$

$$R_{\mathrm{S}} = \cos(\pi g_i r m_{\mathrm{c}i}^{*}/2m_0), \tag{3.32}$$

$$\alpha = \frac{2\pi^2 k_{\mathrm{B}}}{e\hbar}. \tag{3.33}$$

Here, the magnetization is periodic in $1/H$ with a dHvA frequency F_i;

$$\begin{aligned} F_i &= \frac{\hbar c}{2\pi e} S_i \\ &= 1.048 \times 10^{-8} [\mathrm{Oe} \cdot \mathrm{cm}^2] \cdot S_i, \end{aligned} \tag{3.34}$$

which is directly proportional to the $i{-}th$ extremal (maximum or minimum) cross-sectional area S_i $(i = 1, \ldots, n)$. The extremal area in a spherical Fermi surface is shown as a mesh plane in Fig. 3.20(a). On the other hand, three extremal areas exist in a dumbbell-shaped Fermi surface, as shown in Fig. 3.20(b).

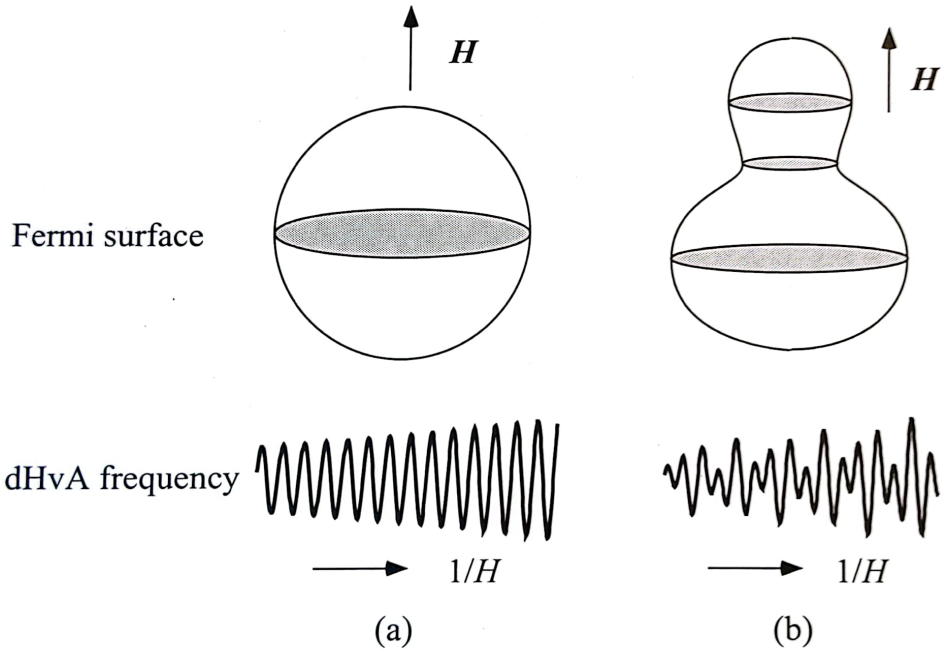

Figure 3.20: Simulations of the cross-sectional area and its dHvA signal for a simple Fermi surface. There is one dHvA frequency in (a), while there are three different frequencies in (b).

The factor R_{T} in the amplitude A_i is related to the thermal damping at finite temperature T. The factor R_{D} is related to the Landau level broadening $k_{\mathrm{B}}T_{\mathrm{D}}$. Here, T_{D} is due to both the lifetime broadening and inhomogeneous broadening caused by impurities, crystalline imperfections, or strains. T_{D} is called the Dingle temperature and is given by

$$\begin{aligned} T_{\mathrm{D}} &= \frac{\hbar}{2\pi k_{\mathrm{B}}}\tau^{-1} \\ &= 1.22 \times 10^{-12}[\mathrm{K}\cdot\mathrm{sec}]\cdot\tau^{-1}. \end{aligned} \tag{3.35}$$

The factor R_{S} is called the spin factor and is related to the difference of phase between the Landau levels due to the Zeeman split. When $g_i = 2$ (free electron value) and $m_{\mathrm{c}}^* = 0.5m_0$, this term becomes zero for $r = 1$, and fundamental oscillations vanish for all values of the fields. This is called oscillation cancel out, and this can be useful for determining the value of g_i. Note that in this situation the second harmonics for $r = 2$ should give a full amplitude.

The quantity $\left|\partial^2 S/\partial k_{\mathrm{H}}^2\right|^{-1/2}$ is called the curvature factor. The rapid change of the cross-sectional area around the extremal area along the field direction diminishes the

dHvA amplitude for this extremal area.

The detectable conditions of dHvA effect are as follow;

1. The distance between the Landau levels $\hbar\omega_c$ must be larger than the thermal broadening width $k_B\omega_c \gg k_BT$ (high field, low temperature).
2. At least one cyclotron motion must be performed during the scattering, namely, $\omega_c\tau/2\pi > 1$ (high-quality sample).
3. The fluctuation of the static magnetic field must be smaller than the field interval of one cycle of the dHvA oscillation (homogeneity of the magnetic field).

Shape of Fermi surface

The angular dependence of dHvA frequencies gives important information about the shape of Fermi surface. As a volume of Fermi surface corresponds to a carrier number, we can obtain the carrier number of metal directly.

We show the typical Fermi surfaces and their angular dependences of dHvA frequencies in Fig. 3.21. In a spherical Fermi surface, the dHvA frequency is constant for any field direction. On the other hand, in a cylindrical Fermi surface such as in Fig.3.21(a), it takes a minimum value for the field along the z-axis. These relatively simple Fermi surfaces can be determined only by the dHvA experiment. However, exact information from an energy band calculation is needed to determine a complicated one.

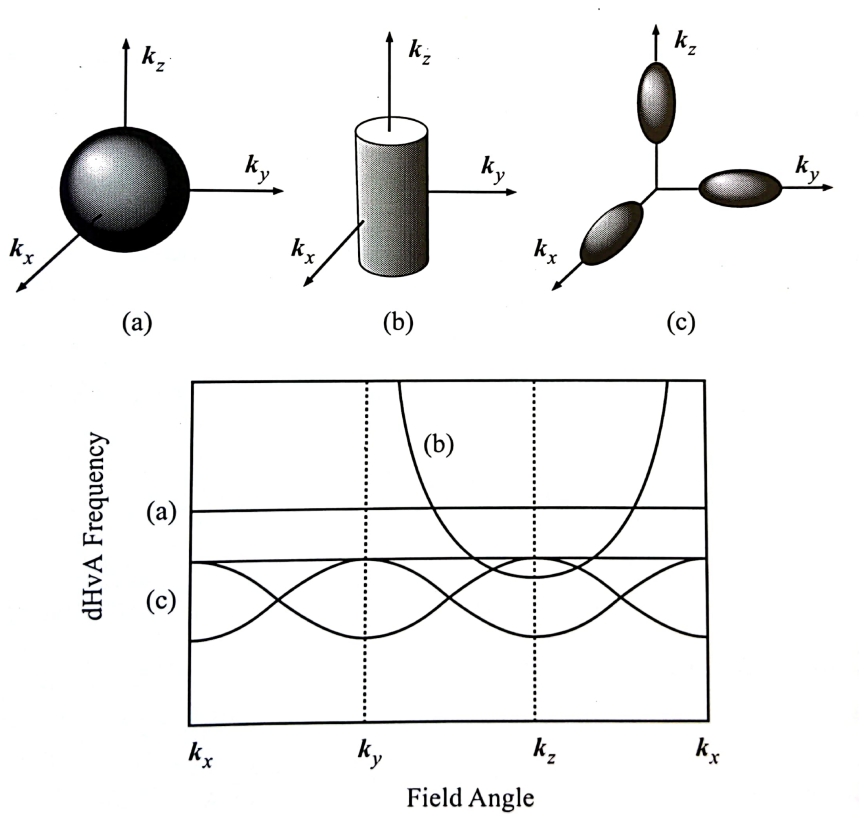

Figure 3.21: Angular dependences of the dHvA frequencies in three typical Fermi surfaces (a) sphere, (b) cylinder, and (e) ellipsoid.

Cyclotron effective mass

We can determine the cyclotron effective mass m^*_{ci} from measurements of the temperature dependence of a dHvA amplitude. Equation (3.30) is transformed into;

$$\ln\left\{A_i\left[1-\exp\left(\frac{-2\lambda m^*_{ci}T}{H}\right)\right]/T\right\} = \frac{-\lambda m^*_{ci}}{H}T + \text{const.} \tag{3.36}$$

From the slope of a plot of $\ln\left\{A_i\left[1-\exp\left(\frac{-2\lambda m^*_{ci}T}{H}\right)\right]/T\right\}$ versus T at a constant field H, the effective mass can be obtained.

Let us consider the relation between the cyclotron mass and electrical specific heat γ. Using a density of states $D(E_F)$, γ is written as

$$\gamma = \frac{\pi^2}{3}k_{\mathrm{B}}^2 D(E_{\mathrm{F}}). \tag{3.37}$$

In the spherical Fermi surface, γ can be written as

$$\gamma = \frac{\pi^2}{3} k_{\mathrm{B}}^2 \cdot \frac{V}{2\pi^2} \left(\frac{2m_{\mathrm{c}i}^*}{\hbar^2} \right)^{3/2} E_{\mathrm{F}}^{1/2}$$
$$= \frac{k_{\mathrm{B}} V}{3\hbar^2} \cdot m_{\mathrm{c}}^* \cdot k_{\mathrm{F}}, \tag{3.38}$$

where V is molar volume and $k_{\mathrm{F}} = (S/\pi)^{1/2}$, then

$$\gamma = \frac{k_{\mathrm{B}}^2 m_0}{3\hbar^2} \left(\frac{2e}{\hbar c} \right)^{1/2} \cdot \frac{m_{\mathrm{c}}^*}{m_0} F^{1/2} \tag{3.39}$$
$$= 2.87 \times 10^{-6} [\mathrm{mJ/K^2 mol} \cdot (\mathrm{cm^3/mol}) \cdot \mathrm{Oe}] \cdot V \frac{m_{\mathrm{c}}^*}{m_0} F^{1/2}$$

In the case of the cylindrical Fermi surface,

$$\gamma = \frac{\pi^2}{3} k_{\mathrm{B}}^2 \frac{V}{2\pi^2\hbar^2} m_c^* k_z \tag{3.40}$$
$$= \frac{k_{\mathrm{B}}^2 V}{6\hbar^2} m_c^* k_z, \tag{3.41}$$

where the Fermi wave number k_z is parallel to an axial direction of the cylinder. If we regard simply the Fermi surfaces as sphere, ellipsoid or cylinder approximately and then we can calculate them.

Dingle temperature

The Dingle temperature T_{D} is estimated by measuring field dependence of a dHvA amplitude;

$$\ln \left\{ A_i H^{1/2} \left[1 - \exp \left(\frac{-2\lambda m_{\mathrm{c}i}^* T}{H} \right) \right] \right\} = -\lambda m_{\mathrm{c}i}^* (T + T_{\mathrm{D}}) \cdot \frac{1}{H} + const. \tag{3.42}$$

From the slope of a $\ln \left\{ A_i H^{1/2} \left[1 - \exp \left(\frac{-2\lambda m_{\mathrm{c}i}^* T}{H} \right) \right] \right\}$ plot versus $1/H$ at a constant T, the Dingle temperature can be obtained. Here, the cyclotron effective mass must have already been obtained.

We can estimate the mean free path l or the scattering lifetime τ from the Dingle temperature. The relation between an effective mass and lifetime takes the form

$$\hbar k_{\mathrm{F}} = m_{\mathrm{c}}^* v_{\mathrm{F}}, \tag{3.43}$$
$$l = v_{\mathrm{F}} \tau. \tag{3.44}$$

Then eq. (3.35) is transformed into

$$l = \frac{\hbar^2 k_{\mathrm{F}}}{2\pi k_{\mathrm{B}} m_{\mathrm{c}}^* T_{\mathrm{D}}} \tag{3.45}$$

When the extremal area is approximated as a circle approximately, using eq. (3.45), the mean free path is expressed as

$$\begin{aligned} l &= \frac{\hbar^2}{2\pi k_{\mathrm{B}} m_0} \left(\frac{2e}{\hbar c}\right) \cdot F^{1/2} \left(\frac{m_{\mathrm{c}}^*}{m_0}\right)^{-1} T_{\mathrm{D}}^{-1} \\ &= 0.776\ [\text{Å} \cdot \text{Oe}^{-1/2} \cdot \text{K}] \cdot F^{1/2} \left(\frac{m_{\mathrm{c}}^*}{m_0}\right) T_{\mathrm{D}}^{-1} \end{aligned} \tag{3.46}$$

The magnetic torque measurement was carried out using the membrane-type surface stress sensor (MSS) chip (Nano World, SD-MSS) [103]. In this torque measurement method, a piezoresistive MSS chip was used, as shown in Fig 3.22(a). The measurement technique is similar to torque magnetometry using a piezoresistive microcantilever [104, 105, 106].

A Wheatstone bridge was constructed to detect the quantum oscillations, as shown in Fig 3.22(c). A part of on-chip interconnections was disconnected and two middle wires were short-circuited to cancel out the magnetoresistance of the piezo element, as shown in Fig. 3.22(b). In the modified circuit, only the piezo elements R_1 and R_2 are active. R_1 and R_2 are connected to the external resistor (500 Ω) and the variable resistor to form the Wheatstone Bridge, as shown in Fig 3.22(c). In zero field, the bridge is balanced using the variable resistor. The output voltage ΔV_{out} of Wheatstone bride can be described as:

$$\Delta V_{\mathrm{out}} \propto (\Delta R_2 - \Delta R_1) I. \tag{3.47}$$

When a magnetic torque is applied to the sample plate, the strain applied to the piezo elements R_1 and R_2 are in opposite directions. Therefore, the output voltage is increased as in eq. 3.47.

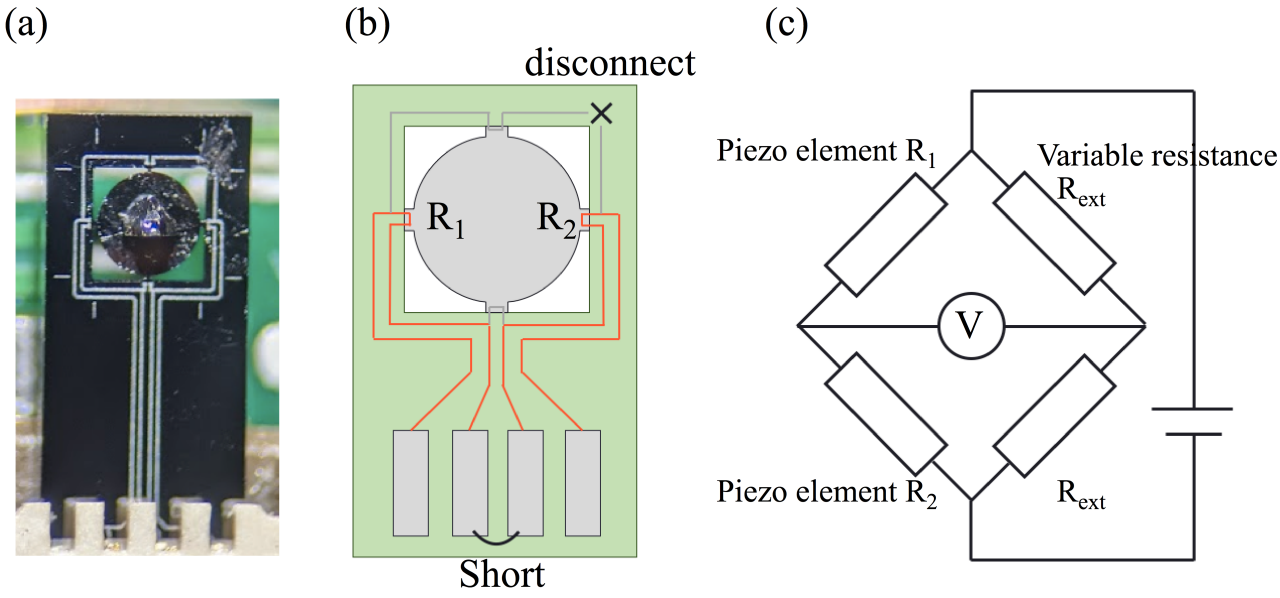

Figure 3.22: Picture of the membrane-type surface stress (MSS) sensor. (b) Schematic view of the MSS sensor. (c) Schematic diagram of the Wheatstone bridge circuit.

The output voltage was measured using a Lock-in amplifier (SR-830, Stanford Research Systems). The angular dependence of magnetic torque was measured using the TeslatronPT (Oxford Instruments) with the rotator probe (Niki Glass).

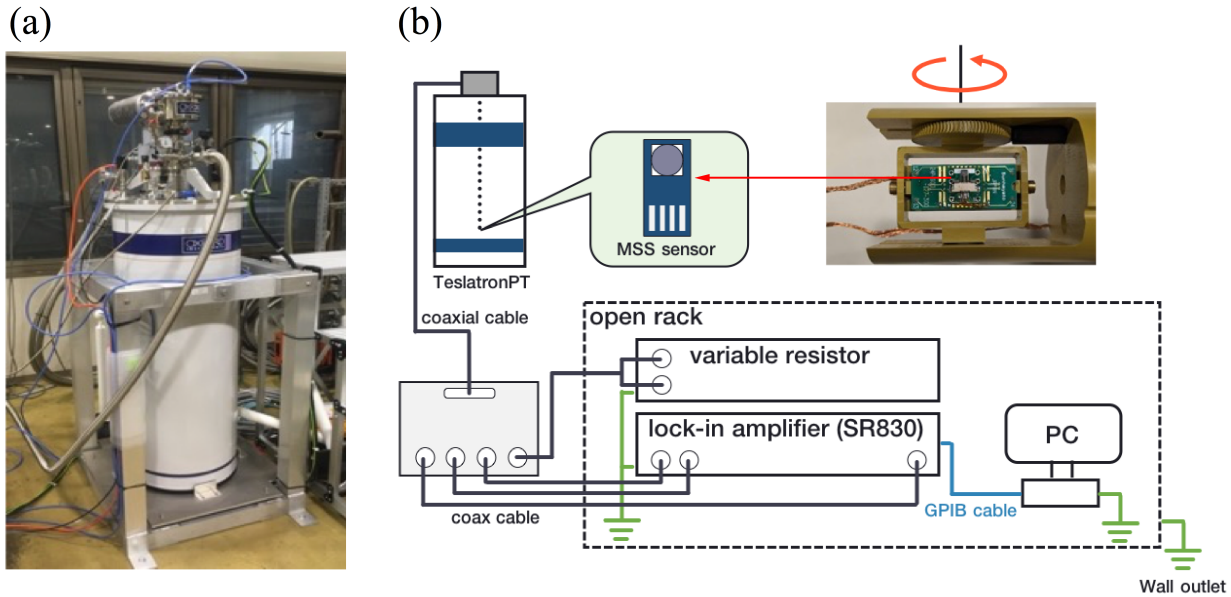

Figure 3.23: (a) Picture of TeslatronPT. (b) Schematic diagram of the circuit for dHvA measurements.

CHAPTER 4

Experimental Results and Discussion

We present the experimental results of electrical resistivity, specific heat, magnetoresistance, and de Haas-van Alphen (dHvA) effect for α-$IrSn_4$, α-$RhSn_4$, $IrGe_4$, and $RhGe_4$, together with the results of energy band calculations.

4.1 Electrical resistivity

Figures 4.1(a), 4.1(b), 4.1(c), and 4.1(d) show the temperature dependences of electrical resistivities ρ in α-$IrSn_4$, α-$RhSn_4$, $IrGe_4$, and $RhGe_4$ for the current J along the [0001] and [11$\bar{2}$0] directions, respectively. The resistivities show slight convex features in their temperature dependences, namely, $d^2\rho/dT^2 < 0$, which suggests a contribution of Rh-4d and Ir-5d electrons to conduction electrons. The residual resistivities ρ_0 are very small in α-$IrSn_4$, α-$RhSn_4$, and $IrGe_4$, indicating high-quality single crystals. The residual resistivity and residual resistivity ratio RRR (= ρ_{RT}/ρ_0) are $\rho_0 = 0.052\ \mu\Omega\cdot$cm and RRR = 1250 for $J \parallel [0001]$ and $\rho_0 = 0.192\ \mu\Omega\cdot$cm and RRR = 867 for $J \parallel [11\bar{2}0]$ in α-$IrSn_4$; $\rho_0 = 0.098\ \mu\Omega\cdot$cm and RRR = 430 for $J \parallel [0001]$ and $\rho_0 = 0.115\ \mu\Omega\cdot$cm and RRR = 540 for $J \parallel [11\bar{2}0]$ in α-$RhSn_4$; $\rho_0 = 0.76\ \mu\Omega\cdot$cm and RRR = 90 for $J \parallel [0001]$ and $\rho_0 = 2.49\ \mu\Omega\cdot$cm and RRR = 90 for $J \parallel [11\bar{2}0]$ in $IrGe_4$; and $\rho_0 = 13.7\ \mu\Omega\cdot$cm and RRR = 8.5 in $RhGe_4$. Note that the previous single crystal of α-$IrSn_4$ was grown by the usual flux method, revealing $\rho_0 = 0.1\ \mu\Omega\cdot$cm and RRR = 628. The present single crystal shown in Fig. 4.1(a) was grown by the modified flux method in a horizontal furnace, with extremely high quality. As shown in insets of 4.1(c) and 4.1(d), superconductivity was observed at 1.12 K in $IrGe_4$ and 2.28 K in $RhGe_4$.

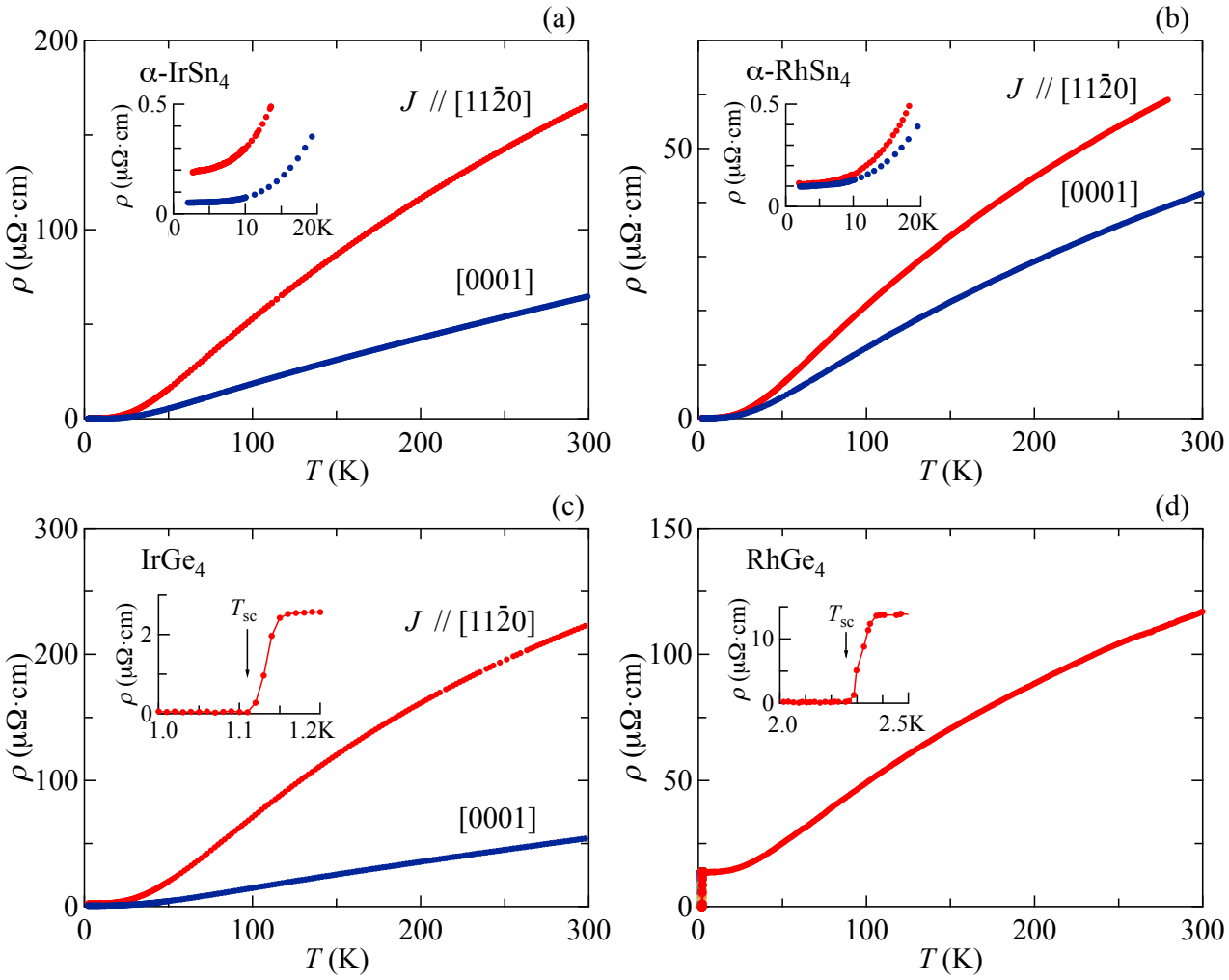

Figure 4.1: Temperature dependences of electrical resistivities in (a) α-$IrSn_4$, (b) α-$RhSn_4$, (c) $IrGe_4$, and (d) $RhGe_4$.

We noticed similar anisotropy of the resistivities in these compounds. The resistivities for $J \parallel [11\bar{2}0]$ are larger than those for $J \parallel [0001]$ in magnitude. If a Fermi surface is spherical as expressed in $\varepsilon_F = (\hbar^2/2m^*)\boldsymbol{k}_F^2 = (\hbar^2/2m^*)(k_x^2 + k_y^2 + k_z^2)$, there exists no anisotropy in the electrical resistivity ρ, where ε_F is the Fermi energy and $\boldsymbol{k}_F = (k_x, k_y, k_z)$ is the Fermi wave vector of conduction electrons. If a Fermi surface is cylindrical as in $\varepsilon_F = (\hbar^2/2m^*)(k_x^2 + k_y^2)$, the resistivity along the cylindrical axis is infinite in magnitude, although the resistivity perpendicular to the cylindrical axis is finite, revealing a two-dimensional electronic state. If instead, the conduction electrons can move only along the z-axis [$\varepsilon_F = (\hbar^2/2m^*)k_z^2$], the topology of the Fermi surface can be changed into two plates. A flat ellipsoid of revolution might correspond to a simple

Fermi surface in the present compounds, where the plate Fermi surface is expanded along the z-axis. The Fermi surface and effective mass are further discussed later.

4.2 Specific heat

We measured the low-temperature specific heat C of α-$IrSn_4$, α-$RhSn_4$, $IrGe_4$, and $RhGe_4$, as shown in Figs. 4.2(a), 4.2(b), 4.2(c), and 4.2(d), respectively. The specific heat consists of electronic and lattice contributions: $C = C_{\rm el} + C_{\rm ph} = \gamma T + \beta T^3$, where γ is the electronic specific heat coefficient and β is related to the Debye temperature $\theta_{\rm D}$. Figures 4.2(a)-4.2(d) represent the C/T vs T^2 plot. The γ and $\theta_{\rm D}$ values were obtained from these plots as 3.46 mJ/(K^2·mol) and 255 K in α-$IrSn_4$, 5.50 mJ/(K^2·mol) and 270 K in α-$RhSn_4$, 3.93 mJ/(K^2· mol) and 362 K in $IrGe_4$, and 4.16 mJ/(K^2·mol) and 340 K in $RhGe_4$.

As shown in Figs. 4.2(c) and 4.2(d), superconductivity was observed at 1.12 K in $IrGe_4$ and 2.55 K in $RhGe_4$. The specific heat jump was $\Delta C/\gamma T_{\rm sc} = 1.23$ in $IrGe_4$ and $\Delta C/\gamma T_{\rm sc} = 1.44$ in $RhGe_4$, which are close to the weak-coupling BCS value of 1.43.

Figures 4.2(d) and 4.2(f) represent the temperature dependences of electronic specific heats in the form of $C_{\rm el}/T$ in $IrGe_4$ and $RhGe_4$, respectively. Solid lines, which fit to the experimental data by adjusting superconducting energy gaps Δ in the BCS theory, represent $2\Delta = 3.70$ K in $IrGe_4$ and $2\Delta = 8.93$ K in $RhGe_4$ [107, 108].

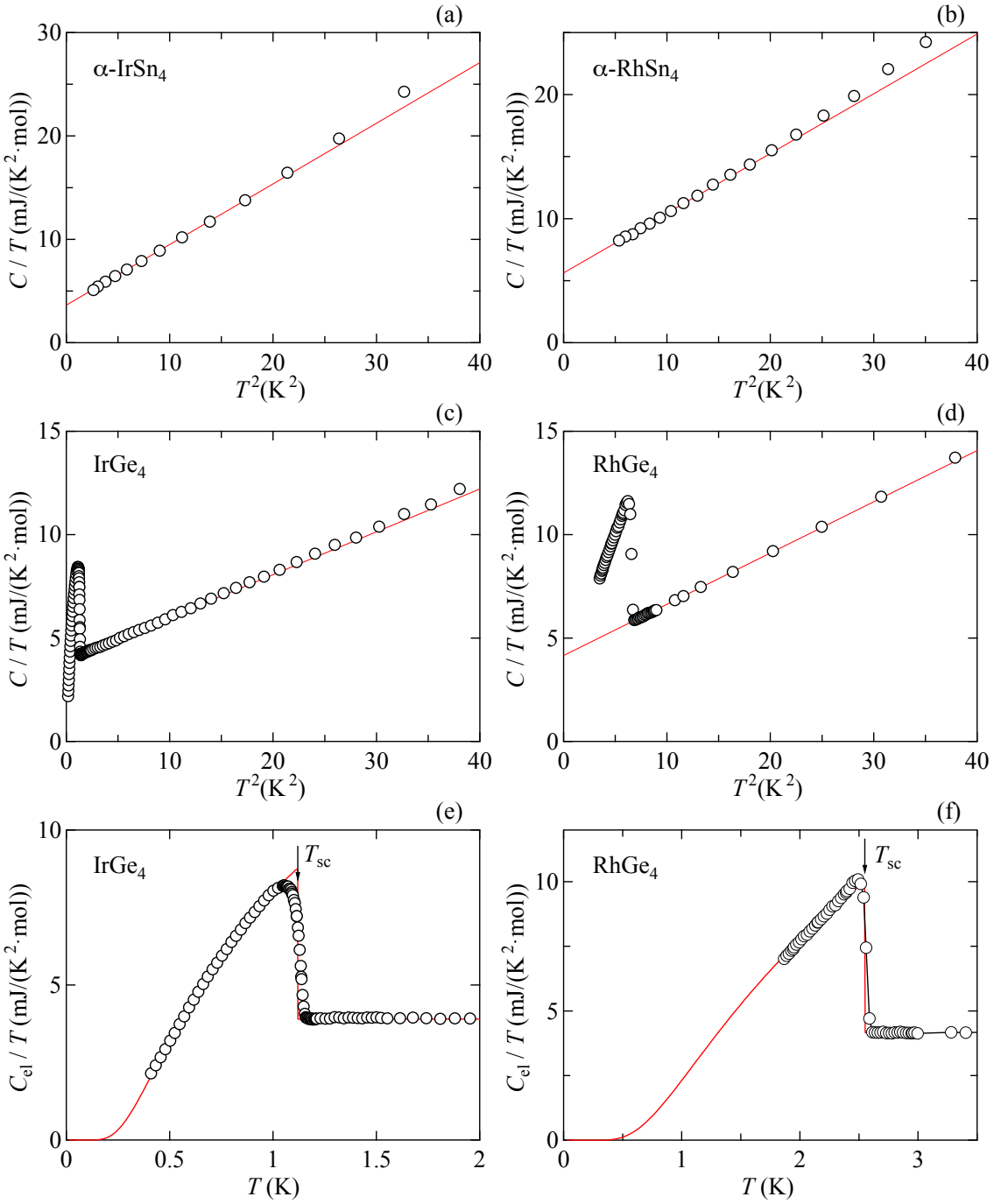

Figure 4.2: T^2-dependences of the specific heats C in the form of C/T in (a) α-$IrSn_4$, (b) α-$RhSn_4$, (c) $IrGe_4$, and (d) $RhGe_4$, together with the temperature dependences of electronic specific heats in the form of C_{el}/T in (e) $IrGe_4$ and (f) $RhGe_4$, where T_{sc} is the superconducting transition temperature.

Next, we measured the specific heats under several magnetic fields to obtain the upper critical field $\mu_0 H_{c2}$ in $IrGe_4$ and $RhGe_4$, as shown in Figs. 4.3(a)-6(d) and Figs. 6(e) and 6(f), respectively. Superconducting transition temperatures under magnetic fields for $H \parallel [11\bar{2}0]$ in $IrGe_4$, for example, are defined by arrows, as shown in Fig. 6(a). Thus, the obtained data were used in the temperature dependence of $\mu_0 H_{c2}$, as shown in Figs. 6(d) and 6(f). Solid lines connecting the data in Figs. 4.3(d) and 6(f) are based on the so-called WHH theory [36, 37]. The upper critical field $\mu_0 H_{c2}$ at 0 K is small in value,: $\mu_0 H_{c2}(0) = 11.5$ mT for $H \parallel [11\bar{2}0]$ and $[10\bar{1}0]$ or $\mu_0 H_{c2}$ $(H \perp c) = 11.5$ mT and $\mu_0 H_{c2}$ $(H \parallel c) = 25.5$ mT in $IrGe_4$, and $\mu_0 H_{c2}(0) = 72.5$ mT in $RhGe_4$.

Anisotropy of $\mu_0 H_{c2}(H \parallel c)$ and $\mu_0 H_{c2}(H \perp c)$ in $IrGe_4$ is simply explained on the basis of the effective mass model because of $\mu_0 H_{c2}(0) = \phi_0/2\pi\xi^2$ and $\xi^{-1} \sim \sqrt{m^*}$, where ϕ_0 is the fluxoid or flux quantum and ξ is the coherence length [109]. We assumed an ellipsoidal Fermi surface of revolution as in

$$\varepsilon_F = \frac{\hbar^2 k_x^2}{2m_a^*} + \frac{\hbar^2 k_y^2}{2m_a^*} + \frac{\hbar^2 k_z^2}{2m_c^*}. \tag{4.1}$$

$\mu_0 H_{c2}(H \parallel c) \sim m_a^*$ and $\mu_0 H_{c2}(H \perp c) \sim \sqrt{m_a^* m_c^*}$ are obtained from relations of $dS/d\varepsilon = 2\pi m_a^*/\hbar^2$ for $H \parallel c$ and $dS/d\varepsilon = 2\pi\sqrt{m_a^* m_c^*}/\hbar^2$ for $H \perp c$, where S correspond to the cross-sectional area of the Fermi surface, namely, S_F $(H \parallel c) = \pi k_a^2 = (2\pi\varepsilon_F/\hbar^2) m_a^* \sim \mu_0 H_{c2}(H \parallel c)$ and S_F $(H \perp c) = \pi k_a k_c = (2\pi\varepsilon_F/\hbar^2)\sqrt{m_a^* m_c^*} \sim \mu_0 H_{c2}(H \perp c)$ were obtained, representing relations of $k_a : k_c = \sqrt{\mu_0 H_{c2}(H \parallel c)} : \mu_0 H_{c2}(H \perp c)/\sqrt{\mu_0 H_{c2}(H \parallel c)}$ $\simeq 9 : 4$ or $m_a^* : m_c^* = \mu_0 H_{c2}(H \parallel c) : \mu_0 H_{c2}(H \perp c)^2/\mu_0 H_{c2}(H \parallel c) = 9^2 : 4^2$. From these relations, the flat ellipsoidal Fermi surface of revolution was obtained as shown in the inset of Fig. 4.3(d). Table 4.1 summarizes the superconducting properties obtained from the specific heat experiments for $IrGe_4$ and $RhGe_4$. The present Fermi surface is consistent with the anisotropy of electrical resistivities mentioned above.

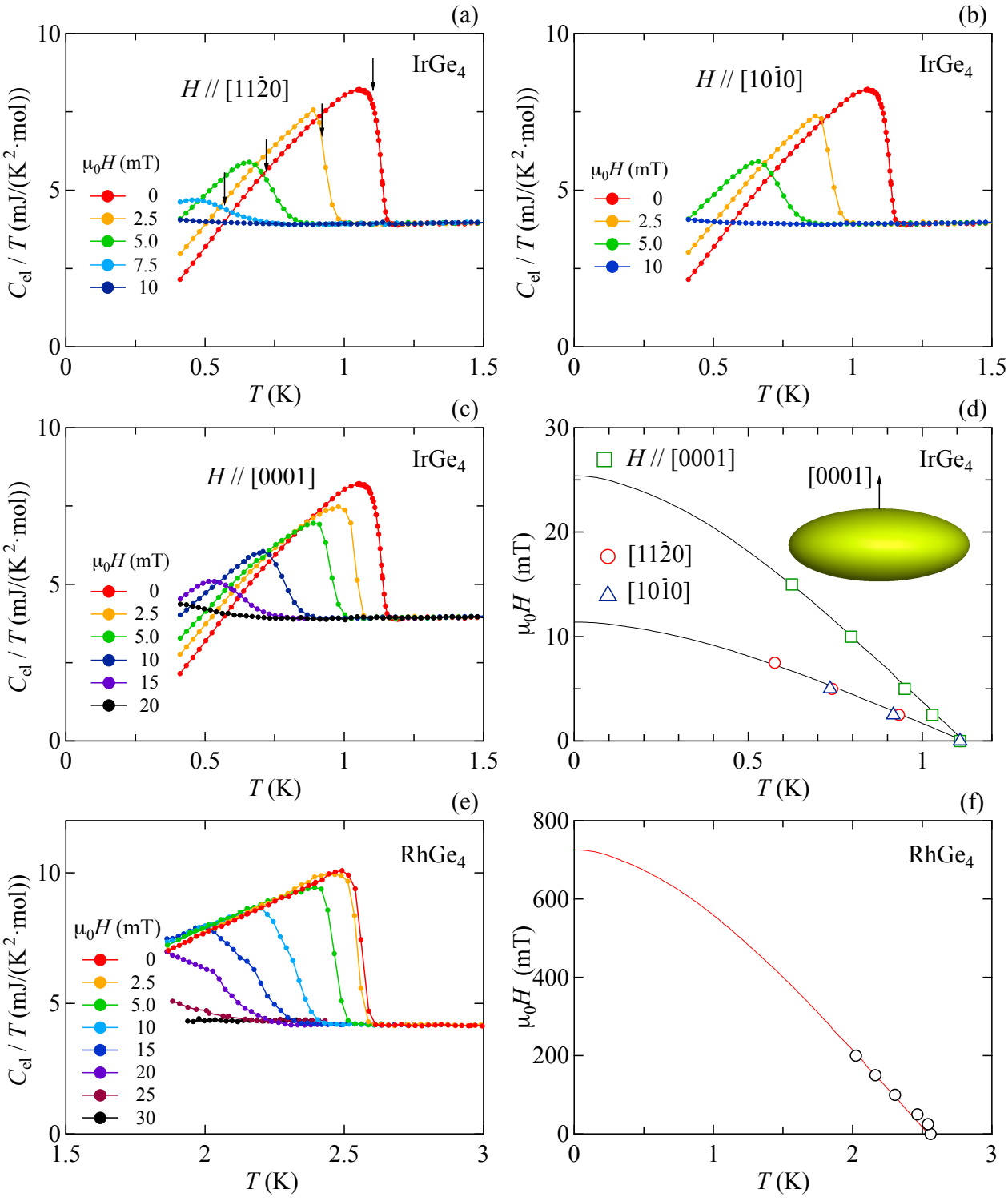

Figure 4.3: Temperature dependences of (a)-(c) electronic specific heats in the form of C_{el}/T under several magnetic fields and the upper critical fields H_{c2} in (d) $IrGe_4$, and (e)-(f) in $RhGe_4$, where a flat ellipsoidal Fermi surface is obtained on the basis of the effective mass model for H_{c2} in superconductivity, as shown in the inset of (d).

Table 4.1: Superconducting properties of $IrGe_4$ and $RhGe_4$, where c corresponds to the c-axis or [0001] direction.

parameters	$IrGe_4$	$RhGe_4$.
T_{sc} (K)	1.22	2.55
γ (mJ/K^2-mol)	3.93	4.16
$\mu_0 H_{c2}$ (mT)	25.5 ($H \parallel c$)	72.5
	11.5 ($H \perp c$)	
ξ (Å)	2540 ($H \parallel c$)	367
	1140 ($H \perp c$)	
$\Delta C/\gamma T_{sc}$	1.23	1.44
2Δ(K)	3.70	8.93

4.3 Magnetoresistance

We measured the transverse magnetoresistances in the configuration of $J \perp H$, where J is along the [11$\bar{2}$0] and [0001] directions, together with the longitudinal magnetoresistances for $J \parallel H \parallel$ [0001] and $J \parallel H \parallel$ [11$\bar{2}$0], as shown in Fig. 4.4. Note that the directions in this trigonal structure are later shown in Fig. 4.13(b).

In Fig. 4.4(a), the transverse magnetoresistance $\rho(H)/\rho(0) = \{\rho(H) - \rho(H = 0)\}/\rho(H = 0)$ in α-$IrSn_4$ is extremely large in magnitude for $J \parallel$ [11$\bar{2}$0] and $H \parallel$ [$\bar{1}$100] and increases for as H^n ($n \simeq 1.6$) above 6 T, indicating that open orbits exist along $J \times H$, namely the [0001] direction. This is because α-$IrSn_4$ is an uncompensated metal. Valence electrons are $5d^9$ in the Ir atom and $5s^2 5p^2$ in the Sn atom, and the primitive cell contains three molecules of α-$IrSn_4$ (Z = 3), as shown in Table 3.2(a), representing 75 valence electrons in total.

For a given field direction, when all of the cyclotron orbits are closed, the transverse magnetoresistance saturates ($\Delta\rho/\rho \sim H^0$) for the uncompensated metal. If the transverse magnetoresistance increases as $H^n (1 < n \leq 2)$ for a particular field direction, often a symmetrical direction, some open orbits exist with the direction parallel to $J \times H$. In the present configuration of $J \parallel$ [11$\bar{2}$0] and $H \parallel$ [$\bar{1}$100] for α-$IrSn_4$, open orbits should exist along [0001]. Similar magnetoresistances are observed in Fig. 4.4(b) for α-$RhSn_4$, and in Fig. 4.4(c) for $IrGe_4$.

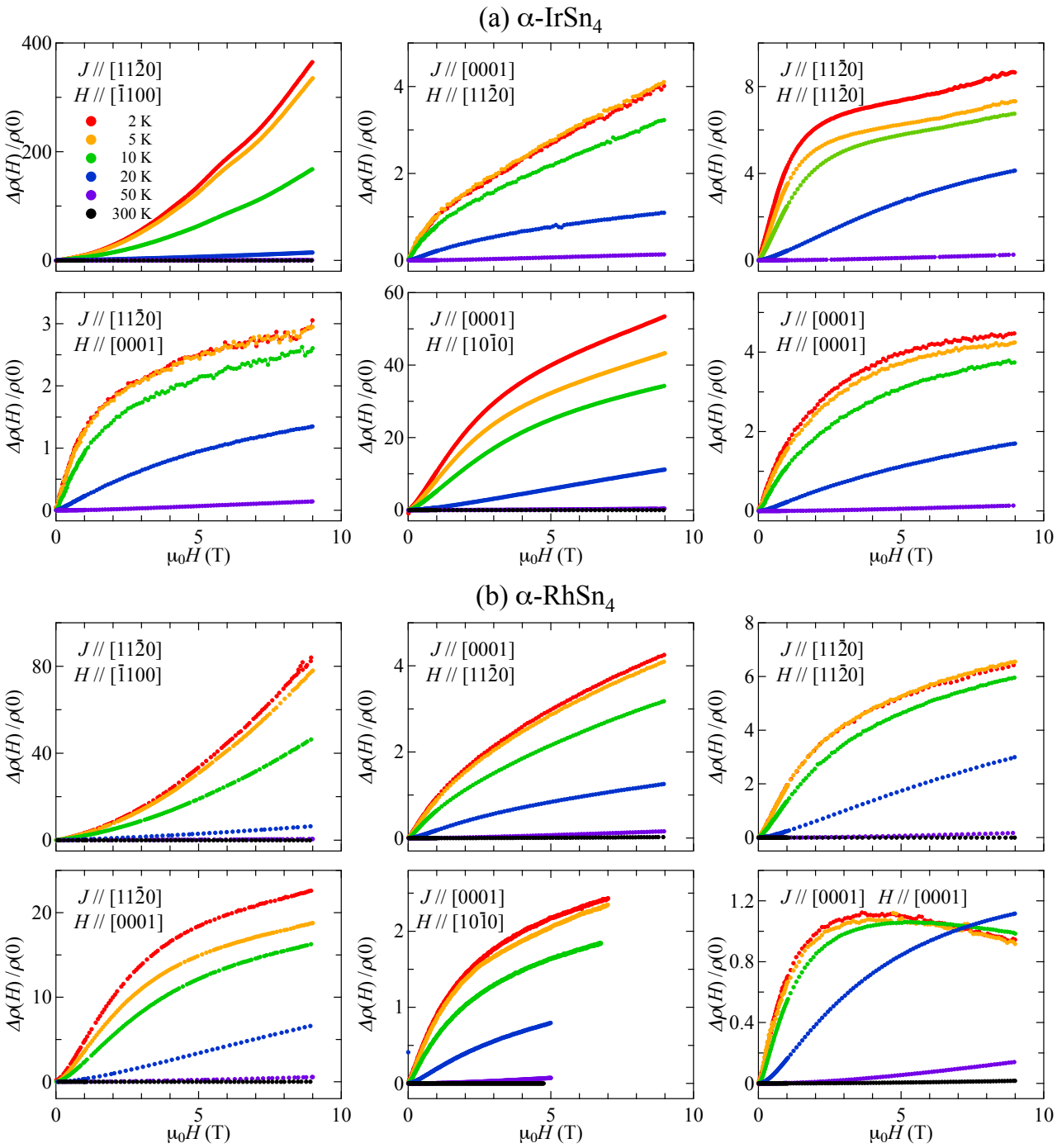
(a) α-IrSn4
J // [11-20]
H // [-1100]
2 K
5 K
10 K
20 K
50 K
300 K
J // [11-20]
H // [0001]
J // [0001]
H // [11-20]
J // [11-20]
H // [11-20]
J // [0001]
H // [10-10]
J // [0001]
H // [0001]
Δρ(H)/ρ(0)
μ0H (T)
(b) α-RhSn4
J // [11-20]
H // [-1100]
J // [11-20]
H // [0001]
J // [0001]
H // [11-20]
J // [11-20]
H // [11-20]
J // [0001]
H // [10-10]
J // [0001] H // [0001]

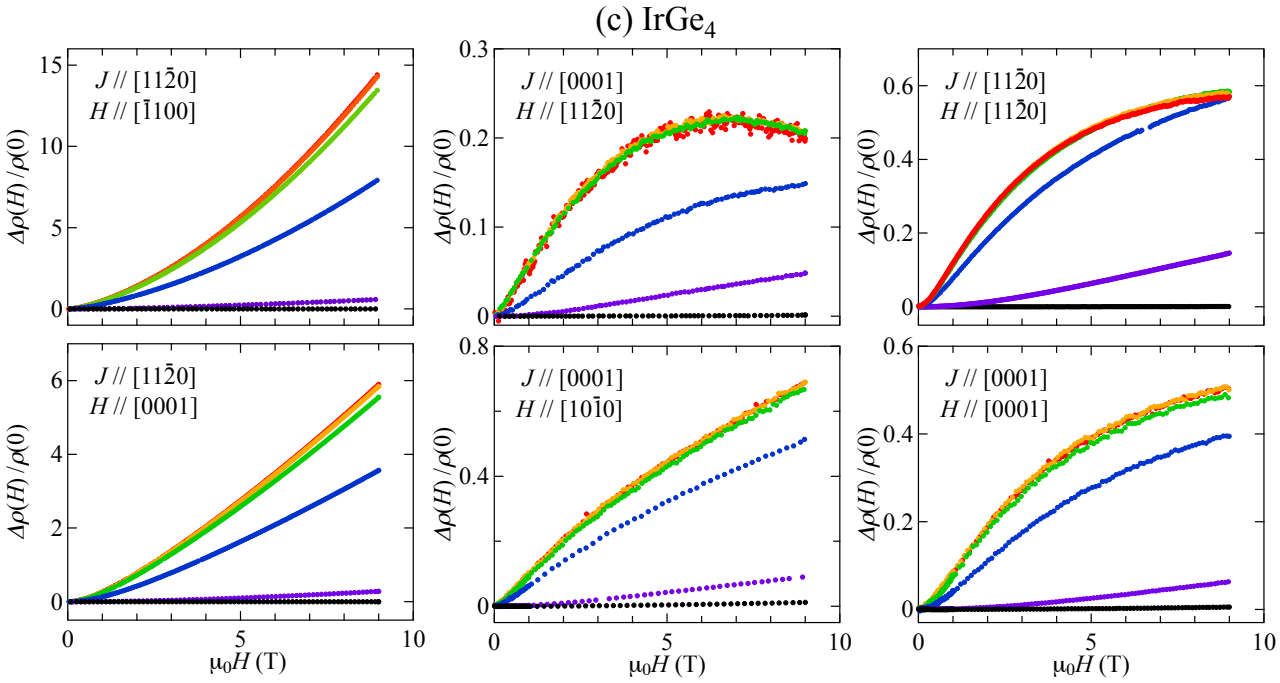

Figure 4.4: Transverse and longitudinal magnetoresistances in (a) α-$IrSn_4$, (b) α-$RhSn_4$, and (c) $IrGe_4$, where the temperature is shown by color in the first figure in α-$IrSn_4$.

For the longitudinal magnetoresistances in the configurations of $J \parallel H \parallel [11\bar{2}0]$ and $J \parallel H \parallel [0001]$, the magnetoresistances are small in magnitude compared with the transverse magnetoresistances. If the Fermi surface is spherical, the longitudinal magnetoresistances should be zero. The present magnetoresistances are mainly due to a non-spherical and multiply-connected Fermi surface, which are described next.

Temperature dependences of magnetoresistances under the magnetic field $\mu_0 H = 9$ T are studied for these compounds, as shown in Fig. 4.5. The vertical axis corresponds to the logarithmic scale of the magnetoresistances. An extremely large change of the electrical resistivity in the magnetic field of 9 T is observed in the high-quality sample of α-$IrSn_4$, reflecting the open orbits along the [0001] direction. Open orbits are observed not only for [0001] but also another direction. This is reflected in the angular dependences of transverse magnetoresistances in Fig. 4.6.

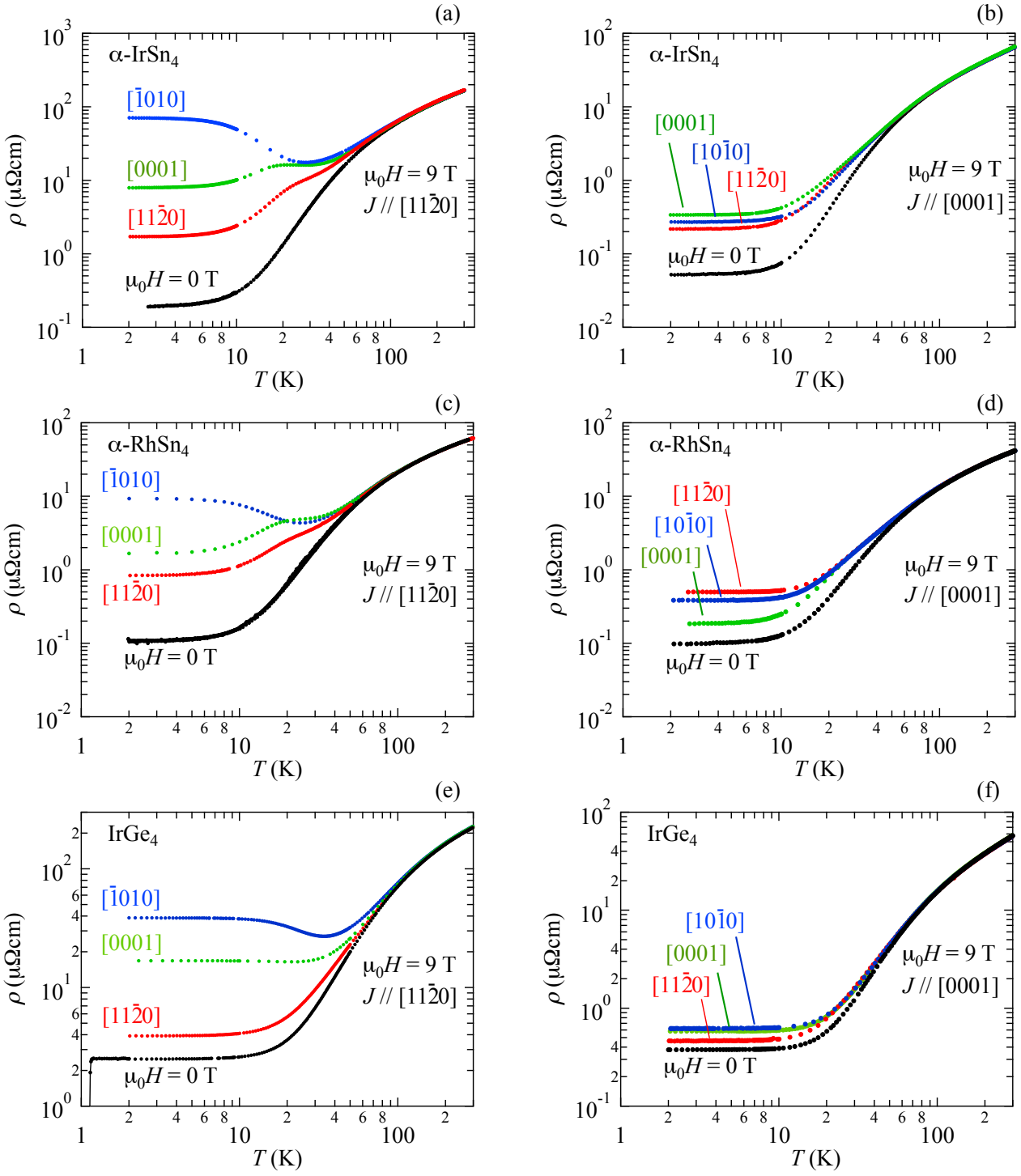

Figure 4.5: Temperature dependences of electrical resistivities in 9 T for (a) and (b) α-$IrSn_4$, (c) and (d) α-$RhSn_4$, and (e) and (f) $IrGe_4$, together with those in 0 T.

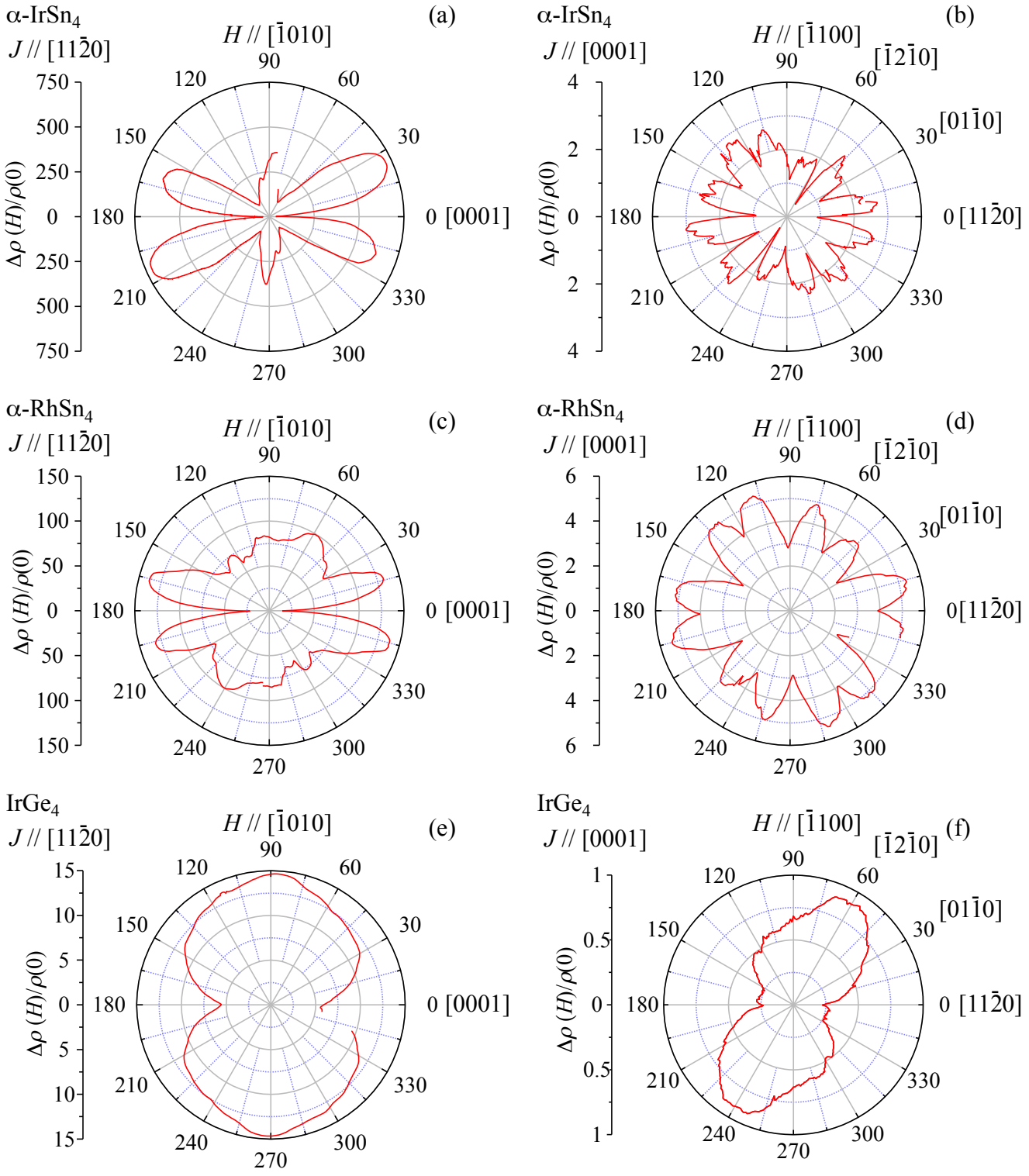

Figure 4.6: Angular dependences of electrical resistivities at 2 K under 9 T (a) and (b) α-$IrSn_4$, (c) and (d) α-$RhSn_4$, and (e) and (f) $IrGe_4$.

4.4 de Haas-van Alphen effect

A main Fermi surface is a flat ellipsoidal Fermi surface from the results of the upper critical field H_{c2} in $IrGe_4$, as mentioned above. However, the Fermi surface is multiply-connected with open orbits, at least along the [0001] direction, from the results of magnetoresistances. To clarify the Fermi surface properties, we carried out the de Haas-van Alphen (dHvA) experiments for α-$IrSn_4$, α-$RhSn_4$, and $IrGe_4$.

Figure 4.7 shows the typical dHvA oscillations and corresponding fast Fourier transformation (FFT) spectrum for $H \parallel [0001]$ in α-$IrSn_4$. The dHvA frequency F ($= c\hbar S_{\mathrm{F}}/2\pi e$), which is proportional to the maximum or minimum cross-sectional area S_{F} of the Fermi surface, is expressed as a unit of magnetic field $\mu_0 H$. The dHvA frequency F ranges from 0.049 kT to 0.432 kT, which are very small in value. The corresponding Fermi surfaces are very small in cross-sectional area. Typical dHvA branches are named $\varepsilon, \varepsilon', \zeta, \zeta'$, together with their harmonics. We also show in Fig. 4.8 the dHvA oscillations and the corresponding FFT spectrum for the field direction of $\theta = 9°$, where $\theta = 9°$ means that the direction of the magnetic field is close to $[11\bar{2}0]$ but is tilted by 9° from $[11\bar{2}0]$ to $[01\bar{1}0]$ in the basal plane. Relatively large dHvA branches named α (3.693 kT) and α'(3.901 kT), together with branches γ and δ, were observed. Figures 4.9 and 4.10 show the typical dHvA oscillations and corresponding FFT spectra for $H \parallel [11\bar{2}0]$ in α-$RhSn_4$ and for $H \parallel [0001]$ in $IrGe_4$, respectively.

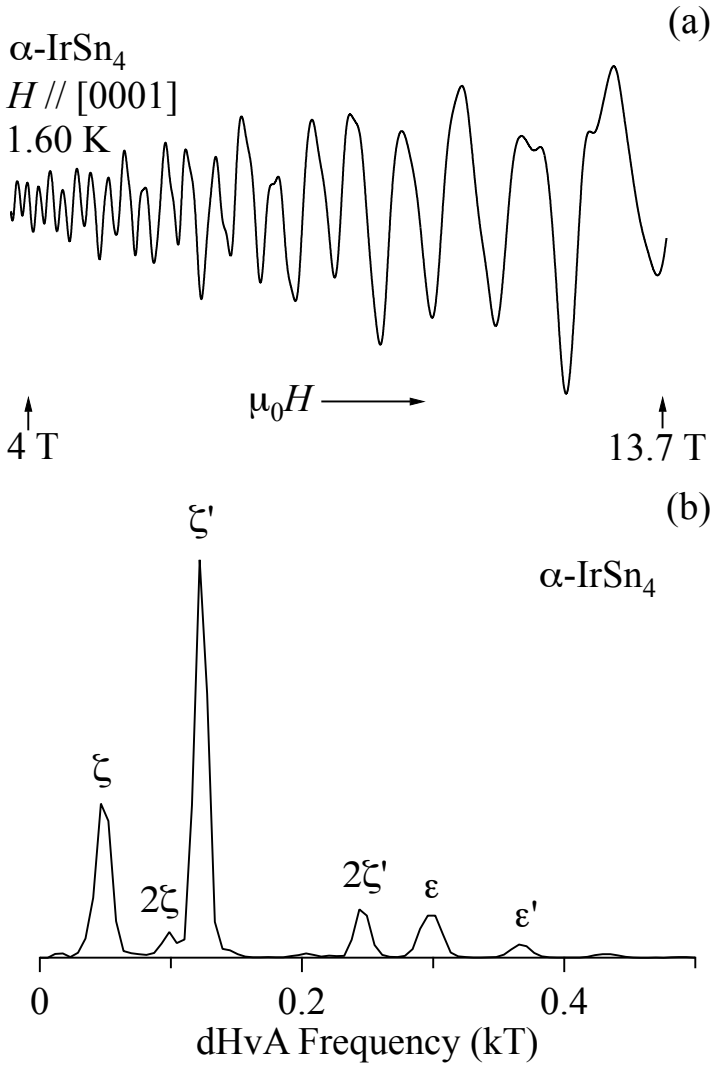

Figure 4.7: Typical dHvA oscillations and the corresponding FFT spectrum for $H \parallel [0001]$ in α-$IrSn_4$.

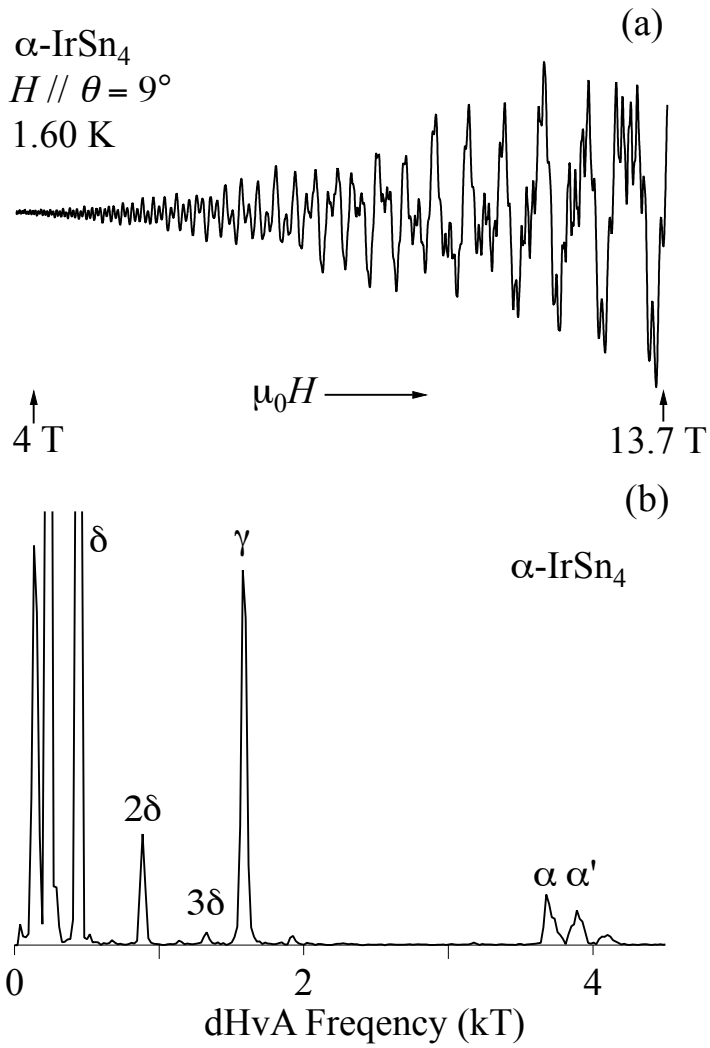

Figure 4.8: Typical dHvA oscillations and the corresponding FFT spectrum for the field direction of $\theta = 9°$, where $\theta = 9°$ means that the direction of the magnetic field is close to $[11\bar{2}0]$ but is tilted by 9° from $[11\bar{2}0]$ to $[01\bar{1}0]$ in the basal plane.

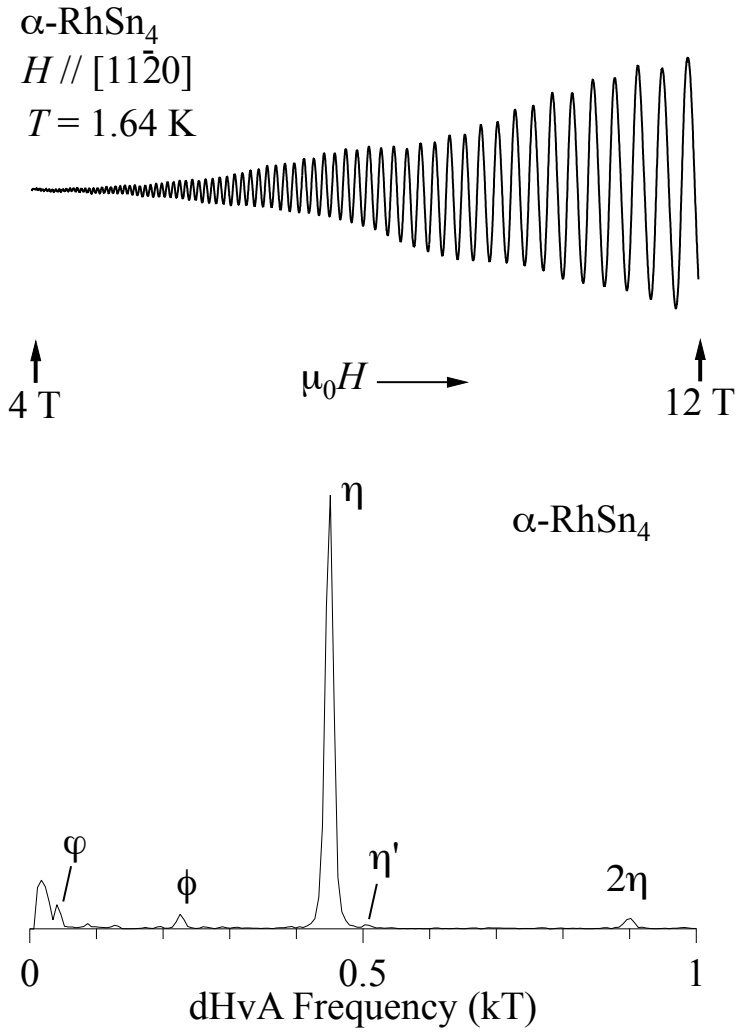

Figure 4.9: Typical dHvA oscillations and the corresponding FFT spectrum for $H \parallel [11\bar{2}0]$ in $RhSn_4$.

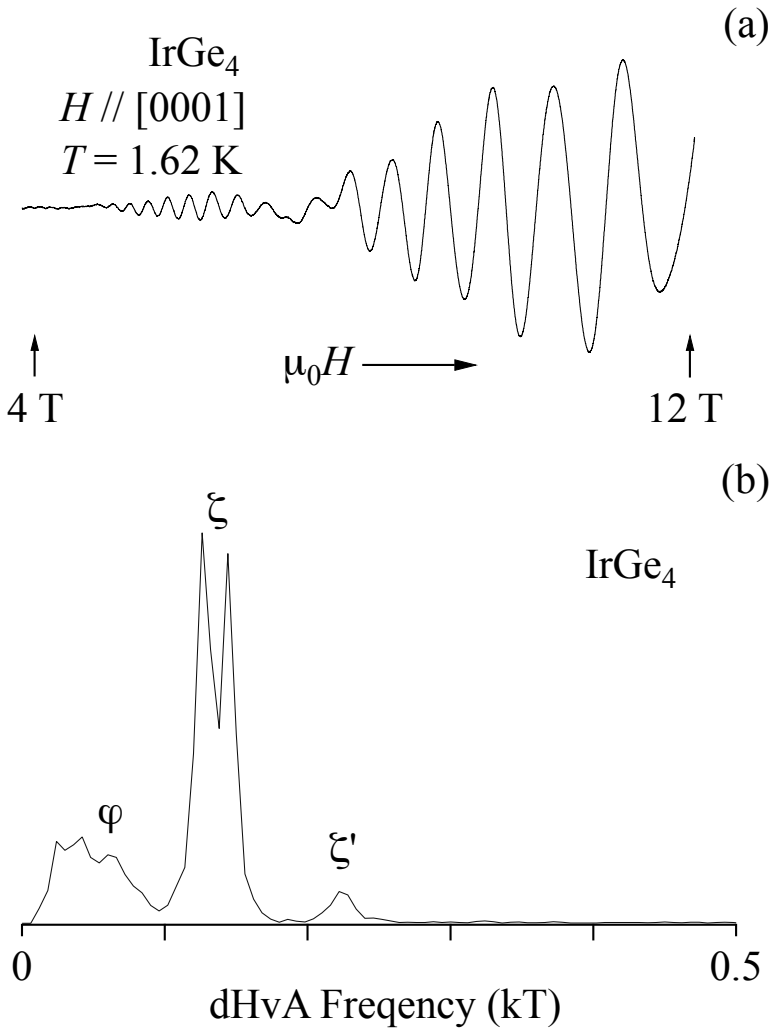

Figure 4.10: Typical dHvA oscillations and the corresponding FFT spectrum for $H \parallel [0001]$ in $IrGe_4$.

We determined the cyclotron effective mass m_c^* from the temperature dependence of dHvA amplitude for α-$IrSn_4$. The cyclotron masses are in the range from 0.36 to 1.55 m_0 (m_0 : rest mass of an electron), which are summarized in Table 4.2(a) for typical three directions.

We measured the angular dependences of dHvA frequencies by rotating the sample, as shown in Fig. 4.11. In Figs. 4.11(a) and 10(b), the magnetic field is directed from [0001] to [11$\bar{2}$0] and furthermore to [000$\bar{1}$]. All the dHvA branches are symmetric for $H \parallel [11\bar{2}0]$ in the angular dependences of dHvA frequencies. The dHvA frequencies are, however, asymmetric in the angular range from [0001] to [10$\bar{1}$0] and furthermore to [000$\bar{1}$], as shown in Fig. 4.11(c). This is based on the present trigonal system with the point group of 321. "3" in 321 indicates three-fold symmetry for the [0001] direction, "2" indicates two-fold symmetry for the [11$\bar{2}$0] direction, and "1" indicates no symmetry for the [10$\bar{1}$0] direction. The present point group symmetry is reflected in the angular dependences of dHvA frequencies. In the basal plane, the angular dependences of dHvA frequencies are symmetric for $H \parallel [01\bar{1}0]$, as shown in Fig. 4.11(d).

We noticed that each dHvA branch is split into two branches, for example, α vs α', β vs β', η vs η', ε vs ε', and ζ vs ζ', reflecting the noncentrosymmetric (chiral) structure of α-$IrSn_4$. Namely, the dHvA frequency F is split into two dHvA frequencies F_+ and F_-, depending on the up(+) and down(-) spin states. Using the relations of $m^* = (\hbar^2/2\pi)dS/d\varepsilon$ and $S_F = (2\pi e/c\hbar)F$, we obtain

$$\begin{aligned} \Delta\varepsilon &= \frac{\hbar^2}{2\pi m^*}\Delta S \\ &= \frac{\hbar e}{m^* c}|F_+ - F_-|. \end{aligned} \tag{4.2}$$

Here, $\Delta\varepsilon$ corresponds to the magnitude of the antisymmetric spin-orbit interaction mentioned in section 2.3. In the dHvA experiments, m^* in eq. (4.2) is the average of two cyclotron masses m_c^* for two split dHvA brances. The splitting energy $\Delta\varepsilon$ between two split Fermi surfaces is 190 K for branches α and α' and is 280 K for branches ζ (F = 0.049 kT and $m_c^* = 0.37\ m_0$) and ζ' (0.124 kT and $m_c^* = 0.36\ m_0$), as summarized in Table 4.2(a).

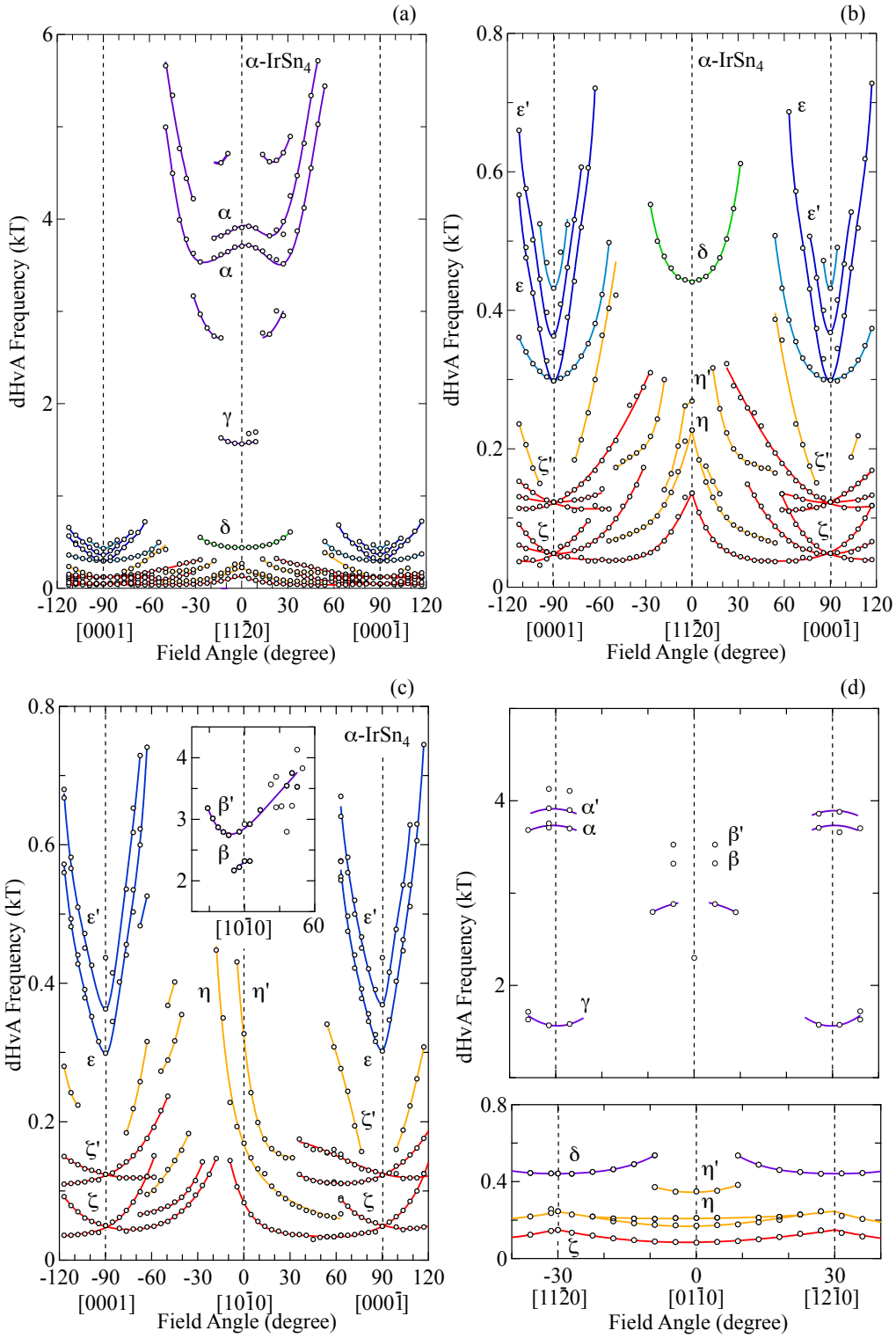

Figure 4.11: Angular dependences of dHvA frequencies of α-$IrSn_4$ in (a) from [0001] to [11$\bar{2}$0] and furthermore to [000$\bar{1}$]. (b) The same angular dependences for small dHvA branches, (c) from [0001] to [10$\bar{1}$0] and furthermore to [000$\bar{1}$], and (d) in the basal plane.

Table 4.2: dHvA frequencies F, cyclotron effective masses m_c^*, and splitting energies $\Delta\varepsilon$ for typical field orientations in α-$IrSn_4$, α-$RhSn_4$, and $IrGe_4$.

(a) α-$IrSn_4$

$H \parallel [0001]$				$H \parallel [10\bar{1}0]$				$\theta = 9°$ tilted from $[11\bar{2}0]$ to $[01\bar{1}0]$			
Branch	F(kT)	m_c^*	$\Delta\varepsilon$(K)	Branch	F(kT)	m_c^*	$\Delta\varepsilon$(K)	Branch	F(kT)	m_c^*	$\Delta\varepsilon$(K)
				β'	2.922	1.1	750	α'	3.901	1.48	190
				β	2.322	1.0		α	3.693	1.39	
								γ	1.588	1.55	
ε'	0.368	0.87	120	η'	0.328	0.77	320	δ	0.444	0.58	
ε	0.302	0.66		η	0.167	0.59		η	0.236	1.00	
ζ'	0.124	0.36	280								
ζ	0.049	0.37		ζ	0.083	0.45		ζ	0.140	0.67	

(b) α-$RhSn_4$

$H \parallel [0001]$				$H \parallel [10\bar{1}0]$				$H \parallel [11\bar{2}0]$			
Branch	F(kT)	m_c^*	$\Delta\varepsilon$(K)	Branch	F(kT)	m_c^*	$\Delta\varepsilon$(K)	Branch	F(kT)	m_c^*	$\Delta\varepsilon$(K)
ε	0.263	0.45		η'	0.424	0.48	220	η'	0.505	0.46	180
				η	0.345	0.43		η	0.449	0.42	
ζ'	0.188	0.27	350								
ζ	0.121	0.24						ϕ	0.226	0.42	
φ	0.067	0.30		φ	0.038	0.18		φ	0.041	0.19	

(c) $IrGe_4$

$H \parallel [0001]$				$H \parallel [10\bar{1}0]$				$H \parallel [11\bar{2}0]$			
Branch	F(kT)	m_c^*	$\Delta\varepsilon$(K)	Branch	F(kT)	m_c^*	$\Delta\varepsilon$(K)	Branch	F(kT)	m_c^*	$\Delta\varepsilon$(K)
ζ'	0.233	0.52	260								
ζ	0.137	0.46									
φ	0.059	0.38		φ	0.056	0.40		φ	0.064	0.37	

We simply considered that the detected dHvA branches are identified as follows:

1. Branches α (α') and most likely β (β') with relatively large dHvA frequencies correspond to main orbits of the flat ellipsoidal Fermi surfaces mentioned above, as shown in Fig 4.12(a). Here, one of two split ellipsoidal Fermi surfaces, namely, branch α is illustrated in Fig. 4.12(a) from the results of the flat ellipsoidal Fermi surface obtained by anisotropic H_{c2} in superconductivity and the dHvA frequency of branch α. Note that the center of the flat ellipsoidal Fermi surface is sited at the A point in the Brillouin zone from the result of the energy band calculations, later shown in Fig 4.13(a). The volume of the corresponding Fermi surface is 2.37×10^{23} cm^{-3}, approximately 33 % of the Brillouin zone in occupation. Here, the volume of the Brillouin zone V_B is $V_B = 7.22 \times 10^{23}$ cm^{-3}. The dHvA branches α and α' are observed in the field angle from $-50°$ to $50°$, having a minimum at $\pm 30°$ in the angular dependences of dHvA frequencies. It is simply suggested that the flat ellipsoidal Fermi surface is slightly corrugated and not closed, but multiply

connected by other Fermi surfaces.

2. Branches ε (ε') are hyperboloidal along the [0001] direction, as shown in Fig. 4.12(b). We considered that the hyperboloidal Fermi surfaces are connected to the ellipsoidal Fermi surface, which favors the open orbits along the [0001] direction. Six hyperboloidal Fermi surfaces occupy approximately 18 % of the Brillouin zone in volume.

3. Branches ζ (ζ') consist of two sets of cylindrical arms, where each set consists of three arms tilted by approximately 40° from the [0001] direction, as shown in Fig. 4.12(c). These six tilted arms and six hyperboloids are most likely connected to the flat ellipsoidal Fermi surfaces, as shown in Fig. 4.12(d). The angular dependences of dHvA frequencies of six tilted arms are shown in Fig. 4.12(e). Six tilted arms occupy approximately 2 % of the Brillouin zone in volume. A half Brillouin zone is roughly occupied by three Fermi surfaces named $\alpha(\alpha'), \varepsilon(\varepsilon')$, and $\zeta(\zeta')$, revealing no other main Fermi surfaces. Open orbits are most likely observed not only for the [0001] direction but also for other field directions.

4. Other dHvA branches such as δ and η are observed.

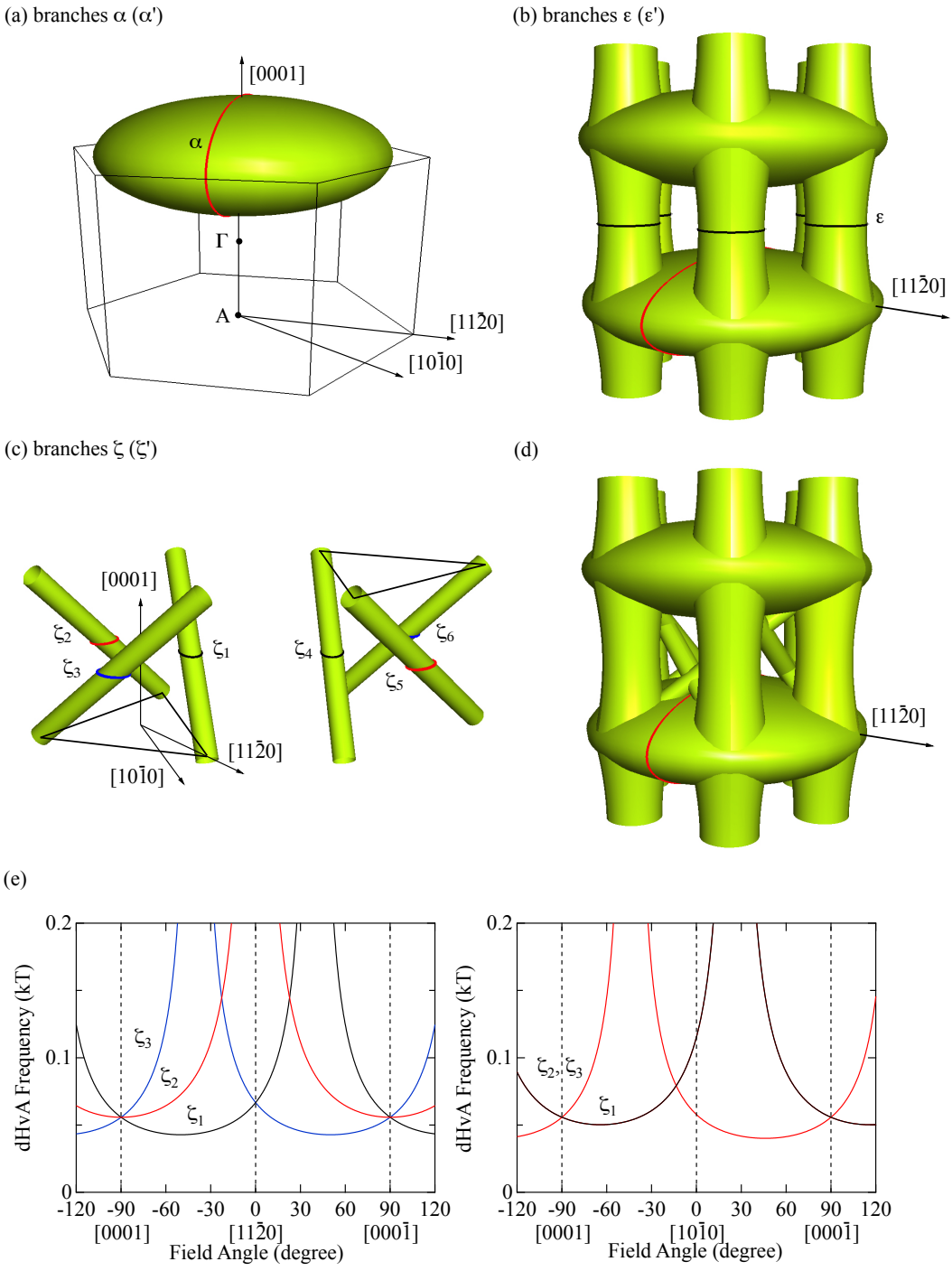

Figure 4.12: (a) A flat ellipsoidal Fermi surface named α, (b) a hyperboloidal Fermi surface named ε, (c) tilted cylindrical arms named ζ_1, ζ_2, and ζ_3 (ζ_4, ζ_5, and ζ_6), (d) multiply connected Fermi surfases, and (e) angular dependences of calculated dHvA frequencies of ζ_1, ζ_2, and ζ_3 (ζ_4, ζ_5, and ζ_6) in α-$IrSn_4$.

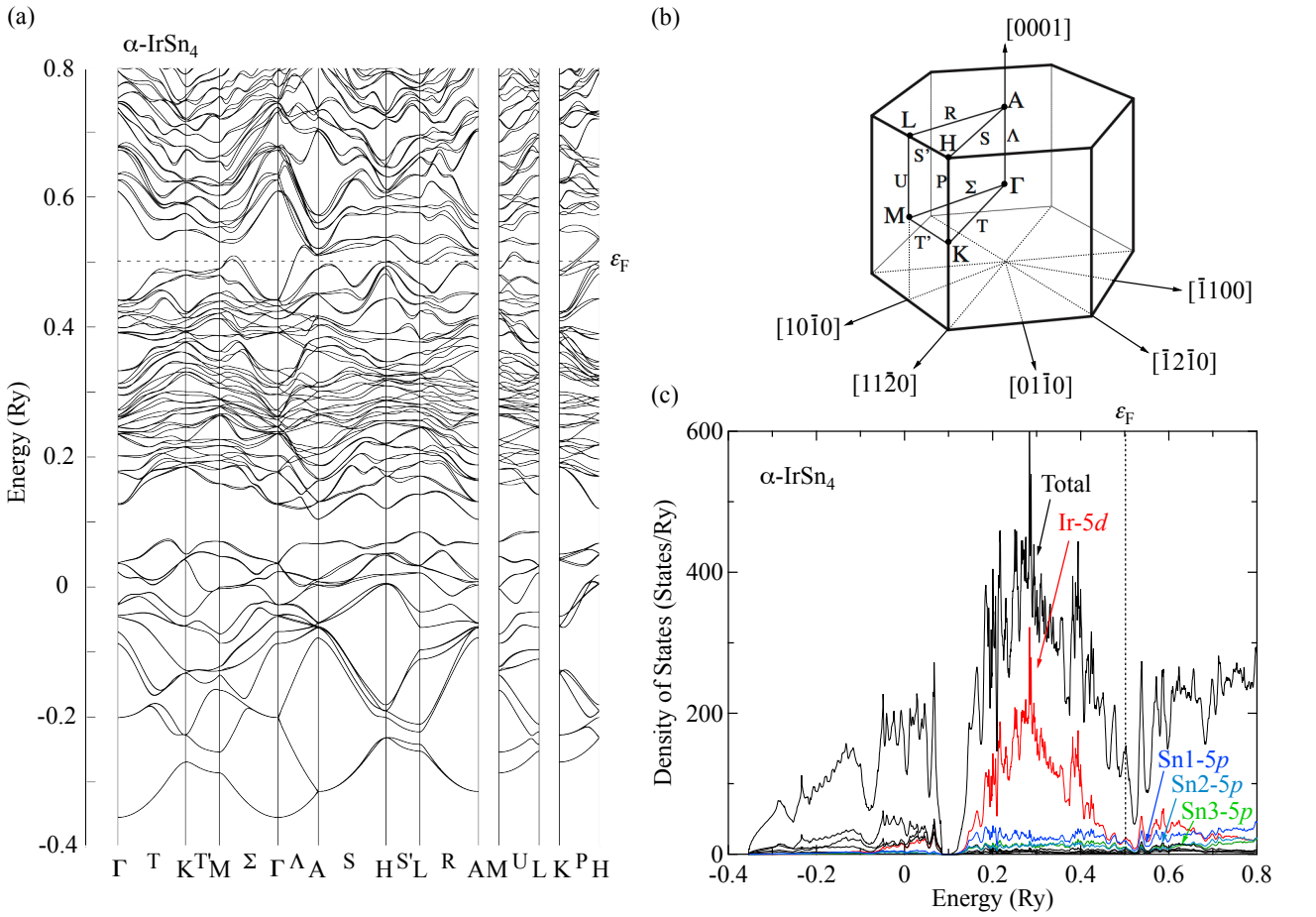

Figure 4.13: (a) Energy band structure in α-$IrSn_4$, (b) the corresponding Brillouin zone, and (c) the partial and total densities of states.

We conducted energy band calculations based on the density fluctional theory by local density approximation (LDA) and the full potential linear augmented plane wave (FLAPW) method, using lattice parameters and atomic positions in Table 3.2(a). In the present band calculations, the scalar relativistic effect was considered for all the valence electrons, and the spin-orbit interaction was included self-consistently for all the valence electrons as in a second variational procedure. Here, $5d^9$ in the Ir atom and $5s^25p^2$ in the Sn atom are treated as valence electrons in the band calculations. As a primitive cell contains three molecules of $IrSn_4$, the present compound is an uncompensated metal, which is reflected in the energy band structure, as shown in Fig. 4.13(a). A main Fermi surface with a hole character is expanded from the A point to a region close to the Γ and L points and to the H point, which corresponds to the flat ellipsoidal Fermi surface centered at the Γ point, as shown in Fig. 4.12(a). Namely, the experimentally estimated

ellipsoidal Fermi surface is a hole Fermi surface centered at the A point.

The partial and total densities of states are shown in Fig. 4.13(c), representing that Ir-5*d* electrons exist in the region from 0.1 to 0.5 Ry, with a peak at 0.3 Ry. A contribution of three kinds of Sn-5*p* electrons to the total density of states are dominant at the Fermi energy ε_F.

For reference, we measured the temperature dependence of the Hall coefficient, as shown in Fig. 4.14. The sign of the Hall coefficient is positive, corresponding to the hole Fermi surface with a large mobility. If we follow a simple one-carrier model, the carrier is 1.7×10^{22} holes/cm^3 at 2 K. Note that the one-carrier model is not applicable to the present compound with the multiply-connected Fermi surface, and in fact, the temperature dependence of the Hall coefficient is very complicated.

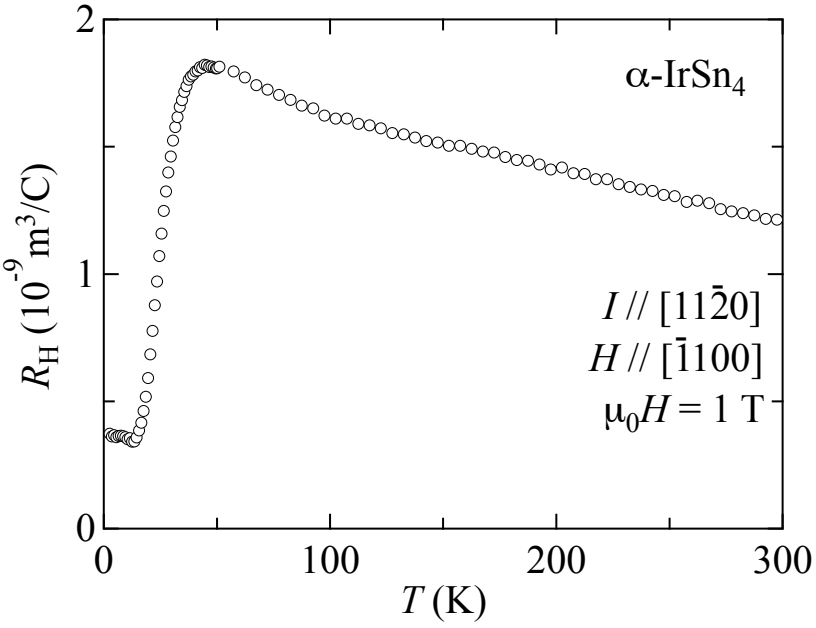

Figure 4.14: Temperature dependence of the Hall coefficient in α-$IrSn_4$.

The similar angular dependences of dHvA frequencies in α-$RhSn_4$ and $IrGe_4$ are shown in Figs. 4.15 and 4.16, respectively. Branches ζ and ζ' are observed in both compounds. The corresponding splitting energy is 350 K in α-$RhSn_4$ and 260 K in $IrGe_4$, which are almost the same value of 280 K in α-$IrSn_4$. Note that a spherical Fermi surface named φ is detected in α-$RhSn_4$ and $IrGe_4$, which is not observed in α-$IrSn_4$. The dHvA frequencies, cyclotron effective masses, and splitting energies in α-$RhSn_4$ and $IrGe_4$ are summarized in Tables 4.2(b) and 4.2(c), respectively.

Energy band calculations were also carried out for α-$RhSn_4$ and $IrGe_4$, as shown in Figs. 4.17(a) and 4.17(b), respectively. These energy bands are approximately the same as that of α-$IrSn_4$ in Fig. 4.13(a).

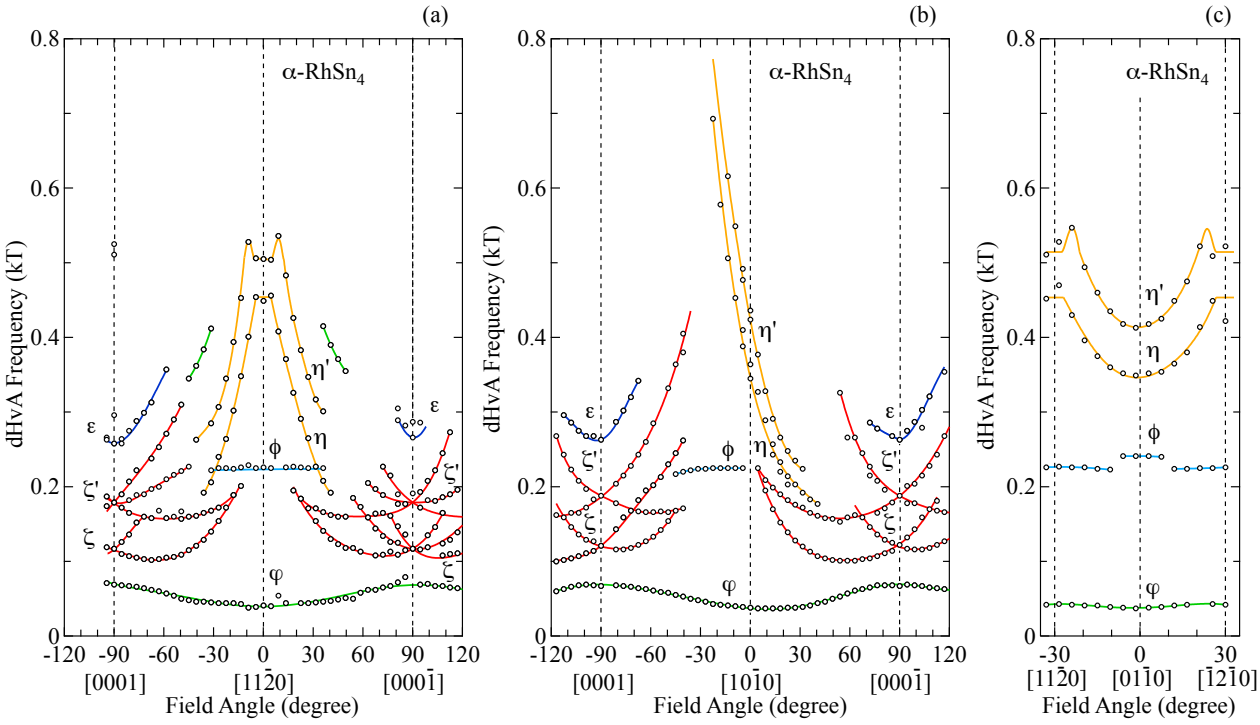

Figure 4.15: Angular dependences of dHvA frequencies of α-$RhSn_4$ in (a) from [0001] to [11$\bar{2}$0] and furthermore to [000$\bar{1}$], (b) from [0001] to [10$\bar{1}$0] and furthermore to [000$\bar{1}$], and (c) in the basal plane.

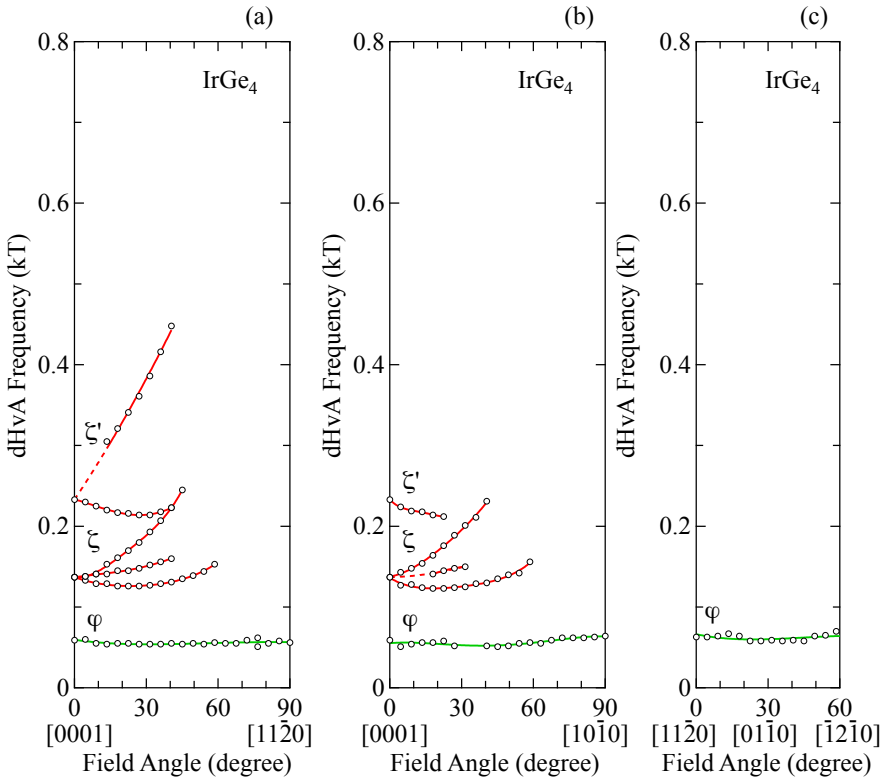

Figure 4.16: Angular dependences of dHvA frequencies of $IrGe_4$ in (a) from [0001] to [11$\bar{2}$0], (b) from [0001] to [10$\bar{1}$0], and (c) in the basal plane.

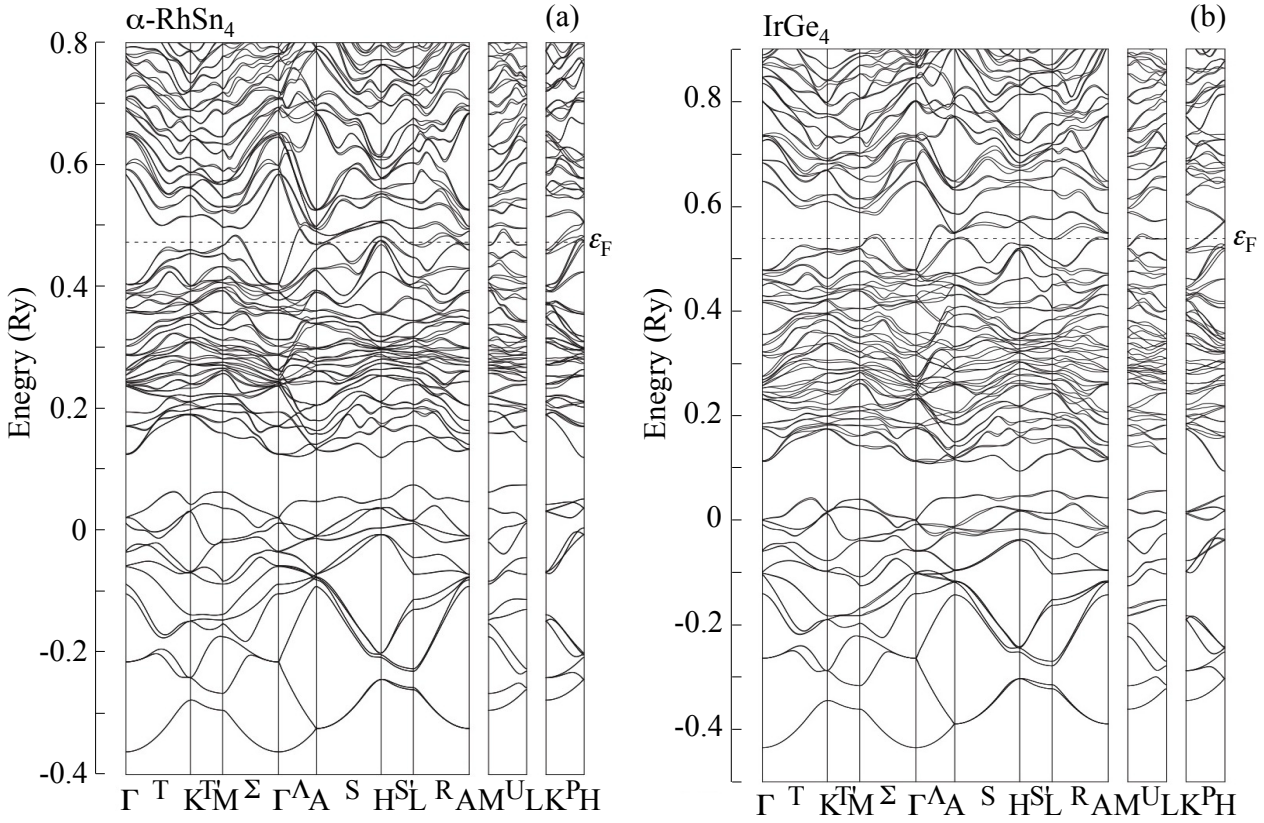

Figure 4.17: Energy band structures in (a) α-$RhSn_4$ and (b) $IrGe_4$.

CHAPTER 5

Conclusion

We successfully grew single crystals of α-$IrSn_4$ and α-$RhSn_4$ by the Sn-flux method and $IrGe_4$ by the Czochralski method in the tetra-arc furnace, together with polycrystals of $RhGe_4$ under pressure, and measured the electrical resistivity, specific heat, magnetoresistance, Hall coefficient, and de Haas-van Alphen effect. The experimental results are summarized as follows:

1. In addition to the usual Sn-flux method, we tried to grow single crystals of α-$IrSn_4$ in a horizontal two-zone electric furnace. The obtained single crystals were of especially high quality, with residual resistivity $\rho_0 = 0.052\ \mu\Omega \cdot \mathrm{cm}$ and residual resistivity ratio RRR = 1250.

2. Single crystals of α-$IrSn_4$, α-$RhSn_4$, and $IrGe_4$ were found to be an enantiopure of the trigonal chiral structure with space groups $P3_121$ (No. 152) or $P3_221$ (No. 154) on the basis of the Flack parameter determined by the single crystal X-ray diffraction analyses. We obtained many single crystalline samples in the Sn-flux method. One single crystal belongs to $P3_121$ and another belongs to $P3_221$ in α-$IrSn_4$ and α-$RhSn_4$. This is also applied to single crystalline ingots of $IrGe_4$, which were obtained using the Czochralsky method in a tetra-arc furnace.

3. We confirmed bulk superconductivity in $IrGe_4$ and $RhGe_4$ by measuring the specific heats. Both compounds are weak-coupling BCS-type superconductors. The upper critical field $\mu_0 H_{c2}$ at 0 K, $\mu_0 H_{c2}(0)$, in $IrGe_4$ is anisotropic, being 11.5 mT for $H \parallel [11\bar{2}0]$ and $[10\bar{1}0]$ and 22.5 mT for [0001]. The anisotropy of $\mu_0 H_{c2}$ was

explained by the effective mass model, resulting in the existence of a flat ellipsoidal Fermi surface in $IrGe_4$, with $k_a : k_c \simeq 9 : 4$ or $m_a^* : m_c^* \simeq 9^2 : 4^2$, where $2k_a$ and $2k_c$ are the caliper lengths of the ellipsoidal Fermi surface of revolution for $k_x(k_y)$ and k_z, respectively, and m_a^* and m_c^* are the corresponding masses. The present Fermi surface in $IrGe_4$ is applied to the other compounds.

4. The present compounds are uncompensated metals of which the transverse magnetoresistances indicate saturated behaviors in the high magnetic fields. Non-saturated behaviors were observed in the configuration of $J \parallel [11\bar{2}0]$ and $H \parallel [\bar{1}100]$, indicating the existence of open orbits along the [0001] direction.

5. From the results of the dHvA experiments for α-$IrSn_4$, we observed relatively large dHvA branches named α (α') for $H \parallel [11\bar{2}0]$ and β (β') for $H \parallel [10\bar{1}0]$. We believe that the dHvA branches $\alpha(\alpha')$ correspond to the belly orbits of the flat ellipsoidal Fermi surfaces of revolution estimated from the effective mass model for the upper critical field H_{c2} in $IrGe_4$. Thus, the obtained ellipsoidal Fermi surface occupies approximately 33 % of the Brillouin zone. From the results of energy band calculations, the present ellipsoidal Fermi surfaces are hole Fermi surfaces centered at the A point of the Brillouin zone. Branches α and α' are similar in the angular dependences of dHvA frequencies, representing the split Fermi surfaces due to the antisymmetric spin-orbit interaction based on the noncentrosymmetric (chiral) structure of this compound. We also observed other split dHvA branches. Among them, branches ε (ε') correspond to hyperbolic arm-like Fermi surfaces along the [0001] direction. Branches ζ (ζ') consist of two sets of three cylindrical arm-like Fermi surfaces. Each cylindrical arm is tilted by approximately 40 ° from the [0001] direction. These arm-like surfaces are most likely connected to the flat ellipsoidal Fermi surfaces, which favor the open orbits along the [0001] direction. A half Brillouin zone was roughly occupied by three Fermi surfaces named $\alpha(\alpha')$, $\varepsilon(\varepsilon')$, and $\zeta(\zeta')$, revealing no other main Fermi surfaces.

6. We observed the characteristic angular dependences of dHvA frequencies in α-$IrSn_4$. The dHvA frequencies in the configuration of $[0001] \rightarrow [11\bar{2}0] \rightarrow [000\bar{1}]$ are symmetric for $[11\bar{2}0]$, while those in the configuration of $[0001] \rightarrow [10\bar{1}0] \rightarrow [000\bar{1}]$ are asymmetric for $[10\bar{1}0]$, reflecting the present trigonal structure. In the basal plane, we also confirmed that those in the configuration of $[11\bar{2}0] \rightarrow [01\bar{1}0] \rightarrow [\bar{1}2\bar{1}0]$ are symmetric for $[01\bar{1}0]$.

7. Characteristic dHvA branches η (η') were also observed in α-$RhSn_4$ and $IrGe_4$. A small nearly spherical Fermi surface named φ was observed in α-$RhSn_4$ and $IrGe_4$, which was not detected in α-$IrSn_4$.

Bibliography

[1] E. Bauer and M. S. (ed.): *Non-Centrosymmetric Superconductors*, (Springer, Heidelberg, 2012) Lecture Notes in Physics, Vo. **847** .

[2] T. Kawai, H. Muranaka, T. Endo, N. Duc Dung, Y. Doi, S. Ikeda, T. D. Matsuda, Y. Haga, H. Harima, R. Settai, and Y. Ōnuki: J. Phys. Soc. Jpn. **77**, 064717 (2008).

[3] Y. Ōnuki and R. Settai: Low Temp. Phys. **38**, 89 (2012).

[4] S. Mühlbauer, B. Binz, F. Jonietz, C. Pfleiderer, A. Rosch, A. Neubauer, R. Georgii, and P. Böni: Science **323**, 915 (2009).

[5] Y. Tokura and N. Kanazawa: Chem. Rev. **121**, 2857 (2021).

[6] K. Kaneko, M. D. Frontzek, M. Matsuda, A. Nakao, K. Munakata, T. Ohhara, M. Kakihana, Y. Haga, M. Hedo, T. Nakama, and Y. Ōnuki: J. Phys. Soc. Jpn. **88**, 013702 (2019).

[7] I. Dzyaloshinsky: J. Phys. Chem. Solids **4**, 241 (1958).

[8] T. Moriya: Phys. Rev. **120**, 91 (1960).

[9] Y. Ōnuki, A. Nakamura, T. Uejo, A. Teruya, M. Hedo, T. Nakama, F. Honda, and H. Harima: J. Phys. Soc. Jpn. **83**, 1 (2014).

[10] K. Shiota, A. Inui, Y. Hosaka, R. Amano, Y. Ōnuki, M. Hedo, T. Nakama, D. Hirobe, J. Ohe, J. Kishine, H. M. Yamamoto, H. Shishido, and Y. Togawa: Phys. Rev. Lett. **127**, 126602 (2021).

[11] W. L. Bragg: Philos. Mag. **28**, 355 (1914).

[12] E. Bauer, G. Hilscher, H. Michor, C. Paul, E. W. Scheidt, A. Gribanov, Y. Seropegin, H. Noël, M. Sigrist, and P. Rogl: Phys. Rev. Lett. **92**, 027003 (2004).

[13] I. Patzak: Z. Metallkd. **47**, 418 (1956).

[14] E. Bauer, H. Kaldarar, A. Prokofiev, E. Royanian, A. Amato, J. Sereni, W. Brämer-Escamilla, and I. Bonalde: J. Phys. Soc. Jpn. **76**, 051009 (2007).

[15] G. L. J. A. Rikken and N. Avarvari: Phys. Rev. B **99**, 245153 (2019).

[16] H. Burzlaff and H. Zimmermann: *International Tables for Crystallography*, for Vol. A, 4th ed., ch. 9.2., edited by T. Hahn. Dordrecht/Boston/London: Kluwer Academic Publishers (1996) .

[17] H. Grimmer: Acta Crystallogr. A **71**, 143 (2015).

[18] T. Hahn and H. Klapper: *International Tables for Crystallography*, for Vol. A, 4th ed., ch. 10.3., edited by T. Hahn. Dordrecht/Boston/London: Kluwer Academic Publishers (1996) .

[19] Z. Ban and M. Sikirica: Acta Crystallogr. **18**, 594 (1965).

[20] W. Dörrscheidt and H. Schäfer: J. Less Common Met. **58**, 209 (1978).

[21] H. D. Flack: Acta Crystallogr. A **39**, 876 (1983).

[22] H. D. Flack and G. Bernardinelli: Chirality **20**, 681 (2008).

[23] D. D. Koelling and B. N. Harmon: J. Phys. C Solid State Phys. **10**, 3107 (1977).

[24] Y. Yanase and H. Harima: Solid State Physics **46**, pp. 237 (2011) [in Japanese] .

[25] H. Harima, T. Goho, and T. Tomi: J. Phys. Conf. Ser. **592** (2014).

[26] M. Kakihana, D. Aoki, A. Nakamura, F. Honda, M. Nakashima, Y. Amako, S. Nakamura, T. Sakakibara, M. Hedo, T. Nakama, and Y. Ōnuki: J. Phys. Soc. Jpn. **87**, 023701 (2018).

[27] D. Adroja, B. Padalia, S. Malik, R. Nagarajan, and R. Vijayaraghavan: J. Magn. Magn. Mater. **89**, 375 (1990).

[28] Y. Ōnuki, M. Hedo, and F. Honda: J. Phys. Soc. Jpn. **89**, 1 (2020).

[29] M. Kakihana, D. Aoki, A. Nakamura, F. Honda, M. Nakashima, Y. Amako, T. Takeuchi, H. Harima, M. Hedo, T. Nakama, and Y. Ōnuki: J. Phys. Soc. Jpn. **88**, 094705 (2019).

[30] Y. Ōnuki, M. Kakihana, W. Iha, K. Nakaima, D. Aoki, A. Nakamura, F. Honda, M. Nakashima, Y. Amako, J. Gouchi, Y. Uwatoko, S. Nakamura, T. Sakakibara, T. Takeuchi, Y. Haga, H. Ikeda, H. Harima, M. Hedo, and T. Nakama: J. Phys. Conf. Ser. **29**, 012001 (2020).

[31] M. Sakano, M. Hirayama, T. Takahashi, S. Akebi, M. Nakayama, K. Kuroda, K. Taguchi, T. Yoshikawa, K. Miyamoto, T. Okuda, K. Ono, H. Kumigashira, T. Ideue, Y. Iwasa, N. Mitsuishi, K. Ishizaka, S. Shin, T. Miyake, S. Murakami, T. Sasagawa, and T. Kondo: Phys. Rev. Lett. **124**, 136404 (2020).

[32] G. Gatti, D. Gosálbez-Martínez, S. S. Tsirkin, M. Fanciulli, M. Puppin, S. Polishchuk, S. Moser, L. Testa, E. Martino, S. Roth, P. Bugnon, L. Moreschini, A. Bostwick, C. Jozwiak, E. Rotenberg, G. Di Santo, L. Petaccia, I. Vobornik, J. Fujii, J. Wong, D. Jariwala, H. A. Atwater, H. M. Rønnow, M. Chergui, O. V. Yazyev, M. Grioni, and A. Crepaldi: Phys. Rev. Lett. **125**, 216402 (2020).

[33] J. Bardeen, L. N. Cooper, and J. R. Schrieffer: Phys. Rev. **108**, 1175 (1957).

[34] K. Ueda and Y. Ōnuki: *Physics of Heavy Electron Systems* (Shokabo, Tokyo, 1998) p.291-292 [in Japanese] .

[35] V. L. Ginzburg: Zh. Eksp. Teor. Fiz. **20**, 1064 (1950).

[36] E. Helfand and N. R. Werthamer: Phys. Rev. **147**, 288 (1966).

[37] N. R. Werthamer, E. Helfand, and P. C. Hohenberg: Phys. Rev. **147**, 295 (1966).

[38] R. Settai, Y. Miyauchi, T. Takeuchi, F. Lévy, I. Sheikin, and Y. Ōnuki: J. Phys. Soc. Jpn. **77**, 073705 (2008).

[39] N. Tateiwa, Y. Haga, T. D. Matsuda, S. Ikeda, E. Yamamoto, Y. Okuda, Y. Miyauchi, R. Settai, and Y. Ōnuki: J. Phys. Soc. Jpn. **76**, 083706 (2007).

[40] B. Joshi, A. Thamizhavel, and S. Ramakrishnan: Phys. Rev. B **84**, 064518 (2011).

[41] E. M. Carnicom, W. Xie, T. Klimczuk, J. Lin, K. Górnicka, Z. Sobczak, N. P. Ong, and R. J. Cava: Sci. Adv. **4**, eaar7969 (2018).

[42] U. Gottlieb, J. C. Lasjaunias, J. L. Tholence, O. Laborde, O. Thomas, and R. Madar: Phys. Rev. B **45**, 4803 (1992).

[43] B. Joshi, A. Thamizhavel, and S. Ramakrishnan: J. Phys. Conf. Ser. **592**, 012069 (2015).

[44] A. Amon, E. Svanidze, R. Cardoso-Gil, M. N. Wilson, H. Rosner, M. Bobnar, W. Schnelle, J. W. Lynn, R. Gumeniuk, C. Hennig, G. M. Luke, H. Borrmann, A. Leithe-Jasper, and Y. Grin: Phys. Rev. B **97**, 014501 (2018).

[45] B. Chevalier, P. Lejay, A. Cole, M. Vlasse, and J. Etourneau: Solid State Commun. **41**, 801 (1982).

[46] A. B. Karki, Y. M. Xiong, I. Vekhter, D. Browne, P. W. Adams, D. P. Young, K. R. Thomas, J. Y. Chan, H. Kim, and R. Prozorov: Phys. Rev. B **82**, 064512 (2010).

[47] E. Bauer, G. Rogl, X.-Q. Chen, R. T. Khan, H. Michor, G. Hilscher, E. Royanian, K. Kumagai, D. Z. Li, Y. Y. Li, R. Podloucky, and P. Rogl: Phys. Rev. B **82**, 064511 (2010).

[48] E. Bauer, C. Sekine, U. Sai, P. Rogl, P. K. Biswas, and A. Amato: Phys. Rev. B **90**, 054522 (2014).

[49] H. Niimura, K. Kawashima, K. Inoue, M. Yoshikawa, and J. Akimitsu: J. Phys. Soc. Jpn. **83**, 044702 (2014).

[50] U. Eibenstein and W. Jung: J. Solid State Chem. **133**, 21 (1997).

[51] K. Togano, P. Badica, Y. Nakamori, S. Orimo, H. Takeya, and K. Hirata: Phys. Rev. Lett. **93**, 247004 (2004).

[52] P. Badica, T. Kondo, and K. Togano: J. Phys. Soc. Jpn. **74**, 1014 (2005).

[53] H. Q. Yuan, D. F. Agterberg, N. Hayashi, P. Badica, D. Vandervelde, K. Togano, M. Sigrist, and M. B. Salamon: Phys. Rev. Lett. **97**, 017006 (2006).

[54] T. P. Ying, Y. P. Qi, and H. Hosono: Phys. Rev. B **100**, 094522 (2019).

[55] R. Gupta, T. P. Ying, Y. P. Qi, H. Hosono, and R. Khasanov: Phys. Rev. B **103**, 174511 (2021).

[56] T. Shang, W. Wei, C. Baines, J. L. Zhang, H. F. Du, M. Medarde, M. Shi, J. Mesot, and T. Shiroka: Phys. Rev. B **98**, 180504 (2018).

[57] K. Kawashima, T. Muranaka, and J. Akimitsu: Sci. Technol. Adv. Mater. **7**, 9 (2006).

[58] K. Kawashima, A. Kawano, T. Muranaka, and J. Akimitsu: J. Phys. Soc. Jpn. **74**, 700 (2005).

[59] J. M. Hopkinson and H.-Y. Kee: Phys. Rev. B **74**, 224441 (2006).

[60] S. V. Isakov, J. M. Hopkinson, and H.-Y. Kee: Phys. Rev. B **78**, 014404 (2008).

[61] T. E. Redpath and J. M. Hopkinson: Phys. Rev. B **82**, 014410 (2010).

[62] P. Bak and J. von Boehm: Phys. Rev. B **21**, 5297 (1980).

[63] Y. Ishikawa, K. Tajima, D. Bloch, and M. Roth: Solid State Commun. **19**, 525 (1976).

[64] A. Bauer and C. Pfleiderer: Phys. Rev. B **85**, 214418 (2012).

[65] A. Neubauer, C. Pfleiderer, B. Binz, A. Rosch, R. Ritz, P. G. Niklowitz, and P. Böni: Phys. Rev. Lett. **102**, 186602 (2009).

[66] C. Tabata, T. Matsumura, H. Nakao, S. Michimura, M. Kakihana, T. Inami, K. Kaneko, M. Hedo, T. Nakama, and Y. Ōnuki: J. Phys. Soc. Jpn. **88**, 093704 (2019).

[67] G. Shirane, R. Cowley, C. Majkrzak, J. B. Sokoloff, B. Pagonis, C. H. Perry, and Y. Ishikawa: Phys. Rev. B **28**, 6251 (1983).

[68] Y. Togawa, Y. Kousaka, K. Inoue, and J. Kishine: J. Phys. Soc. Jpn. **85**, 112001 (2016).

[69] T. Miyadai, K. Kikuchi, H. Kondo, S. Sakka, M. Arai, and Y. Ishikawa: J. Phys. Soc. Jpn. **52**, 1394 (1983).

[70] J. Kishine: Solid States Physics **53**, 1-19, No. 1 (2018) [in Japanese] .

[71] Y. Togawa, T. Koyama, K. Takayanagi, S. Mori, Y. Kousaka, J. Akimitsu, S. Nishihara, K. Inoue, A. S. Ovchinnikov, and J. Kishine: Phys. Rev. Lett. **108**, 107202 (2012).

[72] M. Groenewege: Mol. Phys. **5**, 541 (1962).

[73] L. Zhang and Q. Niu: Phys. Rev. Lett. **115**, 115502 (2015).

[74] J. Kishine, A. S. Ovchinnikov, and A. A. Tereshchenko: Phys. Rev. Lett. **125**, 245302 (2020).

[75] S. Sengupta, M. N. Y. Lhachemi, and I. Garate: Phys. Rev. Lett. **125**, 146402 (2020).

[76] T. Nomura, X.-X. Zhang, S. Zherlitsyn, J. Wosnitza, Y. Tokura, N. Nagaosa, and S. Seki: Phys. Rev. Lett. **122**, 145901 (2019).

[77] K. Ishito, H. Mao, Y. Kousaka, Y. Togawa, S. Iwasaki, T. Zhang, S. Murakami, J.-i. Kishine, and T. Satoh: Nat. Phys. **19**, 35 (2023).

[78] G. L. J. A. Rikken and E. Raupach: Nature **405**, 932 (2000).

[79] Y. Xu, G. Yang, H. Xia, G. Zou, Q. Zhang, and J. Gao: Nat. Commun. **5**, 5050 (2014).

[80] I. Mogi and K. Watanabe: Sci. Technol. Adv. Mater. **7**, 342 (2006).

[81] V. Krstić and G. Rikken: Chem. Phys. Lett. **364**, 51 (2002).

[82] G. L. Rikken and N. Avarvari: Phys. Rev. B **99**, 1 (2019).

[83] T. Yokouchi, N. Kanazawa, A. Kikkawa, D. Morikawa, K. Shibata, T. Arima, Y. Taguchi, F. Kagawa, and Y. Tokura: Nat. Commun. **8**, 866 (2017).

[84] R. Aoki, Y. Kousaka, and Y. Togawa: Phys. Rev. Lett. **122**, 57206 (2019).

[85] A. Lang and W. Jeitschko: J. Mater. Chem. **6**, 1897 (1996).

[86] R. Omura, E. Suto, N. Nakamura, R. Higashinaka, T. D. Matsuda, and Y. Aoki: JPS Conf. Proc. **30**, 011018 (2020).

[87] E. L. Nordmark, O. Wallner, and U. Häussermann: J. Solid State Chem. **168**, 34 (2002).

[88] V. I. Larchev and S. V. Popova: J. Less-Common Met. **98**, L1 (1984).

[89] X. Z. Xing, C. Q. Xu, N. Zhou, B. Li, J. Zhang, Z. X. Shi, and X. Xu: Appl. Phys. Lett. **109**, 122403 (2016).

[90] P. Panday and K. Schubert: J. Less-Common Met. **18**, 175 (1969).

[91] Y. Xu, M. Yamazaki, and P. Villars: Jpn. J. Appl. Phys. **50** (2011).

[92] Z. Kletowski, N. Iliev, Z. Henkie, and B. Staliński: J. Less-Common Met. **110**, 235 (1985).

[93] J. Q. Yan, B. C. Sales, M. A. Susner, and M. A. McGuire: Phys. Rev. Mater. **1**, 1 (2017).

[94] T. Irifune, A. Kurio, S. Sakamoto, T. Inoue, and H. Sumiya: Nature **421**, 599 (2003).

[95] Z.-A. Ren, G.-C. Che, X.-L. Dong, J. Yang, W. Lu, W. Yi, X.-L. Shen, Z.-C. Li, L.-L. Sun, F. Zhou, and Z.-X. Zhao: EPL **83**, 17002 (2008).

[96] X. Wang, Q. Liu, Y. Lv, W. Gao, L. Yang, R. Yu, F. Li, and C. Jin: Solid State Commun. **148**, 538 (2008).

[97] H. Kito, H. Eisaki, and A. Iyo: J. Phys. Soc. Jpn. **77**, 20 (2008).

[98] K. Tanaka, Y. Kawahito, Y. Yonezawa, D. Kikuchi, H. Aoki, K. Kuwahara, M. Ichihara, H. Sugawara, Y. Aoki, and H. Sato: J. Phys. Soc. Jpn. **76**, 103704 (2007).

[99] H. Kunitoshi, T. D. Matsuda, R. Midorikawa, R. Higashinaka, K. Kuwahara, Y. Aoki, and H. Sato: J. Phys. Soc. Jpn. **85**, 114708 (2016).

[100] G. M. Sheldrick: SHELXL97, Program for the Refinement of Crystal Structures (University of Gottingen, Germany, 1997).

[101] I. M. Lifshitz and A. M. Kosevich: Dokl. Akad. Nauk SSR **96**, 963 (1954).

[102] I. M. Lifshitz and A. M. Kosevich: Zh. Eksp. Teor. Fiz. **29**, 730 (1955).

[103] H. Takahashi, K. Ishimura, T. Okamoto, E. Ohmichi, and H. Ohta: J. Phys. Soc. Jpn. **86**, 8 (2017).

[104] C. Rossel, P. Bauer, D. Zech, J. Hofer, M. Willemin, and H. Keller: J. Appl. Phys. **79**, 8166 (1996).

[105] M. J. Naughton, J. P. Ulmet, A. Narjis, S. Askenazy, M. V. Chaparala, and A. P. Hope: Rev. Sci. Instrum. **68**, 4061 (1997).

[106] E. Ohmichi and T. Osada: Rev. Sci. Instrum. **73**, 3022 (2002).

[107] H. Padamsee, J. E. Neighbor, and C. A. Shiffman: J. Low Temp. Phys. **12**, 387 (1973).

[108] D. C. Johnston: Supercond. Sci. Technol. **26**, 115011 (2013).

[109] R. A. Klemm and J. R. Clem: Phys. Rev. B **21**, 1868 (1980).

Publication List

(Last update 2023/2/8)

1. Fermi Surface and Superconducting Properties of α-$IrSn_4$, α-$RhSn_4$, $IrGe_4$, and $RhGe_4$ with Trigonal Chiral Structure,
Naoki Nakamura, Ayano Yanuma, Yuma Chiba, Rumi Omura, Ryuji Higashinaka, Hisatomo Harima, Yuji Aoki, and Tatsuma D. Matsuda,
J. Phys. Soc. Jpn. **92**, 034701 (2023).

2. Superconducting Properties of Cage Compounds $YbTr_2Al_{20}$ with Tr = Mo and Ta,
Naoki Nakamura, Ryuji Higashinaka, Yuji Aoki, and Tatsuma D. Matsuda,
Solid State Commun. **6**, 115098 (2023).

3. μSR and Neutron Scattering Studied on Possible Partially-Disordered Magnetic State Coexisting with Heavy Quasiparticles in $SmPt_2Si_2$,
Naoki Nakamura, Ryuji Higashinaka, Kengo Fushiya, Ryo Tsubota, Takashi U. Ito, Wataru Higemoto, Nakao Akiko, Ryoji Kiyanagi, Takashi Ohhara, Koji Kaneko, Tatsuma D. Matsuda, and Yuji Aoki,
JPS Conf. Proc. **30**, 011062 (2020).

4. Crystal Structure and Magnetic Properties for Single Crystals of $YbTr_2Al_{20}$ (Tr = Mo and Ta),
Naoki Nakamura, Ryuji Higashinaka, Yuji Aoki, and Tatsuma D. Matsuda,
JPS Conf. Proc. **29**, 012009 (2020).

5. Single Crystal Growth and Anomalous Magnetoresistance of Chiral Crystal α-$IrSn_4$,
Rumi Omura, Eri Suto, **Naoki Nakamura**, Ryuji Higashinaka, Tatsuma D. Matsuda, and Yuji Aoki,
JPS Conf. Proc. **30**, 011018 (2020).

6. Structural and Magnetic Properties of New Cubic Compounds $PrRu_2In_2Zn_{18}$,
Takahiro Komagata, Kazuhei Wakiya, Yuki Sugiyama, Masatomo Uehara, Izuru Umehara, **Naoki Nakamura**, Tatsuma D. Matsuda, Yuji Aoki, Jun Gouchi, and Yoshiya Uwatoko,
JPS Conf. Proc. **30**, 011157 (2020).

7. Large diamagnetism and low-lying optical phonon modes in Pt–Cd γ-phase,
Nazir Ahmad, Takumi Hasegawa, **Naoki Nakamura**, Ryuji Higashinaka, Tatsuma D. Matsuda, and Yuji Aoki,
J. Alloys Compd. **901**, 163520 (2022).

Acknowledgements

I am indebted to Prof. Tatsuma D. Matsuda, my supervisor for a period of six years, for encouraging me to carry out single crystal growth and crystal structure analyses of single crystalline samples and to construct a cantilever-type de Hass-van Alphen (dHvA) equipment, which completed the present Thesis. Assis. Prof. Ryuji Higashinaka was kind enough to help me with various measurements in the first stage of my research and continuous suggestions. I would also like to express my gratitude to Prof. Yuji Aoki and Prof. Hideyuki Sato for teaching me superconductivity and magnetoresistance in glowing terms. Invaluable help came from Prof. Yoshichika Ōnuki. His advice for the dHvA effect and the Fermi surface is highly appreciated.

I would like to extend my special thanks to Prof. Hisatomo Harima of Kobe University for a helpful result of band calculations and to Prof. Dai Aoki and Assis. Prof. Ai Nakamura of Tohoku University for their technical help and support of a pick-up-coil-type dHvA experiment.

I would also like to express my gratitude to all the members of *denshi* laboratory of Tokyo Metropolitan University, especially to Mr. Ahmad Nazir for fruitful discussions, Mr. Afzal Md Asif for theoretical calculations, and Dr. Akira Yamada for his encouragement of my research.

Finally, my appreciation goes to my family for their continuous support and encouragement.

Naoki Nakamura
February 2023